



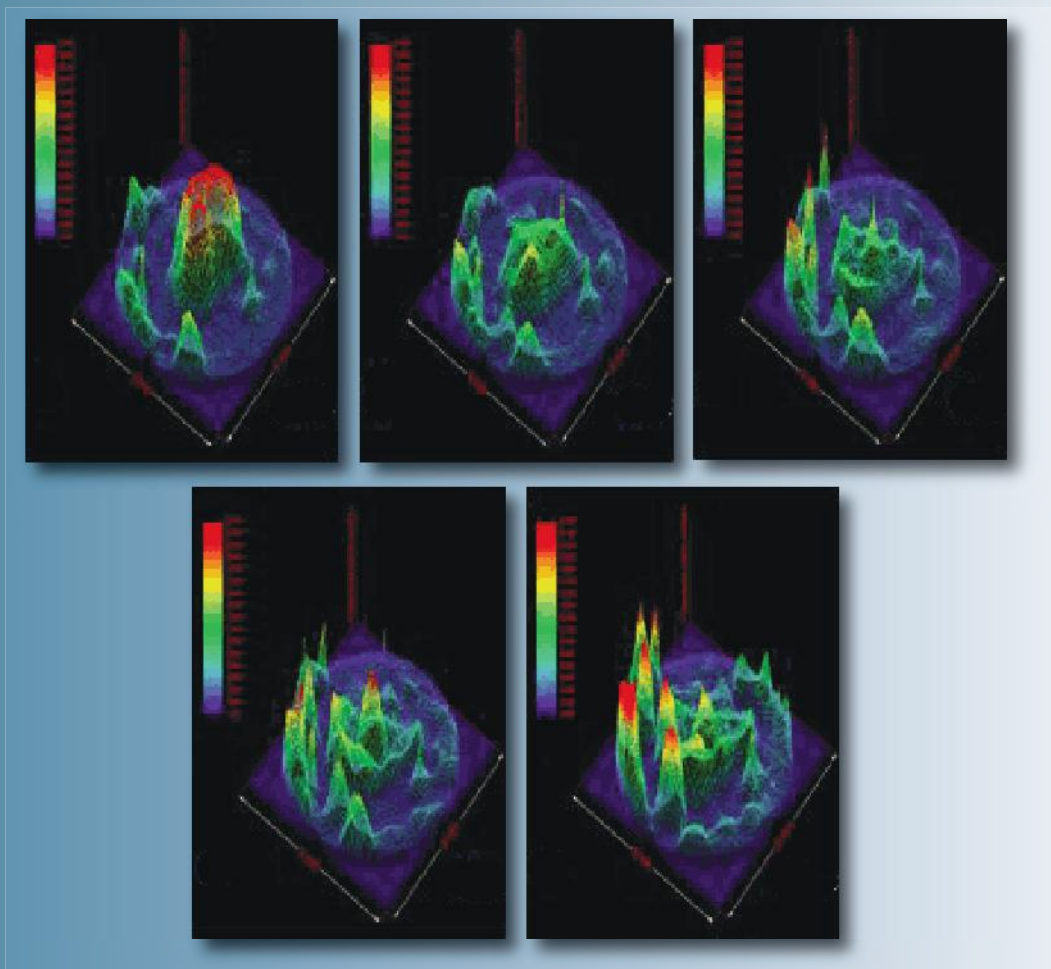
ISSN 1028-8546

Volume XIX, Number 1
Section: En
April, 2013

Azerbaijan Journal of Physics

Fizika

www.physics.gov.az



G.M. Abdullayev Institute of Physics
Azerbaijan National Academy of Sciences
Department of Physical, Mathematical and Technical Sciences

Azerbaijan Journal of Physics

FİZİKÁ

*G.M.Abdullayev Institute of Physics
Azerbaijan National Academy of Sciences
Department of Physical, Mathematical and Technical Sciences*

HONORARY EDITORS

Arif PASHAYEV

EDITORS-IN-CHIEF

Nazim MAMEDOV

Chingiz QAJAR

SENIOR EDITOR

Talat MEHDIYEV

INTERNATIONAL REVIEW BOARD

Ivan Scherbakov, Russia
Kerim Allahverdiyev, Turkey
Mehmet Öndr Yetiş, Turkey
Gennadii Jablonskii, Buelorussia
Rafael Imamov, Russia
Vladimir Man'ko, Russia
Eldar Salayev, Azerbaijan
Dieter Hochheimer, USA
Victor L'vov, Israel
Vyacheslav Tuzlukov, South Korea
Majid Ebrahim-Zadeh, Spain

Firudin Hashimzadeh, Azerbaijan
Anatoly Boreysho, Russia
Mikhail Khalin, Russia
Hasan Bidadi, Tebriz, East Azerbaijan, Iran
Natiq Atakishiyev, Mexico
Maksud Aliyev, Azerbaijan
Bahram Askerov, Azerbaijan
Arif Hashimov, Azerbaijan
Vali Huseynov, Azerbaijan
Javad Abdinov, Azerbaijan
Bagadur Tagiyev, Azerbaijan

Tayar Djafarov, Azerbaijan
Talat Mehdiyev, Azerbaijan
Emil Guseynov, Azerbaijan
Ayaz Baramov, Azerbaijan
Tofiq Mammadov, Azerbaijan
Salima Mehdiyeva, Azerbaijan
Shakir Nagiyev, Azerbaijan
Rauf Guseynov, Azerbaijan
Almuk Abbasov, Azerbaijan
Iskender Djafarov, Azerbaijan
Yusif Asadov, Azerbaijan

TECHNICAL EDITORIAL BOARD

Senior secretary Elmira Akhundova, Nazli Guseynova, Sakina Aliyeva,
Nigar Akhundova, Elshana Aleskerova

PUBLISHING OFFICE

33 H.Javid ave, AZ-1143, Baku
ANAS, G.M.Abdullayev Institute of Physics

Tel.: (99412) 439-51-63, 439-32-23
Fax: (99412) 447-04-56
E-mail: jophphysics@gmail.com
Internet: www.physics.gov.az

It is authorized for printing:

Published at "SƏRQ-QƏRB"
17 Ashug Alessger str., Baku
Typographer : Aziz Gulaliyev

Sent for printing on: ___.__. 201__
Printing approved on: ___.__. 201__
Physical binding: _____
Number of copies: _____200
Order: _____

ATOMIC-FORCE MICROSCOPY OF VAN-DER WAALS SURFACE OF LAYERED CRYSTALS BY GaSe AND GaSe<IMPURITY> TYPES

A.M. PASHAYEV, B.G. TAGIYEV, R.A. IBRAGIMOV, A.A. SAFARZADE

National Academy of Aviation of Azerbaijan

e-mail:safarzade@yandex.ru

The morphological peculiarities of chipped Van-der-Waals surface of layered crystals by GaSe and GaSe<impurity> types are investigated by method of scanning atomic-force microscopy. The obtained morphology images show that plastic reconstruction in the complex goffer form with pyramidal nano-formations takes place as a result of mechanical chip. The atomic-force investigation methods allows us to suppose that obtained morphologies of layered crystal surface are the consequence of the complex of surface energy interacting processes at the chip, dislocation implantation into interlayer space and chemisorptions process in *ex situ* conditions.

Keywords: Van-der-Waals surface, layered crystals, morphology

PACS: 68.35.Bs, 68.35.Dv, 68.37

1. INTRODUCTION

The layered semiconductor GaSe is the binary arsenide and belongs to $A^{III}B^{VI}$ group. The layered crystals (LC) are composite of X-M-M-X quadro-layers (see fig.1) inside of which the strong covalent bond and weak ion (Van-der-Waals VdW) bond between layers take place (fig.1).

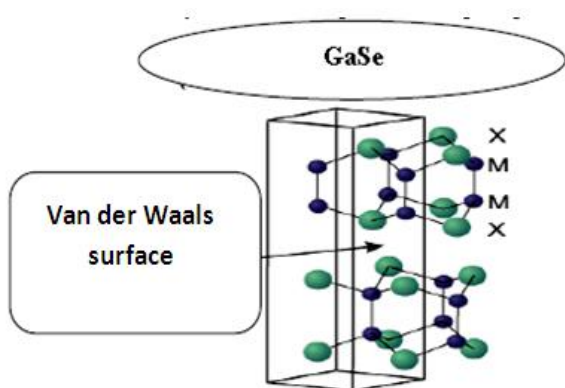


Fig.1. The layer structure and position of VdW (Van-der-Waals) surface of layered semiconductor crystals of GaSe type. X are (chalcogens) elements of VI group of Mendeleyev table, M are (metals) elements of III group of Mendeleyev table.

The difference of interatomic bond types inside and between layers are the reason of LC physical property anisotropy. The chemical bond anisotropy inside and between layers GaSe allows us to obtain the atomically clean surface with low density of surface states ($\leq 10^{10} \text{ cm}^{-2}$) by chip way [1].

The modern optoelectronics requires the formation of new generation devices: transformers of light and electric energies which are sensitive to radiation polarization [2]. For the achievement of this aim especially transformers of the light energy into electric one and electric energy into polarized light energy are useful on the base of strongly anisotropic semiconductor

compounds $A^{III}B^{VI}$. The big value of luminescence inner quantum yield and high photosensitivity in optical band in combination with optic transition anisotropy in Brillouin band critic points of mentioned materials allows us to form the optoelectronic devices on their base with new functional possibilities in the form of polarimetric detectors which are sources and receivers of linear-polarized radiation [3].

Se atoms forming the VdW-surface of GaSe crystal have the non-metallic character and it is the main reason of LC difficult oxidation [4]. The high stability to oxidation, low surface roughness and absence of the broken bands gives us the possibility of morphology investigation of LC cleaved surface by atomic-force microscopy on air at room temperature in *ex situ* conditions. The presence of thin oxide film on LC VdW-surface which appears in several minutes after sample exposition on air [5] should be taken into consideration at representation of real structure of investigated surface [6].

The probe microscopy is the one of the advanced methods of surface investigation in nano-meter scale. The method name is obtained by force type used in it. At AFM investigations of oxide surfaces in noncontact mode the interaction force between probe point and surface is defined by electrostatic charges on oxide surface, and also by VdW-forces [6]. AFM-investigations are carried out after carrying out of sample preparation (*ex situ*) on air.

The aim of the present work is the study of GaSe VdW-surface morphology obtained by chip method with AFM method use at room temperature in *ex situ* conditions.

2. EXPERIMENT TECHNIQUE

The single crystalline layer semiconductor GaSe is grown up by Bridgman-Stockbarger vertical method that provides the electronic conduction by 0,1 order $\Omega^{-1} \cdot \text{cm}^{-1}$ and electron concentration $\sim 10^{13} \text{ cm}^{-3}$ at temperature 300°K. The atom geometric position corresponds to hexagonal structure with lattice parameters given in table 1.

Table 1

Polytype	β	ε	γ	δ
Lattice parameter, Å: a	3,755	3,755	3,735	3,755
Lattice parameter, Å: c	15,95	15.996	23.862	31,99

AFM-investigations are carried out with the use of atomic-force microscope Solver-NEXT.

For AFM-investigations the sample VdW-surface is formed by the means of elimination of several single crystal upper layers by adhesive ribbon (sticky tape) on air. After chip the scan surface presents itself the atomic plane (0001). The duration of following arrangement of investigated VdW-surface on scanning table of AFM microscope and measurement carrying out don't exceed 2-3min. The scanning square is chosen $\sim 5 \times 5 \mu\text{m}$, scanning

velocity is not more $3 \mu\text{m}/\text{sec}$, feedback amplification is 3,0, operating point is 0,8.

3. EXPERIMENTAL RESULTS AND THEIR DISCUSSION

The separate nano-formations which have the pyramidal form are clearly observed on AFM-sample (fig.2). One can take into consideration the interaction between probe and LC surface, and also the atmosphere influence on surrounding sample on AFM-images.

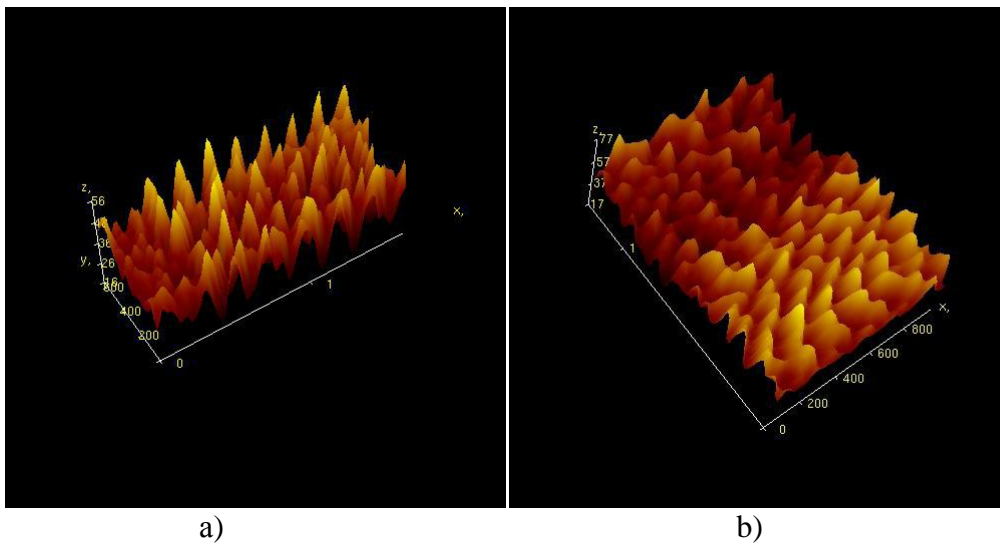


Fig.2 . a) AFM-image of VdW surface of GaSe<0,1%Zn> LC surface and b) AFM-image of VdW surface of GaSe<0,1%Sn> LC surface in 3D scale.

The analysis of published results of AFM investigations shows on dependence of atomic permission degree on sample obtaining method and surface preparation, storage duration, investigated medium and temperature value.

The form, lateral dimension and nano-dimension cavity distribution in GaSe<0,1%Sn> crystal upper layer depend on intercalant type (electronegativeness, atomic dimension), value and distribution of surface stresses, an also on technological conditions of GaSe growing with the impurity [7].

The continuous film of natural oxide as it is observed on AFM-images of oxidated GaSe surface, forms on GaSe VdW-surface at long duration on air. The natural oxide formation takes place in the result of oxidation process carrying out in LC defect regions, nano crystal generation and their coaliscence and recrystallization, and also deformation processes on the boundary between oxide film and LC [5].

The natural oxide which forms at room temperature in the presence of atmospheric water can be result of chemisorption of water molecule and oxygen on separate

surface structural defects which are unordered arranged on LC VdW-surface [8]. The increase of this layer probably takes place at chemical reaction carrying out which are placed between selenium oxide and water with formation of selenious acid [5].



The carrying out of chemical reactions with participation of acid and metal atoms leads to formation of oxide nano-formations. The oxide films on LC surface adsorb the atmospheric water and this causes to their increase because of reaction carrying out on LC-oxide interface. At LC storage on air during several years, the thickness of oxide layers can achieve the value of several μm . The SeO_2 , SeO_3 and Se_2O_5 oxides which are observed on GaSe VdW-surface also can present in natural oxide [5].

The oxidation of LC VdW-surface takes place in defect regions of these crystals [9]. The main defect generation in this plane is connected with small formation

energy of Se vacancies. These vacancies interact between each other and form the clusters of charged vacancies (nano-formations) [101]. The chalcogen vacancies shift with high velocity and coalesce in LC basic plane (0001). The chalcogen vacancy and their nano-dimension clusters are adsorbed centers at oxidation of nano-porous LC [11]. The bulging oxide nano-formations by height up to ~ 15÷20 nm are observed on AFM-images scanned on air of GaSe and GaSe <impurity> crystal surfaces. The morphology of these nano-formations in lateral plane (rings, circles) reflect the interaction character between charged vacancies on the surface with molecular bond type. The covalent bonds between metal atoms destroy and they naturally fall into interface space at formation of surface defects which have the circle form (close to hexahedron) in LC basic plane with radius more than ~ 10nm [5].

The non-equilibrium system of defects and adsorbed particles on VdW-surface strives for the equilibrium by the way of self-organization forming the surface with minimal energy [12,13]. At such processes the goffered structure which is observed on VdW-surface forms. One can suppose that corrugated surface forms by the way of self-organization in the result of carrying out of

cooperative dislocation processes in basic and pyramidal crystallographic planes, in upper LC layers [12]. The corrugating of VdW-surface is observed in Ni-Ga-Se system [14], for clusters of Cu atoms the corrugating is observed in upper layers VSe₂ [15]. The simple corrugated surface with periodic alternation of maximums which are characterized by small values of amplitude and big values of period is observed.

Defects on GaSe surface are dark nanocavity which have forms of circle and hexahedron, their lateral dimensions and the depth achieve ~ 10 nm и ~ 20 nm correspondingly (fig.4).

They are formed by native defects and are responsible for presence of oxide nano-formations in LC depth. The surface defects of such type (“clusters of point defects” of hexahedral form in LC basic plane) had been observed earlier by AFM method [7,12].

The separate nano-formations which have the pyramidal form are observed on AFM-image of GaSe VdW-surface obtained in noncontact mode [16]. The nano-formation dimensions by height achieve ~20÷30 nm (fig.4). It is mentioned that oxidation of LC VdW-surface takes place in defect regions of these crystals [17].

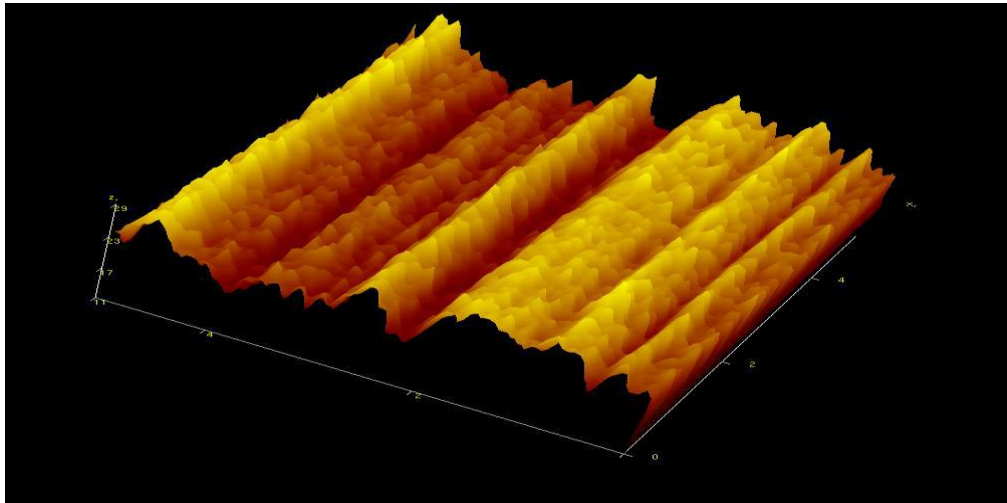


Fig.3. The corrugated structure of AFM-images of layered GaSe VdW-surface.

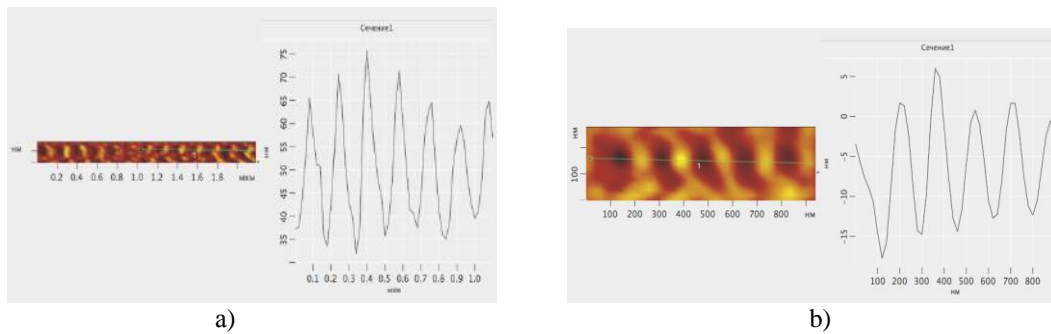


Fig.4. 2D –images of fragments and profile diagram corresponding to them along blade hand of VdW-surface; a)-GaSe<Ag> and GaSe<Sn>

The preparation process of VdW-surface for investigation with use of adhesive ribbon or edge

probably leads to appearance of broken bonds and other structure defects on separated VdW-surfaces which

appear in the result of deformation at their bend. The formation of each type of substructure takes place not only under the influence of internal efforts but under of dislocation redistributions at their interaction between each other.

VdW-surface obtained after its chipping and exposure on the air during not more 2 min, presents itself the corrugated surface with roughness not more than 30 nm (fig.3). The corrugation complex character the profile of which is given on fig.4 concentrates our attention. This is sequence of maximums of different amplitudes.

One can suppose that during LC exposure on air (~2 min) on surface (0001) of GaSe single crystal the water and oxygen molecules are adsorbed. The sorption centers of foreign atoms from surrounding medium present themselves the different type defects, in particular, on GaSe chip surface [18]. These molecules can dissociate in the result of chemisorption on broken bonds of VdW-surface. The molecule chemisorption on lattice structural defects GaSe and interaction between them with participation of mobile structural defects change LC surface energy [19]. The non-equilibrium system of defects and adsorbed particles on VdW-surface strives for equilibrium by the way of self-organization forming the surface with minimal energy [20,13]. At such processes the space ordered corrugated structure which is observed on GaSe VdW-surface, forms. One can suppose that corrugated surface forms by the way of self-organization

in the result of carrying out of cooperative dislocation processes in basic and pyramidal crystallographic planes in LC upper layers [13].

4. CONCLUSION

The striving for minimum of dislocation subsystem total energy is the reconstruction driving force (self-organization) of deforming structure of crystal VdW-surface. The total energy is consisted of separate dislocation energies and energy of their interaction. At increase of dislocation number, the distance between them decreases increasing the forces of their interaction, the collective phenomena role increases that leads to self-organization in similar systems. The energy decreases because of dislocation union into big scale structures. The dislocations before the union have the bigger energy in comparison with after it. It is profitable for dislocations to be energetically united. The agreed (self-organization) behavior is observed in dislocation structure system that leads to VdW-surface corrugation and appearance of pyramidal nano-formations. The corrugated VdW-surface can have the unique properties similar to multi-atomic graphite (graphen) layer to which the wide practical use in nano-technology is predicted, and pyramidal nano-formations can be applied as quasi-one-dimensional structures necessary for preparation of cathode-luminescent light sources in rapid developed nano-technology.

-
- [1] R.H. Williams, A.J. McAvej. *J. Vac. Sci / Technol.*, **2**, 867(1972).
- [2] Q.A. Medvedkin, Yu.B. Rud, M.A. Tairov. Poluprovodnikovie kristalli fotokristalli fotopriemnikov lineyno polyarizovannoqo izlucheniya. Tashkent. 1992. s. 295. (In Russian)
- [3] N.M. Mextiev, Yu.B. Rud, E.Yu. Salaev. // *Fizika I texnika poluprovodnikov*. 1978. T. 12. № 8. s. 1566-1570. (In Russian)
- [4] A.Yu. Zavrajnov, D.N. Turchen. *Kondensirovannie sredi I mejfaznie qranichi*. 2,190 (1999)]. (In Russian)
- [5] S.I. Drapak, S.V. Qavrilyuk, Z.D. Kovalyuk, O.S. Litvin. *FTP* **42**, 4, 423 (2008). (In Russian)
- [6] D.A. Bonnell, J.Garra. *Rep. Prog. Phys.* **71**, 155308 (2008).
- [7] A.M. Pashayev, B.Q. Taqiev, A.A. Safarzade. *Osobennosti strukturi poverxnostey sloistix kristallov GaSe<Sn>*. *Ximiya, fizika I texnologiya poverxnosti*. **T.2.№3.S.395-398**. (2011). (In Russian)
- [8] B. Baranowski, S.Yu. Zaginaichenko, D.V. Schur, V.V. Skorokhod, A. Veziroglu. Springer, Netherlands (2009). P. 765.
- [9] A.Yu. Zavrajnov, D.N. Turchen. *Kondensirovannie sredi I mejfaznie qranichi*. 1, 2, 190, (1990). (In Russian)
- [10] E. Wisotski, A. Klein, W. Jaegermann. *Thinn Solid Films* **380**, 263 (2000).
- [11] Z.D. Kovalyuk, A.P. Baxtinov, V.N. Vodopyanov, A.V. Zasloukin, V.V. Netyaga. In: *Carbon nfnomaterials in clean enerhy hydrogen systems / Eds B. Barckocmanowski, A. Veziroglu*. Springer, Netherlands (2009)/P. 765.
- [12] Q.A. Malqin. *FTT* **49**, 8, 1392 (2007). (In Russian)
- [13] A.M. Pashayev, B.Q. Taqiev, F.K. Aleskerov, K.Sh. Kahramanov, A.A. Safarzade. *Nanostukturivannie qibridnie strukturi na osnove $A^V_2B^{VI}_3$ <primes>*. «Termoelektrichestvo». №2. 34-44. (2011). (In Russian)
- [14] O. Lang, F.A. Rlein, C. Pettenkofer, W. Jaegermann, A. Chevy. *J. Appl. Phys.* **80**, 3817 (1996).
- [15] E. Spiecker, S. Hollensteiner, W. Jager, A.K. Schmid, A.M. Minor, U. Dahmen. *Abstracts of E-MRS 2005 Spring Meeting. Symp.*
- [16] A.I. Dmitriev, Q.V. Lashkarev, Z.D. Kovalyuk, *Nanosistemi nanomateriali, nanotexnologii*, **4,2**, 407 (2006). (In Russian)
- [17] E. Wisotski, A. Klein, W. Jaegermann, A. Chevy, *J. Appl. Phys.* **80**, 3817 (1996).
- [18] S.I. Drapak, S.V. Qavrilyuk, Z.D. Kovalyuk, O.S. Litvin. *FTP* **42**, 4, (2008). (In Russian)
- [19] A.I. Dmitriev, V.V. Vishnyak, Q.V. Lashkarev, Z.D. Kovalyuk, V.L. Karbovskiy, A.P. Baxtinov. “Issledovanie morfoloqii Van-der-Vaalsovoy poverxnosti monokristalla InSe” *FTT*, **53**, 3, (2011). (In Russian)
- [20] Q.A. Malqin. *FTT* **49**, 8, 1392 (2007).(In Russian)

Received: 14.02.2013

ANALYSIS OF MAIN ARTIFACTS IN SCANNING PROBE MICROSCOPY (II)

S.D. ALEKPEROV^{1,2}¹The MSU branch named after M.V. Lomonosov
AZ-1141, Baku, F.Agayeva 14²G.M. Abdullayev Institute of Physics
National Academy of Sciences of Azerbaijan
AZ-1143, Baku, H.Javid,33
e-mail: sdalekperov@mail.ru

In article the methodology consideration of experiment carrying out in the region of scanning probe microscopy (SPM) is done, the main parameters influencing on image quality are revealed. In order to reveal the artifact reason, the main components of SPM signal which are divided on 5 groups, are considered: useful signal; noises connected with external influences and temperature drift; distortions connected with piezoceramics and piezoceramics imperfectness; probe geometry influence; equipment noises. The main methods on elimination and minimization of given artifacts are considered. In second part of the article the SPM formation mechanisms of surface images.

Keywords: scanning probe microscopy (SPM); scanning tunneling microscopy (STM); atomic force microscopy (AFM).

PACS: 81.05.Je, 81.70.-q

III. The main processing algorithms of SPM images

The noises are in almost all SPM images under method specifics. This is connected with: 1) instability of probe-sample contact at the scanning; 2) external acoustic disturbances and 3) noises of electric equipment (mainly, these are noises of high-sensitive input amplifiers), always presenting at measurement of weak signals. The distortions into images are also introduced because of probe thermal drift relatively the sample, non-linearity and creep in piezoceramic elements from which the scanner is done. Concerning it, the special digital image processing is required for obtaining of SPM images of high quality and carrying of their qualitative analysis. In spite of the fact that processing technology of SPM images mainly is similar with general approach to image processing, though, there are essential differences connected with the specificity of their obtaining.

§ 1. The formation mechanism of SPM images

The surface scanning process in scanning probe microscope (SPM) includes in itself the following stages (fig.1). The motion probe moves along the line firstly in direct and further in reverse direction (Horizontal scanning). The probe motion is carried out with the help of scanner by small steps under the influence of saw tooth voltages formed by numerical-analogue transformers. The information registration about the surface topography is carried out on direct pass. The information obtained with the help of SPM is saved in the form of SPM cadre – two-dimensional massive of integral numbers a_{ij} (matrix). The physical meaning of the given numbers is defined by that value which is quantified in scanning process. The definite surface point in scanning filed limit corresponds to each value of index couple ij . The surface point coordinates are calculated with the help of simple amplification of corresponding index on distance value between points in which the information recording is carried out:

$$x_i = x_0 \times i, \quad y_j = y_0 \times j.$$

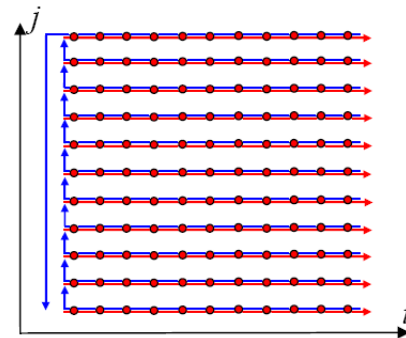


Fig.1. The schematic image of scanning process. The direction of scanner direct motion is designated by red color hands. The scanner reverse motion is designated by blue color hands. The information registration is carried out in points on direct pass [1].

Here x_0 and y_0 are distances between neighbor points along X and Y axes in which the information recording is carried out. As a rule, SPM images present themselves the quadratic matrix having the dimension 2^n (mainly 256×256 and 512×512 elements).

The visualization of SPM images is carried out by computer graphics mainly in the form of three-dimension (3D) and two-dimensional (2D) of brightness images. At 3D visualization the surface surface-mapping $Z=f(x,y)$ corresponding to SPM data is constructed in axonometric perspective with the help of pixels and lines. In addition to this the pixel lighting methods corresponding to different height of relief topography are used.

The modeling of surface illumination conditions by point source situated in some space pint above the surface (fig.2) is the more effective color method of 3D images. One should emphasize the small-scale relief roughnesses. The scaling and 3D rotation of SPM images are realized by also computer processing means and graphics. At 2D visualization the color corresponds to each surface point $Z=f(x,y)$. The gradient palettes, in which the image color is carried out by definite color tone in the correspondence with the height of surface point, are widely used.

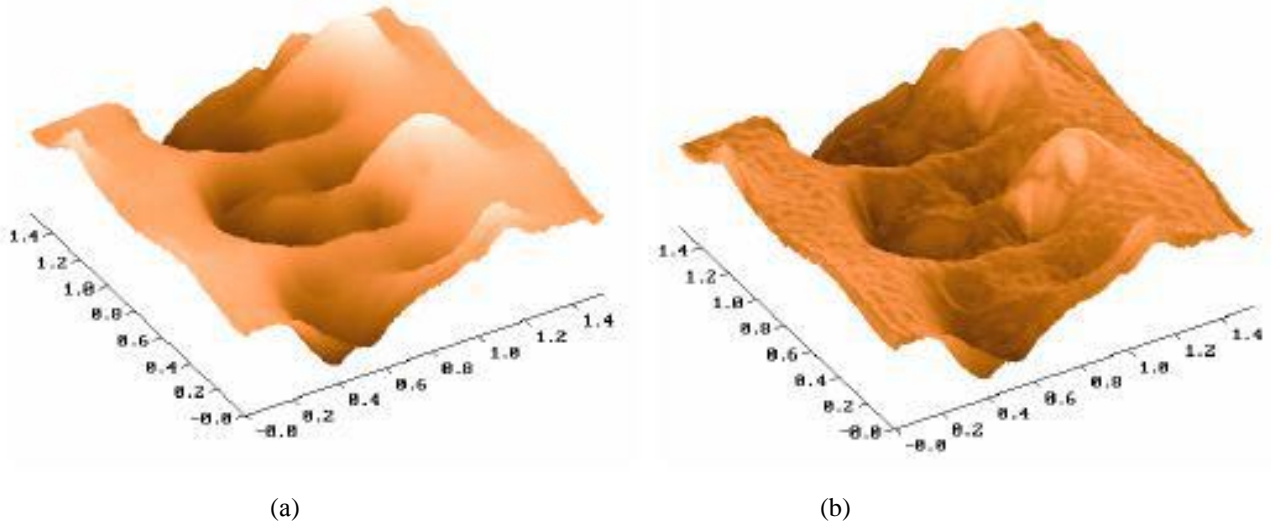


Fig.2. 3D visualization of surface topology with illumination by height (a) and with side illumination (b) [2].

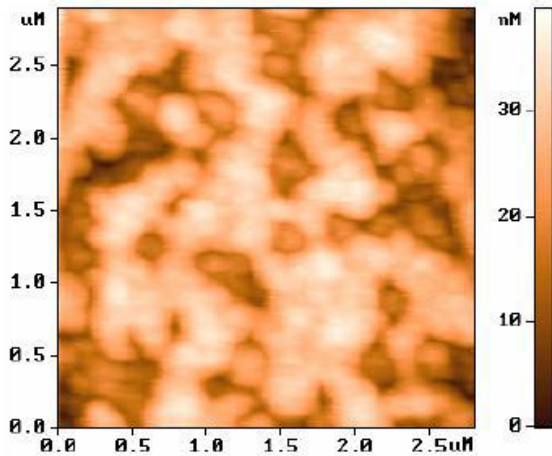


Fig.3. The brightness 2D image [3].

The 2D image of surface part is given for the example on fig.3. The local SPM measurements as a rule are conjugated with dependence registration of investigated values on different parameters [4-6]. For a example, these are dependences of electric current value through probe-surface contact on applied voltage, dependences of different parameters of probe force interaction on probe-sample distance and etc. The given information is saved in the form of vector massifs or matrixes by dimension $2 \times N$. For their visualization in microscope software support the series of standard means of function plot images is provided.

§ 2. The difference of constant inclination

The surface images obtained with the help of probe microscopes, as a rule, have the general inclination. This can be caused by some reasons. Firstly, the inclination can appear in the result of sample inaccurate establishment relatively probe; secondly, it can be

connected with temperature drift which leads to probe shift

Relatively the sample; thirdly, it can be caused by non-linearity of piezo scanner movements [7]. On inclination image the big value of usable space in SPM image is spent so that image small details become invisible ones. For elimination of the given disadvantage, the difference operation of constant inclination is carried out (fig.4). For this on the first stage by least square method the approximating plane $P^{(1)}(x,y)$ having the minimal inclinations on surface topography $Z=f(x,y)$ (fig. 5), is found. Further, the difference of the given plane from SPM image is carried out. The difference one must rationally carried out by different methods in the dependence on inclination nature. If the inclination in SPM image is caused by sample inclination relatively to probe axis, then one must carry out the plane turn on angle corresponding to the angle between normal to \vec{n} plane and Z axis; surface coordinates $Z=f(x,y)$ transform in the correspondence with space turn transformations.

However, at the given transformation the surface image obtaining in the form of multifunction $Z=f(x,y)$ is possible. If the inclination is caused by thermodrft then the inclination difference procedure is led to difference of plane Z-coordinates from Z-coordinate of SPM image:

$$Z'_{ij} = Z_{ij} - P_{ij}^{(1)}.$$

This allows us to save the right geometric relations in X, Y plane between objects in SPM image. In the result of this the massive with less value range is obtained and small image details are shown by big color quantity becoming the more significant. The result of plane difference from real AFM surface image is presented on fig.6.

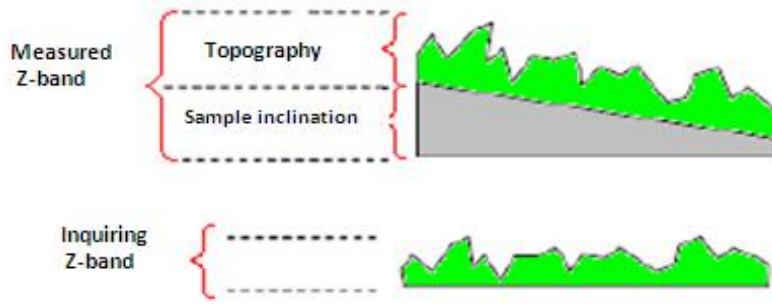


Fig. 4. The elimination of constant inclination (upper figure is up to constant inclination; lower figure is after difference of constant inclination).

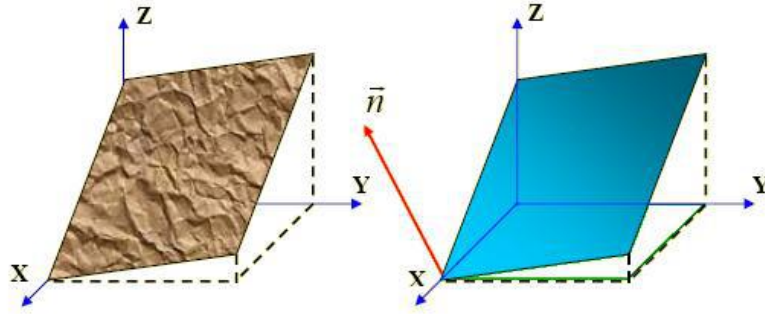


Fig. 5. The difference of constant inclination from SPM surface image [1].

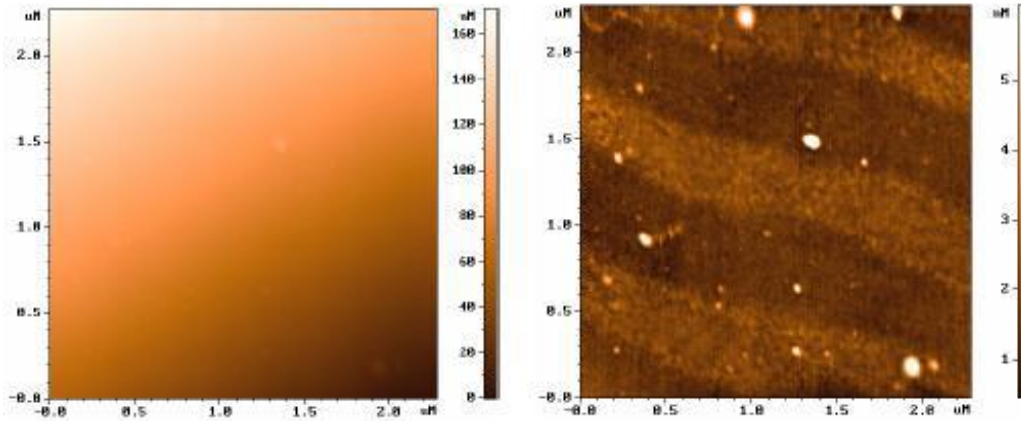


Fig. 6. The difference of inclined plane from real AFM surface image [8].

§ 3. The averaging on lines.

The surface scanning process in scanning probe microscope takes place in so way that information registration frequency in the line strongly differs on line frequency registration (at least in 100 times). This leads to the fact that high-frequency noises are mainly in SPM image lines and low-frequency noises change the position each other [10].

Besides, the probe-sample distance often changes during the scanning in the result of micro-motions in construction elements of microscope measuring head or state change of probe working part (for example, micro-particle probe edge capture from the surface and etc). This leads to the fact that stages parallel to scanning direction connected with the shift of one part of SPM image relatively to other, appear on SPM image (fig.7 (upper image)). One can eliminate from such defects of SPM

images with the help of image adjustment by lines. The average relief meaning is in each scanning line:

$$\bar{Z}_j = \frac{1}{N} \sum_i Z_{ij}.$$

And further the corresponding averages are eliminated from the values in image each line:

$$Z'_{ij} = Z_{ij} - \bar{Z}_j,$$

So that in new image in each line it is equal to zero. This leads to the fact that stages connected with strong changes of average values in the lines, are eliminated from the image. The alignment result by lines of real AFM surface image is presented on fig.7 (lower image).

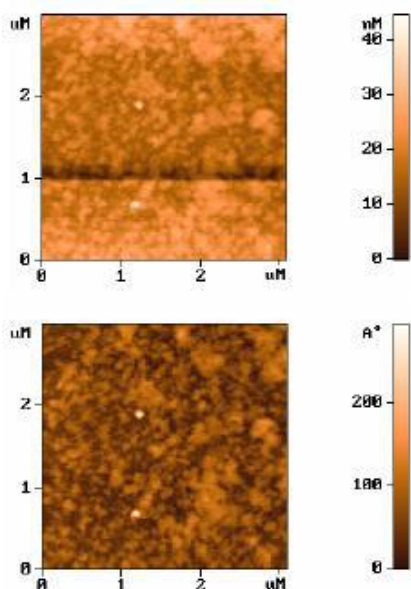


Fig. 7. The surface AFM-images (upper image is up to averaging on lines; lower image is after averaging on lines) [9].

§ 4. The median filtering of SPM images

The median filtration gives the good results at elimination of high-frequency accidental disturbances in SPM images.

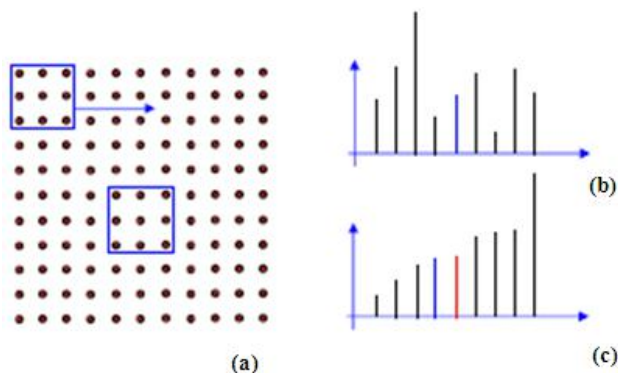


Fig. 8. The principle of operation of median filter with the window 3×3 : (a) is window shift in massif filtration process; (b) is element position in non-selected massif (blue is central element); (c) is element position in non-selected massif (red is new central element) [11].

This is non-linear image processing method the substance of which one can consider the following way. The working filter window consisting from $n \times n$ points is chosen (for definition we take the window 3×3 , i.e.

consisting 9 points (fig. 8)). In filtration process this window shifts by image from the point to point and the following procedure is carried out. The amplitude values of SPM image in the given window points are posited by increase and the value being in the center of selected series in window central point.

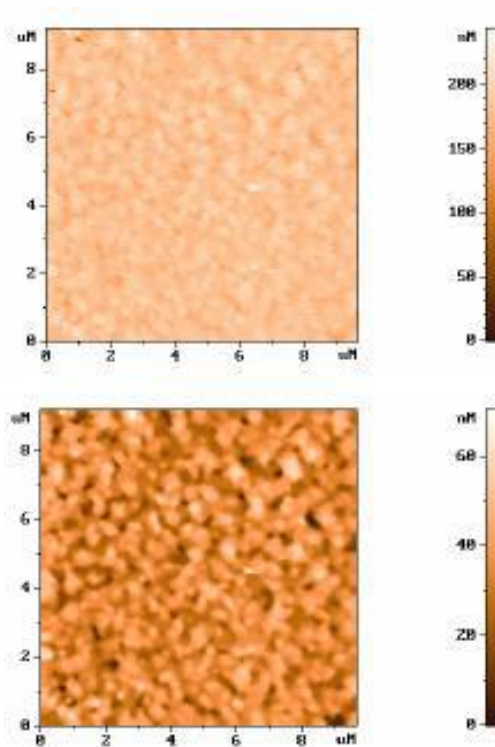


Fig. 9. The median filtration results with window 5×5 of AFM surface image [5].

Further, the window shifts to the following point and selection procedure repeats. Thus, the power accidental bursts and down falls at such selection are always on the edge of selected massive and aren't entered in overall (filtered) image. Note that at such processing the filtered regions which are eliminated in end image by image edges. The result of median filtration of real AFM surface images is presented on fig.9.

Thus, the standard software of probe microscopes includes the enough wide series of means by visualization and processing of SPM data. Besides, the images obtained on scanning probe microscope can be saved in the one of graphic formats that allows us to use the additional possibilities (for example, Furrier-filtration), given by modern packets of computer programs by processing and corrections of images.

[1] Yu. N. Tyurin, A.A. Makarov. Analiz dannix na kompyutere, Moskva, Finansi I statistika, 1995, 256 s. (In Russian)
 [2] M.O. Ivchenko, S.O. Matyushechkin, N.R. Sharipov, R.A. Emelyanenko, R.Q. Sarimsakov. Intellektualniy terminal obrabotki dannix skaniruyushey zondovoy mikroskopii s udalennim dostupom, Moskva, MQTU, 2008, 87 s. (In Russian)

[3] V.K. Nevolin. Osnovi tunnelnozondovoy mikroskopii, Moskva, MIET, 2000, 163 s. (In Russian)
 [4] Edelman. Pribori I texnika eksperimenta. 1989, №5, s. 25-38. (In Russian)
 [5] A.I. Lyamkin, Yu.L. Mixlin, M.B. Qorev. I.N. Flerov, V.D. Fokina. Eksperimentalnie metodi issledovaniy, Krasnoyarsk, 2007, 259 s. (In Russian)

ANALYSIS OF MAIN ARTIFACTS IN SCANNING PROBE MICROSCOPY (II)

- [6] *J.A. Kubby, J.J. Boland.* Scanning tunneling microscopy of semiconductor surfaces// Surface Science Reports, 1996, no. 26, pp. 61-204. B.C.
- [7] *R. Barret, K. Kueyt.* Pribori dlya nauchnix issledovaniy, 1991, №6, s. 3-8. (In Russian)
- [8] *S.A. Rikov.* Skaniruyushaya zondovaya mikroskopiya poluprovodnikovix materialov i nanostuktur, SPB, Nauka, 2001, 53 s. (In Russian)
- [9] *R.Z. Baxtizin, R.R. Qallyamov.* Fizicheskie osnovi skaniruyushey zondovoy mikroskopii, Ufa, BashQU, 2003, 82 s. (In Russian)
- [10] *A.A. Buxarev, N.B. Berdunov, D.V. Ovchinnikov, K.M. Salixov.* Mikroelektronika, 1997, t.26, №3, s. 163-175. (In Russian)
- [11] *U. Prett.* Chifrovaya obrabotka izobrajeniy, Moskva, Mir, 1982, kn. 2, 790 s. (In Russian)

Received: 12.02.2013

SOLUTION OF GENERALIZATION OF PRINCIPAL CHIRAL FIELD PROBLEM FOR THE HIGH RANK SEMISIMPLE ALGEBRAS

M.A. MUKHTAROV

*Institute of Mathematics and Mechanics
370602, Baku, F.Agaev str. 9, Azerbaijan*

New solutions of the principal problem with moving poles are constructed by means discrete symmetry transformations for the algebra $SL(3, C)$.

Keywords: chiral field, high rank semisimple algebras

PACS: 02.30.Jr.

1. Over the last few years self-dual Yang-Mills equation has attracted a fair amount of attention. It has been shown [1-8] that a large number of one, two and (1+2)-dimensional integrable models such as Korteweg-de Vries, N-waves, Ernst, Kadomtsev-Petviashvili, Toda lattice, nonlinear Schrodinger equations and many others can be obtained from the four-dimensional self-dual Yang-Mills equation by symmetry reduction and by imposing the constraints on Yang-Mills potentials.

The universality of the self-dual Yang-Mills (SDYM) model as an integrable system has been confirmed in the paper [9] where the general scheme of the reduction of the Belavin-Zakharov Lax pair for self-duality [10] has been represented over an arbitrary subgroup from the conformal group of transformations of R_4 -space. As the result of this reduction one has the Lax pair representation for the corresponding differential equations of a lower dimension.

The problem of constructing of the instanton solutions in the explicit form for semisimple Lie algebra, rank of

which is greater than two, remains also important for the present time.

The method of integration of SDYM [11] is based on homogeneous Hilbert (Riemannian) problem (HHP) techniques. By means of the same method it was constructed the large class of solutions of the principal chiral field problem with moving poles (PCFMP) [12]. Being reduction of SDYM, the principal field model is investigated in [13] and solutions were obtained their by means of discrete symmetry transformations.

In the present paper we show how the discrete symmetry transformation algorithm is effective in constructing of the solutions of the principal chiral field problem with moving poles in the case of $SL(3, C)$ algebra. The same procedure can be applied to the case of arbitrary high rank semisimple algebra.

2. The system of principle chiral field problem with moving poles

$$(\xi - \bar{\xi})f_{\xi\bar{\xi}} = [f_\xi, f_{\bar{\xi}}] \tag{2.1}$$

can be obtained from the system of self-duality equation

$$W_{z\bar{z}} + W_{y\bar{y}} + [W_z, W_y] = 0 \tag{2.2}$$

by means of substitution

$$\xi = r + it, \bar{\xi} = -r + it, r = \sqrt{y\bar{y} + \left(\frac{z - \bar{z}}{2}\right)^2}, it = \frac{z - \bar{z}}{2},$$

Here, the functions f, W take value in the corresponding semisimple algebra, sub-index denotes differentiation.

Let $f = f^0 H + f^+ X^+ + f^- X^-$, where H, X^\pm are generators of algebra A_1 ,

$$\left[X^+, X^- \right] = H, \left[H, X^\pm \right] = \pm 2X^\pm.$$

Then the system (2.1) for the components f^0, f^\pm takes the following form

$$\begin{aligned}
 (\xi - \bar{\xi})f_{\xi\bar{\xi}}^+ &= 2(f_{\xi}^0 f_{\bar{\xi}}^+ - f_{\bar{\xi}}^0 f_{\xi}^+) \\
 (\xi - \bar{\xi})f_{\xi\bar{\xi}}^0 &= f_{\xi}^+ f_{\bar{\xi}}^- - f_{\bar{\xi}}^+ f_{\xi}^- \\
 (\xi - \bar{\xi})f_{\xi\bar{\xi}}^- &= -2(f_{\xi}^0 f_{\bar{\xi}}^- - f_{\bar{\xi}}^0 f_{\xi}^-)
 \end{aligned} \tag{2.3}$$

The discrete symmetry transformation in this case takes the form:

$$\begin{aligned}
 F^- &= \frac{1}{f^+} \\
 \frac{\partial F^0}{\partial \xi} &= (f^0 - F^0 + \xi) \frac{\partial \ln f^+}{\partial \xi} - \frac{\partial f^0}{\partial \xi} \\
 \frac{\partial F^0}{\partial \bar{\xi}} &= (f^0 - F^0 + \bar{\xi}) \frac{\partial \ln f^+}{\partial \bar{\xi}} - \frac{\partial f^0}{\partial \bar{\xi}} \\
 \frac{\partial F^+}{\partial \xi} &= (f^0 - F^0 + \xi)^2 \frac{\partial \ln f^+}{\partial \xi} - 2f^+(f^0 - F^0 + \xi) \frac{\partial \ln f^0}{\partial \xi} - (f^+)^2 \frac{\partial f^-}{\partial \xi} \\
 \frac{\partial F^+}{\partial \bar{\xi}} &= (f^0 - F^0 + \bar{\xi})^2 \frac{\partial \ln f^+}{\partial \bar{\xi}} - 2f^+(f^0 - F^0 + \bar{\xi}) \frac{\partial \ln f^0}{\partial \bar{\xi}} - (f^+)^2 \frac{\partial f^-}{\partial \bar{\xi}}
 \end{aligned} \tag{2.4}$$

These transformations imply that if $f = (f^+, f^0, f^-)$ is a solution of (2.3), then so is $F = (F^+, F^0, F^-)$.

Now we construct some exact solutions of the eq. (2.3).

Let the initial solution has the following form: $f^- = 0$, $f^0 = \frac{p}{2}(\xi + \bar{\xi})$, f^+ where p is an arbitrary parameter.

From eqs.(2.3) for f^+ we have the following equation

$$(\xi - \bar{\xi})f_{\xi\bar{\xi}}^+ = p(f_{\bar{\xi}}^+ - f_{\xi}^+) \tag{2.5}$$

For $p = -1$ the eq. (2.5) is equivalent to the Laplace equation

$$(\xi - \bar{\xi})f_{\xi\bar{\xi}}^+ = 0, \quad f^+ = \left(\frac{\xi - \bar{\xi}}{\varphi + \bar{\phi}} \right)^{-1}$$

where $\varphi, \bar{\phi}$ are arbitrary functions of independent variables $\xi, \bar{\xi}$ respectively.

Substituting f^+ into the formulas (2.4) and integrating we have

$$F^- = \frac{\xi - \bar{\xi}}{\varphi + \bar{\phi}}, \quad F^0 = \frac{\xi - \bar{\xi}}{2} \frac{\varphi - \bar{\phi}}{\varphi + \bar{\phi}}, \quad F^+ = (\xi - \bar{\xi}) \frac{\varphi \bar{\phi}}{\varphi + \bar{\phi}} \tag{2.6}$$

This solution coincides with solution (6) of [12] which is obtained by HHP.

For the $p = 1$ the eq. (4.5) is reduced to the Laplace equation on function ω defined by

$$\frac{f_{\xi}^+}{(\xi - \bar{\xi})^2} = \omega_{\xi}, \quad \frac{f_{\bar{\xi}}^+}{(\xi - \bar{\xi})^2} = \omega_{\bar{\xi}}, \quad [(\xi - \bar{\xi})\omega]_{\xi\bar{\xi}} = 0, \quad \omega = \left(\frac{\xi - \bar{\xi}}{\varphi + \bar{\phi}} \right)^{-1} \tag{2.7}$$

Integration of eq. (2.7) gives

$$f^+ = (\xi - \bar{\xi})(\phi - \bar{\phi}) - 2 \int^{\xi} \phi d\xi' - 2 \int^{\bar{\xi}} \phi d\bar{\xi}'$$

For $p = \frac{1}{2}$ we have

$$f^+ = \int_L C^+(\lambda) \sqrt{(\lambda - \xi)(\lambda - \bar{\xi})} d\lambda - \int_L C^-(\lambda) / \sqrt{(\lambda - \xi)(\lambda - \bar{\xi})} d\lambda$$

where $C^\pm(\lambda)$ are arbitrary functions of arguments λ in the complex plane, L represents an arbitrary circle. Elements F^\pm are defined by means of first order differential equations.

3. Following Leznov [14], for the case of a semisimple Lie algebra and for an element f being a solution of (2.1), the following statement takes place:

There exists such an element S taking values in a gauge group that

$$\begin{aligned} S^{-1} \frac{\partial S}{\partial \xi} &= \frac{1}{\tilde{f}_-} \left[\frac{\partial \tilde{f}}{\partial \xi}, X_M \right] - \xi \frac{\partial}{\partial \xi} \frac{1}{\tilde{f}_-} X_M \\ S^{-1} \frac{\partial S}{\partial \bar{\xi}} &= \frac{1}{\tilde{f}_-} \left[\frac{\partial \tilde{f}}{\partial \bar{\xi}}, X_M \right] + \bar{\xi} \frac{\partial}{\partial \bar{\xi}} \frac{1}{\tilde{f}_-} X_M \end{aligned} \quad (3.1)$$

Here X_M is the element of the algebra corresponding to its maximal root divided by its norm, i.e.,

$$[X_M^+, X^-] = H, [H, X^\pm] = \pm 2X^\pm, \quad ,$$

– \tilde{f}_- - is the coefficient function in the decomposition of \tilde{f} of the element corresponding to the minimal root of the algebra, $\tilde{f} = \sigma f \sigma^{-1}$ and where σ is an automorphism of the algebra, changing the positive and negative roots.

In the case of algebra $SL(3, \mathbb{C})$ we'll consider the case of three dimensional representation of algebra and the following

form of $\sigma = \begin{pmatrix} 0 & 0 & 1 \\ 0 & 1 & 0 \\ -1 & 0 & 0 \end{pmatrix}$.

The discrete symmetry transformation, producing new solutions from the known ones, is as follows:

$$\frac{\partial F}{\partial \xi} = S \frac{\partial \tilde{f}}{\partial \xi} S^{-1} - \xi \frac{\partial S}{\partial \xi} S^{-1}, \quad \frac{\partial F}{\partial \bar{\xi}} = S \frac{\partial \tilde{f}}{\partial \bar{\xi}} S^{-1} - \bar{\xi} \frac{\partial S}{\partial \bar{\xi}} S^{-1} \quad (3.2)$$

It can be easily shown that the group valued elements at every step of the reduction procedure g_{n+1} and g_n are connected by the relation

$$g_{n+1} = S_n \sigma g_n \quad (3.3)$$

4. Let's represent the explicit formulae of the recurrent procedure of obtaining the group-valued element solutions in the case of $SL(3, \mathbb{C})$ algebra .

At every step S is upper triangular matrix and can be represented in the following form:

$$S_n = \exp(\beta_1)_n X_1^+ \exp(\beta_{1,2})_n X_{1,2}^+ \exp(\beta_2)_n X_2^+ \exp(\beta_0)_n H, \quad (4.1)$$

where $H=h_1+h_2$ and for g_n we use the following parameterization:

$$g_n = \exp(\eta_1^+)_n X_1^+ \exp(\eta_{1,2}^+)_n X_{1,2}^+ \exp(\eta_2^+)_n X_2^+ \exp((t_1)_n h_1 + (t_2)_n h_2) \times \quad (4,2)$$

$$\times \exp(\eta_2^-)_n X_2^- \exp(\eta_{1,2}^-)_n X_{1,2}^- \exp(\eta_1^-)_n X_1^-$$

with

$$g_0 = \exp(\eta_1^+)_0 X_1^+ \exp(\eta_{1,2}^+)_0 X_{1,2}^+ \exp(\eta_2^+)_0 X_2^+ \exp((t_1)_0 h_1 + (t_2)_0 h_2)$$

as an initial solution.

Hereafter, $X_1^\pm, X_2^\pm, X_{1,2}^\pm, h_1, h_2$ are the generators of $SL(3, \mathbb{C})$ algebra.

Following the general scheme we have at

(0)-step:

$$(t_i)_0 = \tau_i^{-1} \equiv v_i, (\eta_i^+)_0 = \alpha_i^{-1}, i = 1, 2, (\eta_{1,2}^+)_0 = \alpha_{1,2}^{-1,0} ;$$

(1)-step:

$$(t_1)_1 = -v_1 + \ln\left(-\frac{\alpha_{1,2}^{-1,0}}{\alpha_{1,2}^{0,0}}\right), (t_2)_1 = -v_2 + \ln\left(-\frac{\alpha_{1,2}^{0,-1}}{\alpha_{1,2}^{0,0}}\right),$$

$$(\eta_1^-)_1 = -\frac{\alpha_2^{-1}}{\alpha_{1,2}^{-1,0}} \exp \delta_1, (\eta_2^-)_1 = \frac{\alpha_1^{-1}}{\alpha_{1,2}^{0,-1}} \exp \delta_2, (\eta_{1,2}^-)_1 = \frac{1}{\alpha_{1,2}^{-1,0}} \exp(\delta_1 + \delta_2),$$

$$(\eta_1^+)_1 = -\frac{\det\begin{pmatrix} \alpha_1^{-1} & \alpha_1^0 \\ \alpha_{1,2}^{-1,0} & \alpha_{1,2}^{0,0} \end{pmatrix}}{\alpha_{1,2}^{-1,0}}, (\eta_2^+)_1 = -\frac{\det\begin{pmatrix} \alpha_2^{-1} & \alpha_2^0 \\ \alpha_{1,2}^{0,-1} & \alpha_{1,2}^{0,0} \end{pmatrix}}{\alpha_{1,2}^{0,-1}}, (\eta_{1,2}^+)_1 = \frac{\det\begin{pmatrix} \alpha_{1,2}^{-1,0} & \alpha_{1,2}^{-1,1} \\ \alpha_{1,2}^{0,0} & \alpha_{1,2}^{0,1} \end{pmatrix}}{\alpha_{1,2}^{-1,0}},$$

$$\delta_i = 2v_i - v_j, i \neq j ;$$

(2)-step:

$$(\eta_1^-)_2 = -\frac{\det\begin{pmatrix} \alpha_2^{-1} & \alpha_2^0 \\ \alpha_{1,2}^{1,-1} & \alpha_{1,2}^{1,0} \end{pmatrix}}{\det\begin{pmatrix} \alpha_{1,2}^{-1,0} & \alpha_{1,2}^{-1,1} \\ \alpha_{1,2}^{0,0} & \alpha_{1,2}^{0,1} \end{pmatrix}} \exp \delta_1, (\eta_2^-)_2 = \frac{\det\begin{pmatrix} \alpha_1^{-1} & \alpha_1^0 \\ \alpha_{1,2}^{0,0} & \alpha_{1,2}^{1,0} \end{pmatrix}}{\det\begin{pmatrix} \alpha_{1,2}^{0,-1} & \alpha_{1,2}^{0,0} \\ \alpha_{1,2}^{1,-1} & \alpha_{1,2}^{1,0} \end{pmatrix}} \exp \delta_2,$$

$$(\eta_{1,2}^-)_2 = \frac{1}{\det\begin{pmatrix} \alpha_{1,2}^{-1,0} & \alpha_{1,2}^{-1,1} \\ \alpha_{1,2}^{0,0} & \alpha_{1,2}^{0,1} \end{pmatrix}} \exp(\delta_1 + \delta_2),$$

$$(\eta_1^+)_2 = \frac{\det\begin{pmatrix} \alpha_1^{-1} & \alpha_1^0 & \alpha_1^1 \\ \alpha_{1,2}^{-1,0} & \alpha_{1,2}^{0,0} & \alpha_{1,2}^{1,0} \\ \alpha_{1,2}^{-1,1} & \alpha_{1,2}^{0,1} & \alpha_{1,2}^{1,1} \end{pmatrix}}{\det\begin{pmatrix} \alpha_{1,2}^{-1,0} & \alpha_{1,2}^{-1,1} \\ \alpha_{1,2}^{0,0} & \alpha_{1,2}^{0,1} \end{pmatrix}_1}, (\eta_2^+)_2 = \frac{\det\begin{pmatrix} \alpha_2^{-1} & \alpha_2^0 & \alpha_2^1 \\ \alpha_{1,2}^{0,-1} & \alpha_{1,2}^{0,0} & \alpha_{1,2}^{0,1} \\ \alpha_{1,2}^{1,-1} & \alpha_{1,2}^{1,0} & \alpha_{1,2}^{1,1} \end{pmatrix}}{\det\begin{pmatrix} \alpha_{1,2}^{0,-1} & \alpha_{1,2}^{0,0} \\ \alpha_{1,2}^{1,-1} & \alpha_{1,2}^{1,0} \end{pmatrix}_2},$$

$$(\eta_{1,2}^+)_2 = \frac{\det \begin{pmatrix} \alpha_{1,2}^{-1,0} & \alpha_{1,2}^{-1,1} & \alpha_{1,2}^{-1,2} \\ \alpha_{1,2}^{0,0} & \alpha_{1,2}^{0,1} & \alpha_{1,2}^{0,2} \\ \alpha_{1,2}^{1,0} & \alpha_{1,2}^{1,1} & \alpha_{1,2}^{1,2} \end{pmatrix}}{\det \begin{pmatrix} \alpha_{1,2}^{-1,0} & \alpha_{1,2}^{-1,1} \\ \alpha_{1,2}^{0,0} & \alpha_{1,2}^{0,1} \end{pmatrix}}$$

Here, $\alpha_1^i, \alpha_2^j, \alpha_{1,2}^{i,j}$ - chains of solutions determined by formulae

$$\tau_i = \sum_{s=1} \tau_i^s(x_s), \quad \alpha_i = \oint_c \alpha_i(\lambda) \exp(-\bar{\delta}_i(\lambda)) d\lambda, \quad i=1,2$$

$$\bar{\delta}_i(\lambda) = \sum_{s=1} \frac{\tau_i^s(x_s)}{\lambda + \theta_s},$$

$$\alpha_{1,2} = \oint_c \alpha_{1,2}(\lambda) \exp(-\bar{\delta}_1(\lambda) - \bar{\delta}_2(\lambda)) d\lambda +$$

$$+ \oint_c \alpha_1(\lambda) \exp(-\bar{\delta}_1(\lambda)) d\lambda \oint_c \frac{d\lambda' \alpha_2(\lambda') \exp(-\bar{\delta}_2(\lambda'))}{\lambda - \lambda'}$$

and the solutions at steps are interrelated as

$$\theta_s(\alpha_i^k)_{x_s} - (\delta_i)_{x_s} \alpha_i^k = (\alpha_i^{k+1})_{x_s}, \quad i=1,2$$

$$\theta_s(\alpha_{1,2}^{0,k})_{x_s} - (\delta_1 + \delta_2)_{x_s} \alpha_{1,2}^{0,k} - (\alpha_1^k)_{x_s} \alpha_2^k = (\alpha_{1,2}^{0,k+1})_{x_s}$$

$$\theta_s(\alpha_{1,2}^{k,0})_{x_s} - (\delta_1 + \delta_2)_{x_s} \alpha_{1,2}^{k,0} - \alpha_1^k (\alpha_2^k)_{x_s} = (\alpha_{1,2}^{k+1,0})_{x_s}$$

-
- [1] R.S. Ward, *Phil. Trans. R. Soc. Lond.*A315, 451 (1985); *Lect. Notes Phys.*, 1987, 280, 106; *Lond. Math. Soc. Lect. Notes Ser.*, 1990, 156, 246.
- [2] L.J. Mason and G.A. J.Sparling. *Phys. Lett.*, 1989, A137, 29; *J. Geom. and Phys.*, 1992, 8, 243.
- [3] S. Chakravarty, M.J. Ablowitz and P.A. Clarkson. *Phys. Rev. Lett.*, 1990, 1085.
- [4] I. Bakas and D.A. Depireux. *Mod. Phys. Lett.*, 1991, A6, 399.
- [5] M.J. Ablowitz, S. Chakravarty and L.A. Takhtajan. *Comm. Math. Phys.*, 1993, 158, 1289.
- [6] T.A. Ivanova and A.D. Popov. *Phys. Lett.*, 1992, A170, 293.
- [7] L.J. Mason and N.M.J. Woodhouse. *Nonlinearity* 1, 1988, 73; 1993, 6, 569.
- [8] M. Kovalyov, M. Legare and L. Gagnon. *J. Math. Phys.*, 1993, 34, 3425.
- [9] M. Legare and A.D. Popov. *Pis'ma Zh. Eksp. Teor. Fiz.*, 1994, 59, 845.
- [10] A.A. Belavin and V.E. Zakharov. *Phys. Lett.*, 1978, B73, 53.
- [11] A.N. Leznov and M.A. Mukhtarov. *J. Math. Phys.*, 1987, 28 (11), 2574; *Prepr. IHEP*, 1987, 87-90. *Prepr. ICTP 163, Trieste, Italy*, 1990; *J. Sov. Lazer Research*, 13 (4), 284, 1992.
- [12] B.N. Aliev and A.N. Leznov. *Acta Appl. Math.*, 28, 201 (1992)
- [13] A.N. Leznov, M.A. Mukhtarov and W.J. Zakrzewski. *Tr. J. of Physics* 1995, 19, 416.
- [14] A.N. Leznov, *Prepr. IHEP*, 1991, 91-145.

Received: 22.02.2013

INFLUENCE OF TEMPERATURE AND DOPING WITH RARE-EARTH ELEMENTS ON ELECTROPHYSICAL PARAMETERS OF A^{III}B^{VI} CRYSTALS WITH LAYERED STRUCTURE

A.Sh. ABDINOV, R.F. BABAYEVA*, N.A. RAGIMOVA, R.M. RZAYEV, S.I. AMIROVA

Baku State University,

**The Azerbaijan State Economic University*

Baku, Azerbaijan Republic

AZ 1145, Baku, Z. Khalilov Street, 23

Phone: (994 12) 5397373, e-mail: abdinov-axmed@yandex.ru,

abdinov_axmed@yahoo.com,

Babaeva-Rena@yandex.ru

The dependence of the electrical parameters (electrical conductivity, Hall coefficient and obility of free charge carriers) on the temperature (T) at 77 ÷ 600 K in pure and doped with rare earths element (Ho, Gd, Dy) atoms with $N_{\text{REE}} \leq 10^{-1}$ at.% in gallium and indium monoselenide crystals (p-GaSe and n-InSe).

It is established that at low temperatures ($T \leq 300 \div 320$ K) in both groups of crystals Hall coefficient (R_H) is independent on T, and dark conductivity (σ_D) and the mobility of free charge carriers (μ) change with activation on T. Herewith differ greatly also values of σ_D and μ for pure samples of different origins, as well as doped samples with different N_{REE} . The values of electrical parameters do not depend on the chemical nature of the impurities introduced, and vary only with doping level.

It is shown that the observed features of the dependence of electrophysical parameters on T and N_{REE} in the studied p-GaSe and n-InSe crystals is due to partial disordering of this semiconductors and the presence chaotic drift barriers in their free energy bands.

Keywords: single crystals, doping, concentration, Hall coefficient, mobility, low-resistance, high-resistance

PACS: 71.20. Nr, 72.20.-i

1. INTRODUCTION

The layered crystal structure, smooth surface and high chemical resistance of the surface of separate layers [1, 2], possession various switching, optical, photoelectric properties in many practical cases do crystals of layered A^{III}B^{VI} semiconductor compounds irreplaceable in comparison with other semiconductors for solid state physics and solid-state electronics.

Besides, weak (Van-der-Vaals) bond between the next layers and absence of dangling bonds on a surface of layers practically exclude possibility of formation of surface levels chipped from large single crystalline ingots of the samples. It allows to make easily from these materials optically homogeneous plates of thickness up to one micron with naturally mirror and atomically smooth surface, as well as to create on their basis heterostructure of various types with using non-conventional approaches [3].

However, despite such ample opportunities and rich physical properties for a science, the problems associated with electric properties and doping these crystals from first day of their invention are problematic. The analysis of works existing to date show that received at research of electric properties and measurement of electrophysical parameters [4-8], as well as at doping with atoms of various chemical elements [1, 9] results in many cases appear contradictory among themselves and not coordinated with theoretical representations on electronic properties of crystalline semiconductors [10].

For the purpose of clarification of the reasons above-stated discrepancies and non-compliances, in the given work we experimentally investigate temperature dependences of electrophysical parameters in pure and weakly-doped by atoms of rare-earth elements (REE) crystals of layered A^{III}B^{VI} compounds.

2. TECHNIQUE AND SAMPLES

As objects of researches undertook pure (specially not doped) and weakly-doped ($N_{\text{REE}} \leq 10^{-1}$ at.%) with REE atoms of gadolinium (Gd), holmium (Ho) and dysprosium (Dy) single crystals of monoselenides of gallium (p-GaSe) and indium (n-InSe) which are the most characteristic and widely studied representatives of this class of semiconductors. Investigated samples in the form of a rectangular parallelepiped in dimensions along "C" axis and on a "C" plane of the crystal $\sim 0.2 \div 1.0$ mm and $2.0 \div 3.0 \times 6.0 \div 8.0$ mm, accordingly, are made by simple chipping from large single crystalline ingots which were grown by a method of slow cooling at a constant gradient of temperature along an ingot [11] and are doped by addition in batch before the beginning of process of synthesis in the necessary quantity of crushed chemically-pure metallic REE to powdery condition [12]. As materials for current contacts served metallic indium (In), tin (Sn) and silver paste made on special technology or aquadag. The special masks made of a thin teflon film were used for creation current contacts. Where if necessary, also clamping tungsten needle-shaped contacts were used.

On preliminary measurements it is established that at high temperatures ($T \geq 360 \div 400$ K) values of electrophysical parameters – dark specific resistance (ρ_D), concentration (n) and mobility (μ) of free charge carriers for various samples (both pure and doped) do not differ almost.

However at low temperatures considerable distinctions both in numerical values, as well as in character of temperature dependences of these parameters for various samples (depending on their origin and doping level) are observed. Herewith investigated samples both on value of ρ_D and N_{REE} , and on character of temperature dependence

are divided on two groups – low- and high-resistance samples.

By means of the experimental installation assembled on the basis of a constant electromagnet with an adjustable homogeneous magnetic induction to 6 kOe at a gap of ~ 4 cm between poles of an electromagnet. By traditional three-probe method [13] were measured the Hall coefficient (R_h) and specific dark conductivity (σ_D) at various temperatures (in 77÷600 K interval). On received at these measurements R_h and σ_D values specific dark resistance ($\rho_D = \frac{1}{\sigma_D}$), concentration ($n = \frac{A}{eR_h}$, where $e = 1.6 \cdot 10^{-19}$ Cl – electronic charge, $A=2$ – the scattering factor) and mobility ($\mu = \sigma_D R_h$) of free charge carriers (current carriers) have been estimated.

At measurements a current through investigated sample passed along layers, and the magnetic field was directed in a direction perpendicular to layers (to "C" plane) of the crystal.

In some cases (in too high-resistance crystals in low temperatures region) values of concentration and mobility of free charge carriers in studied crystals were estimated also on characteristic points of dark static current-voltage characteristics of the investigated samples in a mode of the space-charge limited currents (SCLC), according to corresponding formulas of the Lampert theory for SCLC [14].

The error of measurements did not exceed 3÷5 % depending on accuracy of used electric meters.

3. EXPERIMENTAL RESULTS

As a result of the carried out measurements it is established that in low-resistance ($\rho_{D0} \leq 10^3 \Omega \cdot \text{cm}$ at 77 K) pure (specially not doped) crystals of indium and gallium monoselenides at low temperatures ($T \leq 300$ K) values of σ_D (Fig. 1, curves 1, 2), R_h (Fig. 1, curves 3, 4), or

$$\rho_D = \frac{1}{\sigma_D} \text{ and } n = \frac{1}{eR_h}, \text{ and also } \mu \text{ (Fig. 1, curves 5, 6) do not depend almost on } T \text{ (Fig. 1, curves 1, 2). At high temperatures } \sigma_D \text{ and } R_h \text{ with temperature change with activation, whereas } \mu \text{ falls down under the law}$$

$\mu \sim T^{-\frac{3}{2}}$. Herewith (in the area of high temperatures) activation energy of the dependences $\sigma_T(T)$ and $R_h(T)$ equals to width of the forbidden band (ε_g) of the studied semiconductor. In difference of low resistance crystals in high-resistance pure crystals dependence $\sigma_T(T)$ in the region of low temperatures also has activation character. However activation energy ($\Delta\varepsilon_i$) thus for various samples (depending on ρ_{D0} , i.e. on value of ρ_D at 77 K) is considerably smaller than ε_g and changes in limits 0.10÷0.25 eV and 0.10÷0.35 eV for various samples of GaSe and InSe crystals, accordingly.

In high-resistance pure crystals also as in low resistance crystals the Hall constant at low temperatures almost does not depend on T, more accurately too weak recession of R_h with T is observed, and in the region of high temperatures (where it is observed sharp – activation growth σ_D with temperature) is observed also strong (activation) dependence for $R_h(T)$. Activation energy of thus also equals to width of the forbidden band (ε_g) of the investigated material.

investigated material.

It has appeared that in pure InSe and GaSe crystals at low temperatures a course of curves of dependence $\sigma_D(T)$ (Fig. 1 and 2, curves 1, 2), unlike curves of dependences $R_h(T)$, or $n(T)$ (Fig. 1 and 2, curves 3, 4) are well correlated with a course of curves of dependence $\mu(T)$ (Fig. 1 and 2, curves 5, 6).

As a result of the measurements carried out by us it is established that at high temperatures influence of doping with REE atoms $N_{\text{REE}} \approx 10^{-5} \div 10^{-1}$ at.% on electrophysical parameters (σ_T , R_x and μ) indium and gallium monoselenides crystals and on their temperature dependences is not observed (Fig. 3, curves 4-9).

Also dependences σ_D , R_h and μ on the chemical nature of the entered impurity and in general influence of doping on the Hall coefficient (accordingly concentration of free charge carriers) are not observed under all conditions considered by us. At the same time at low temperatures as value of σ_D (or ρ_D) (Fig. 4, curves 1, 2) and μ (Fig. 4, curves 5, 6), as well as course of their temperature dependence (Fig. 3, curves 1, 3, 4, 6, 7 and 9) are considerably defined by doping level of the sample. In particular with increasing of the doping level at first (at $N_{\text{REE}} \leq 10^{-4}$ and $N_{\text{REE}} \leq 10^{-3}$ at.% for p-GaSe and n-InSe, accordingly) in this temperature region values of σ_T and μ decrease, whereas value of activation energy ($\Delta\varepsilon_i$) dependences of $\sigma_D(T)$ and $\mu(T)$ increase. At the further increasing of doping level reversed situation is observed – σ_D and μ increase, and $\Delta\varepsilon_i$ decreases (Fig. 3).

When N_{REE} reaches 10^{-1} at.%, values of σ_D and μ become even more than having place in low-resistance pure crystals (Fig. 4, curves 7÷10), and $\Delta\varepsilon_i$ – almost equals to zero.

In the region of high temperatures curves of dependences $R_h(T)$, $\sigma_D(T)$ and $\mu(T)$ for various samples in both groups investigated (in pure and doped) crystals almost merge. Herewith also values of these parameters for various samples, chipped from the pure and alloyed crystals – well coincide.

It is established that dependences $\sigma_D(N_{\text{REE}})$ and $\mu(N_{\text{REE}})$ in studied materials in the region of low temperatures have non-monotonic character and correlated with each other (Fig. 4).

Besides in both groups of samples (pure and doped) on dependence curves $\sigma_D(T)$ in the temperature region corresponding to transition from low temperature region to high-temperature one, some bay is observed which depth depends from N_{REE} non-monotonic (Fig. 3, curves 5, 6 accordingly).

4. DISCUSSION

From the received experimental results follows that in pure (specially not doped) indium and gallium monoselenide crystals absolute value of mobility of free charge carriers, as well as a course of its temperature dependence in the region of low temperatures depend on value of initial dark specific conductivity (σ_{D0}), i.e. on value of σ_D at 77 K. Herewith investigated samples on characters of dependences of $\sigma_T(T)$ and $\mu(T)$ are distinctly divided in two groups: low-resistance ($\rho_{T0} = \frac{1}{\sigma_{T0}} \leq 10^4 \Omega \cdot \text{cm}$) and high-resistance ($\rho_{D0} > 10^4 \Omega \cdot \text{cm}$).

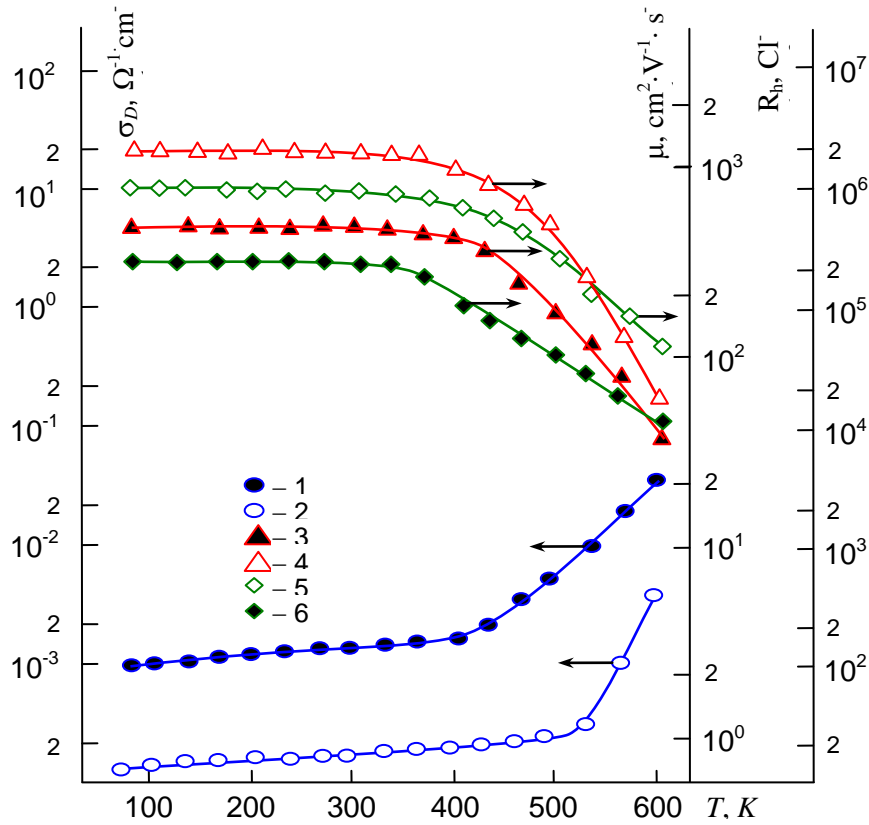


Fig. 1. Temperature dependence of dark specific conductivity (curves 1 and 2), Hall coefficient (curves 3 and 4) and mobility of free charge carriers (curves 5 and 6) in pure (special non-doped) low-resistance n-InSe crystals (curves 1, 3 and 5) and p-GaSe (curves 2, 4 and 6).
 $\rho_{T0}, \Omega \cdot \text{cm}$: 1, 3, 5 - $5 \cdot 10^2$; 2, 4, 6 - $2 \cdot 10^3$.

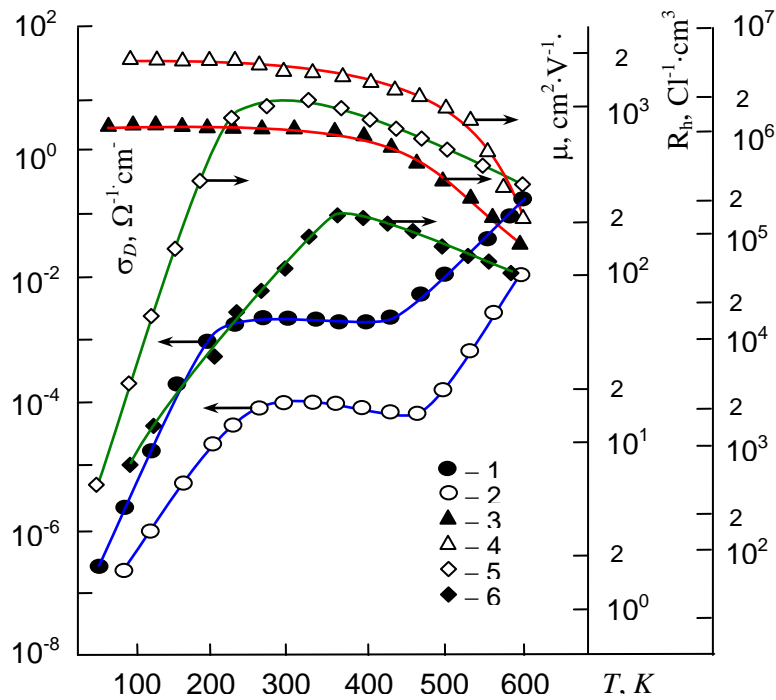


Fig. 2. Temperature dependence of dark specific conductivity (curves 1 and 2), Hall coefficient (curves 3 and 4) and mobility of free charge carriers (curves 5 and 6) in pure (specially non-doped) high-resistance n-InSe crystals (curves 1, 3 and 5) and p-GaSe (curves 2, 4 and 6).
 $\rho_{T0}, \Omega \cdot \text{cm}$: 1, 3, 5 - $5 \cdot 10^2$; 2, 4, 6 - $2 \cdot 10^3$.

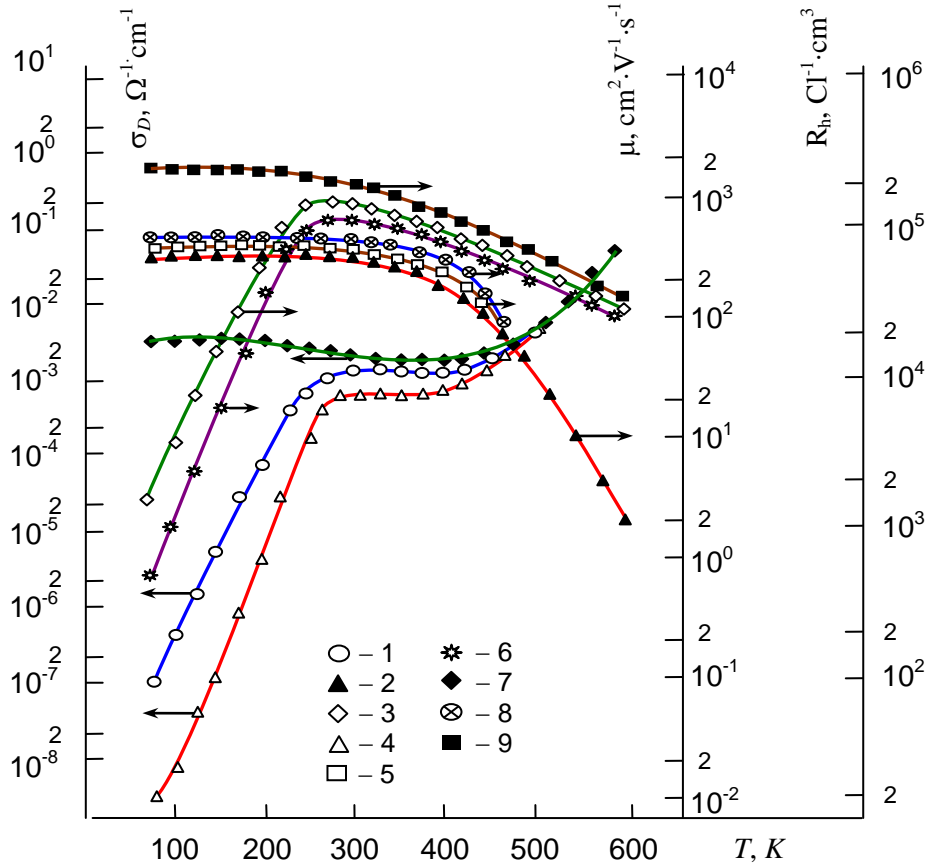


Fig. 3, a. Temperature dependence of dark specific conductivity (curves 1, 4 and 7), Hall coefficient (curves 2, 5 and 8) and mobility of free charge carriers (curves 3, 6 and 9) in n-InSe<REE> crystals. N_{REE} , at. %: 1, 2, 3 - 0; 4, 5, 6 - 10^{-3} ; 7, 8, 9 - 10^{-1} . REE - Dy.

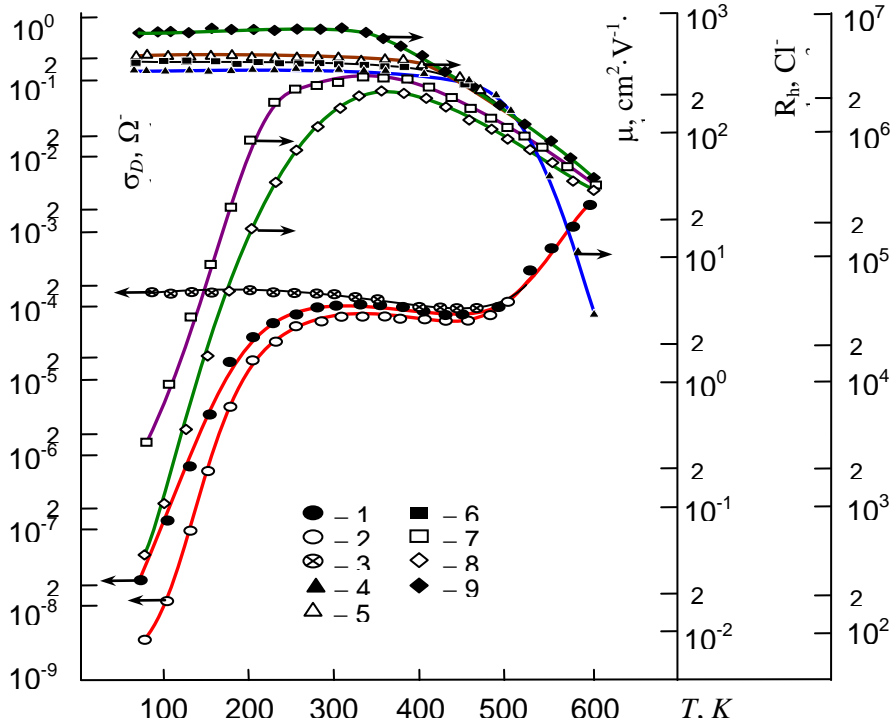


Fig. 3, b. Temperature dependence dark specific conductivity (curves 1, 4 and 7), Hall coefficient (curves 2, 5 and 8) and mobility of free charge carriers (curves 3, 6 and 9) in p-GaSe<REE> crystals. N_{REE} , at. %: 1, 2, 3 - 0; 4, 5, 6 - 10^{-3} ; 7, 8, 9 - 10^{-1} . REE - Ho.

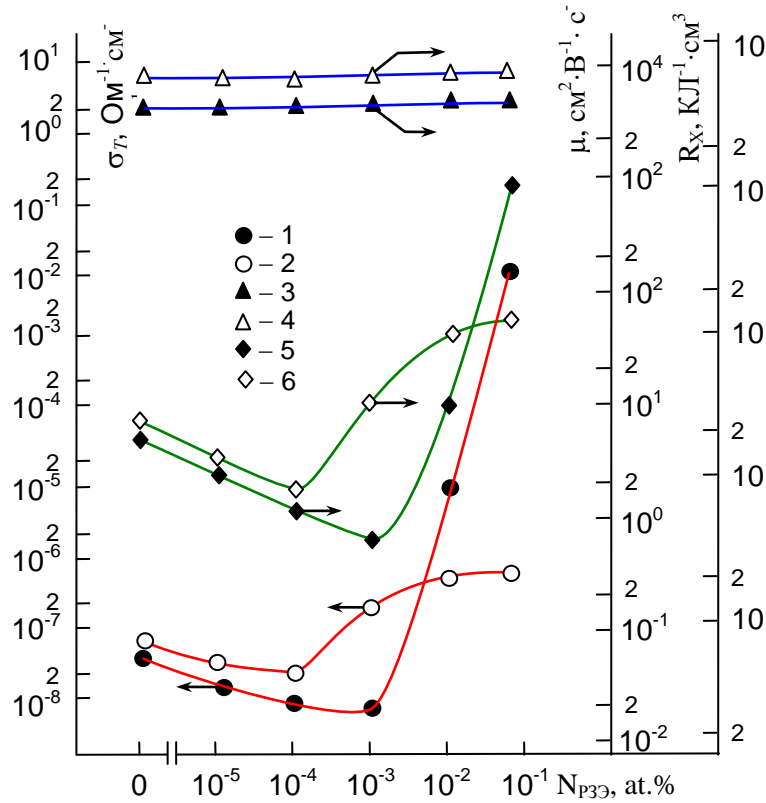


Fig. 4. Dependence of dark specific conductivity (curves 1 and 2), Hall coefficient (curves 3 and 4) and mobility of free charge carriers (curves 5 and 6) in n-InSe <REE> crystals (curves 1, 3 and 5) and p-GaSe <REE> (curves 2, 4 and 6) on doping level.

Unlike low-resistance crystals, in high-resistance ones at low temperatures dependences of $\sigma_D(T)$ and $\mu(T)$ of activation character are observed. In both groups of crystals in the region of low temperatures dependence of $R_h(T)$ or $n(T)$ is not shown almost. Last allows to conclude that found out in high-resistance crystals at low temperatures dependence of $\sigma(T)$ is not concentration effect (it is not caused by change of concentration of free charge carriers depending on temperature) and is not connected with a thermal emptying of any electroactive impurity level. In non-participation of impurity levels in this dependence specifies also considerably smaller values of μ , than a taken place in low-resistance crystals and activation (instead of power dependence as $\mu \sim T^{3/2}$) character of dependence $\mu(T)$.

It is supposed that thus the role of partial disorder of investigated high-resistance samples dominates owing to which in their free energy zones drift barriers of various dimensions arise. With increase of degree of disorder of a studied crystal, also increase the height of drift barriers, and, accordingly, a value of initial dark specific resistance (ρ_{D0}) the investigated sample also increases. In such partially-disordered crystalline semiconductor for participation in conductivity (in electric current) it is necessary for free charge carriers to break some drift barrier with energy height $\Delta\varepsilon_d$ [15]. Therefore at low temperatures mobility of free charge carriers increases with temperature with activation and its activation energy equals $-\Delta\varepsilon_i \approx \Delta\varepsilon_d$. As at such temperatures intrinsic conductivity yet has not begun, and electroactive impurity levels in the

forbidden band of the studied semiconductor are absent, on same activation law increases with temperature also σ_T . At higher temperatures the intrinsic conductivity begins which prevails any other dependences, i.e. therein σ_T and R_x (or n) become dependent on T with activation, and their activation energy equals to width of the forbidden band of the studied material (ε_g). At such temperatures because of thermal smoothing of a potential relief of free energy bands, also a temperature deleting of drift barriers take place [16]. Therefore, at high temperatures influence of the drift barriers on electrophysical parameters and characteristics disappear. As to found out in the region of transition from low-temperature to high-temperature part (where intrinsic conductivity dominates) of $\sigma_T(T)$ curves decay (bay), in our opinion, it most likely that it is caused by replacement of the activation growth of mobility of free charge ($\mu \sim \exp(-\Delta\varepsilon_i/kT)$) with its decay under the power law ($\mu \sim T^{-3/2}$).

Concerning the reason of influence doping with REE atoms on electrophysical parameters of gallium and indium monoselenide crystals, it is possible to tell the following. Absence in the region of low temperatures dependence of value R_h (or n) on T in the crystals doped with REE atoms allows to say that at values N_{REE} considered by us in studied crystals electroactive impurity levels does not create, and doping changes only a condition for drift (moving) of free charge carriers. It is supposed that this circumstance also is connected with dependence of degree of disorder of these semiconductors, or amplitudes of potential fluctuation of their free energy bands

(the dimensions of drift barriers) on doping level. As a result of the last appropriately change also the value of mobility of free charge carriers, as well as the value of initial specific dark conductivity of the investigated sample. Apparently, at $N_{\text{REE}} \leq 10^{-4}$ at.% and $N_{\text{REE}} \leq 10^{-3}$ at.% for gallium and indium monoselenide crystals, accordingly entering into inside of layers, owing to a segregation REE ions accumulate on borders of initial large-scale defects and increase their dimensions. As appropriate increases energy height of drift barriers ($\Delta\varepsilon_d$) and decreases the value of mobility of free charge carriers. At higher levels of doping (at $N_{\text{REE}} > 10^{-3}$ at.%) ions of the entered impurity already gradually are distributed on all volume of the sample within layers. Thereof, degree of disorder of the investigated sample and accordingly, height of drift barriers in them gradually decrease, and mobility of free charge carriers increases with respect to initial value (existing in pure and more weak-doped crystals). At $N_{\text{REE}} \approx 10^{-1}$ at.% p-GaSe <REE> and n-InSe <REE> crystals substantially approach to a status of the quasi-ordered crystal. Therefore at such levels of doping with REE atoms electrophysical parameters and their temperature dependences in these crystals correspond to a case, existing in low-resistance crystals with insignificant fluctuation of potential in free energy bands.

5. THE CONCLUSION

- Divergence of values of electrical conductivity and mobility of free charge carriers, as well as a course of their temperature dependence at low temperatures in various samples of gallium and indium monoselenide crystals are caused with presence of chaotic drift barriers in their free energy bands associated with spatial inhomogeneity (partial disorder) of the investigated semiconductors;

- Influence of weak doping ($N_{\text{REE}} < 10^{-1}$ at.%) gallium and indium monoselenide crystals with atoms of rare-earth elements REE (in particular – with Ho, Gd and Dy atoms) on their electrophysical parameters and characteristics are not associated with formation any new, or growth of concentration already existing electroactive impurity levels, and it is associated only with change of degree of regularity of the investigated sample depending on doping level (N_{REE});

- With increasing of doping level with REE atoms non-monotonically changes degree of disorder of these crystals and parameters of drift barriers in them, and last in turn leads to non-monotonic change the value of μ (and accordingly σ_{D0}) and to detection of features of temperature dependence of electrophysical parameters.

-
- [1] Z.S. Medvedev. Chalcogenides of elements III subgroups of periodic system. M: Science, 1968, - 214 p. (in Russian).
- [2] N.H. Abrikosov, V.F. Bankina, L.V. Poretskaya, E.V. Skudnova, S.N. Chizhevskaya. Semiconductor chalcogenides and alloys on their basis. M: Science, 1975, - 220 p. (in Russian).
- [3] V.L. Bakumenko, Z.D. Kovalyuk, L.N. Kurbatov, et al. Research of heterojunctions InSe-GaSe prepared by landing to optical contact. I. Electric characteristics of non-illuminated junctions // Fizika i Technika Poluprovodnikov, 1980, v. 14, No. 6, pp. 1115-1119 (in Russian).
- [4] S.M. Atakishiyev, G.A. Akhundov, M.G. Aliyev. On electric properties of InSe single crystals. In: «Physical properties of $A^{\text{III}}B^{\text{V}}$ and $A^{\text{III}}B^{\text{VI}}$ semiconductors». Baku: «Elm», 1967, pp. 365-369 (in Russian).
- [5] P.I. Savitsky, Z.D. Kovalyuk, I.V. Mityansky. Anisotropy of electrical conductivity in indium monoselenide // Inorganic materials. 1996. V. 32. No. 4. PP. 405-409 (in Russian).
- [6] P.I. Savitsky, Z.D. Kovalyuk, I.V. Mityansky. Thermostimulated change of condition of defects in indium monoselenide // Inorganic materials. 1997. V. 33. No. 9. pp. 1062-1066 (in Russian).
- [7] M.S. Vinogradov, V.A. Barshak, A.V. Imatov. Anomalous dependence of the dark current in gallium selenide // Fizika i Technika Poluprovodnikov, 1981, V.15, No. 10, PP. 2081-2083. (in Russian).
- [8] F. Power, X. Bonet, A. Segura, A. Chevy. Electrical conductivity anisotropy in doped n-type indium selenide // Phys. Stat. Sol. (b). 1988. V. 145. No. 1. PP. 261-268.
- [9] S.I. Drapak, Z.D. Kovalyuk. Experimental research of influence of aromatic carbohydrates on specific resistance of indium selenide // Fizika i Technika Poluprovodnikov, 2007, V.41, No. 10, PP. 1214-1217 (in Russian).
- [10] R. Smith. Semiconductors, M: "Mir", 1982, 560 p. (in Russian).
- [11] R.F. Mehtiyev, B. Abdullayev, G.A. Akhundov. A technique of growth of GaSe single crystals and research of their some properties // Doklady AN Azerb.SSR. 1962, V.18, No.6, pp. 11-17 (in Russian).
- [12] A.M. Guseynov, T.I. Sadykhov. Reception of the single crystals of indium selenide doped by rare-earth elements. In: Electrophysical properties of semiconductors and gas discharge plasma. Baku, ASU, 1989, p. 42-44 (in Russian).
- [13] N.F. Kovtanyuk, Yu.A. Kontsevov. Measurement of parameters of semiconductor-materials. M. Metallurgiya, 1970, - 429 p. (in Russian).
- [14] M. Lampert, P. Mark. Injection currents in solids. M: Mir, 1973, 416 p. (in Russian).
- [15] E.D. Golovkina, N.N. Levchenya, A.Ya. Shik. Anomalous temperature dependence of Hall mobility in the compensated semiconductor // Fizika i Technika Poluprovodnikov, 1976, V.9, No. 10, pp. 383-389 (in Russian).
- [16] R.F. Babayeva. On the problem of kinetics of dark current in partially-disorder crystals of $A^{\text{III}}B^{\text{VI}}$ type compounds with layered structure // Bulletin of the Baku University, a series of physical and mathematical sciences, 2009. No 2. pp. 140-146 (in Russian).

Receviad:22.02.2013

CHARACTERIZATION OF ELECTRICAL, OPTICAL AND MORPHOLOGICAL PROPERTIES OF CuInSe_2 THIN FILMS EXPOSED TO PLASMA TREATMENT

K. KOSEOGLU^a, S. ACAR^a, B.G. SALAMOV^{a,b,*},
T.G. MAMMADOV^b and F. DAGDELEN^c

^a *Gazi University, Physics Department, Faculty of Sciences, 06500 Ankara, Turkey*

^b *National Academy of Science, Institute of Physics, AZ-1143 Baku, Azerbaijan*

^c *Firat University, Department of Physics, Faculty of Arts and Sciences, 23169 Elazig, Turkey*

The role of plasma-surface interaction on the structural, optical and electrical properties of CuInSe_2 (*CIS*) thin films is investigated. The films were characterized using atomic force microscopy (*AFM*), X-ray diffraction (*XRD*), absorbance, transmission and electrical measurements. Our results show that the plasma treatment plays important role on the electrical and optical properties of *CIS* films. With treatment of plasma, the transmission increases while the absorption coefficient decreases and the band gap energy values decrease from 1.05 to 0.88 eV. It is established that the resistivity values of *CIS* films at room temperature decreases by three orders of magnitude after the plasma treatment.

Keywords: CuInSe_2 , *AFM*, plasma treatment, band gap.

PACS: 73.61.-r Electrical properties of specific thin films- 68.37.Ps Atomic force microscopy (*AFM*)- 78.66.-w Optical properties of specific thin films

1. INTRODUCTION

CuInSe_2 (*CIS*) is a ternary compound semiconductor that crystallizes in chalcopyrite crystal structure. It has a direct energy gap of ~ 1 eV and it shows good outdoor stability. Because of these properties, *CIS* is one of the most promising materials for solar cells [1]. The absorption coefficient is also extremely high in the Cu-III-VI_2 materials, exceeding 10^5 cm^{-1} over most of the visible spectrum. This is greater than that of any other semiconductor used for photovoltaic applications. From the point of view of device optimization, the absorption coefficient also plays a crucial role in the choice of materials for the absorber layer of a photovoltaic device [2]. *CIS* films could be applied to image pickup devices, as well as solar cells, since high efficient thin-film photoconductors are known to be useful in the photoconductive imaging [3,4]. In a study involving applications of *CIS* films in photovoltaic devices, the prime concern is how to make films, which have desirable electrical and optical properties reproducibly. The chemical reaction of oxygen with photoactive layer material is the major mechanism of degradation of optoelectronic devices and solar cells. Establishing the relationship between the interface properties and the characteristics of elements reveals possible mechanisms of degradation. Controlling the process of etching and oxidation of the surface is important in the production of devices with a certain structure [5].

Plasma etching of *CIS* film is used not only as means of characteristics optimization of fabricated devices but also as a process that allows receiving the information regarding them in thermal stability. It has still not been fully understood how mechanism of surface oxidation occurs during plasma etching of the *CIS* thin films and experimental data in air are contradictory. However, it is well established that these phenomena occur and have a significant influence on the efficiency of solar cells. Annealing of the *CIS* films in air reduces the surface resistance, because it occurs due to surface alignment and healed defects. In an earlier work [6], it was shown that influence of oxygen on different physical parameters of

the *CIS* films leads to formation of indium oxide (In_2O_3) phase which causes changes in electrical and optical characteristics of the systems. The effect of In_2O_3 on the optical properties and its formation on the *CIS* films requires the use of more sensitive methods.

However, when working with the polycrystalline thin films instead of single crystal, one has to be careful while controlling the system parameters as the film can be damaged easily [7]. Sensitivity of a device can be increased effectively by reducing the thickness of semiconductor. In this paper, we report experimentally the dynamics of plasma-induced damage (*PID*) of the *CIS* thin film, applying a dc electric field at room temperature in a planar gas discharge device. For the quantitative analysis of the change in the dynamic feature of *PID* of *CIS* thin films, we have analyzed the quality of the film using spatial distributed *DLE* intensities data showing the surface inhomogeneity and damage in the thin film as function of time. However, a noticeable drift of its parameters may be observed during a long operation in the continuous mode. Apparently, it is connected with a change in semiconductor surface properties during the long-term action of the discharge plasma on the semiconductor electrode of the device [8].

Despite the superior structural properties of *Cu*-rich films [9], their electrical properties are dominated by the presence of *Cu*-selenide secondary phases (e.g. Cu_2Se and Cu_{2-x}Se), which are detrimental for device applications [10,11]. Against this background, it is obvious that a clear understanding of the material properties of these films is an important prerequisite for the production of high efficiency solar cell devices [12].

The basic aspect, focused on in this article, is the effect of the non-thermal plasma treatment on the thin film surface and their consequences for the structural, optical and electrical properties of *CIS* thin films in atmospheric air for the first time to our knowledge. Most microstructural analyses of these polycrystalline materials are limited mainly to *SEM* and *XRD*. In this study, *AFM* imaging and *DLE* have been used to investigate the structural properties of *CIS* films.

2. EXPERIMENTAL

The experimental set-up is shown in figure 1. In planar gas discharge system the CIS film was chosen as a photocathode (5). The CIS film that we used has a circular shape of diameter 20 mm on a glass substrate with a back contact. The soda-lime glass substrate was coated with transparent conductor (ITO) and on top, a CIS (5) film of about 0.25 μm thickness was deposited by triple-ionized beam technique (IBT) in which Cu-, In- and Se-vapor for CuInSe_2 were ionized and accelerated [13]. During the film-deposition, the acceleration voltages for Cu-, In- and Se- beams were maintained at 2 kV and the electron currents for ionization of the Cu-, In- and Se- beams were varied between 0 mA and 150 mA. Source materials employed were Cu, In and Se of 99.9999% purity. Source temperatures of the three crucibles for Cu, In and Se were 1420 $^{\circ}\text{C}$, 980 $^{\circ}\text{C}$ and 320 $^{\circ}\text{C}$, respectively. The substrate temperature was kept at 300 $^{\circ}\text{C}$ by an infrared lamp, and the pressure in the vacuum chamber was maintained at less than 1×10^{-5} Torr for deposition period of 90 minutes. This plate is illuminated with IR light (1) which causes an increase in the photoconductivity. A filter (2) is used to allow the desired spectrum to the cathode. CIS film is important in the formation of image by charged particle flux (electron and ion).

At the end of the CIS film layer, there is a glass plate (9) that is covered with a transparent and conductive SnO_2 layer (8). The sheet resistance of the SnO_2 layer is in the range between 15 and 20 Ω/sq . The SnO_2 and ITO electrodes are connected to an external electric circuit, which consists of a high dc voltage supply, U_0 , and a series resistor, R_1 , that is connected to measure the current in the circuit. By applying a high voltage U_0 between the ITO contact and the SnO_2 layers, a discharge is ignited in the gap. The space between the glass plate and the CIS film is the gas layer. The inner surface of the CIS film is separated from a flat anode by an insulating mica sheet (7) with a circular aperture at its centre. The changeable thickness of the insulator makes it possible to vary the size of the interelectrode gap, d , between 15 and 40 μm . Typical diameters, D , of the electrode areas of the photocathode (or of the gas discharge gap) is 9 mm. The experiments are performed in air and the measurements are carried out at room temperature. Before the gas is injected into the system, the cell is evacuated to $p = 1 \times 10^{-6}$ Torr. A feeding voltage of up to 2.5 kV is applied to the electrodes of the cell.

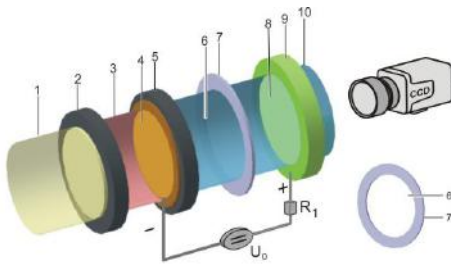


Fig1. Experimental setup. 1. light beam; 2. Si filter; 3. IR light beam; 4. semi-transparent ITO conductor; 5. CIS thin film; 6. gas discharge gap; 7. insulating mica foil; 8. semi-transparent SnO_2 conductor; 9. flat glass disc; 10. UV- visible light beam.

The uniform GDLE over the whole electrode area is observed with currents of more than 100 μA . The maximum E / N is approximately 9 kTd. The GDLE is recorded through a transparent anode with a CCD camera.

An optical absorbance spectrum was taken using a UV-VIS spectrophotometer (Perkin-Elmer Lambda 45), in the photon wavelength range 200-1100 nm. Light signals coming from the samples were collected by an integrating sphere. The thickness of the composite films was measured using an infrared interference method which depends on the reflectance characteristics of the films [14]. The resistivity of CuInSe_2 films was measured by two-point probe method with a Keithley 2400 sourcemeters at room temperature. Surface morphology and grain size were studied using AFM.

3. RESULTS AND DISCUSSION

3.1. STRUCTURAL CHARACTERIZATION AND MORPHOLOGICAL PROPERTIES

Figure 2 shows the XRD pattern of a CIS film. The 112, 220 and 116 diffraction line characteristics of chalcopyrite structure were observed. The three diffraction peaks at the 2θ values of 26.78, 44.64 and 52.88 are associated with the (112), (220) and (116) reflection of the chalcopyrite CIS, respectively. This XRD results clearly indicates that the as-deposited CIS films are crystallized in the chalcopyrite structure. The strong (112) reflection relative to other peaks suggests that these CIS films have a good (112) texture, which is the close-packed plane of the chalcopyrite CIS structure [1]. The relative intensity suggests that the (112) axis is preferentially oriented perpendicular to the film surface.

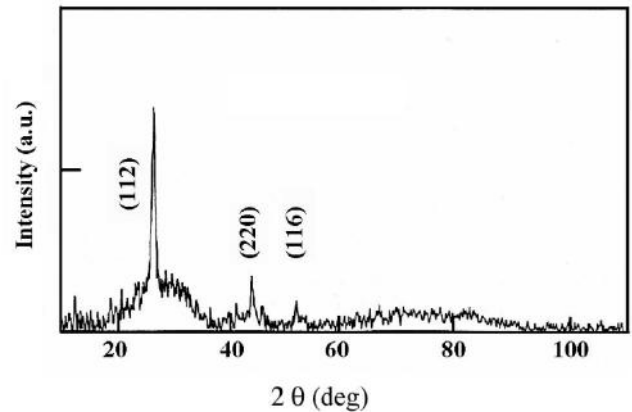


Fig2. The X-ray diffraction pattern of CIS thin film.

The surface morphology of CIS film was studied using the AFM to estimate its surface roughness. Figure 3 shows the surface topographical images recorded for CIS film before and after plasma treatment. In figure 3(a), clusters became apparent besides the crystalline structure in untreated material. Clusters have disappeared after plasma treatment in figure 3(b). However, the surface topography has been composed of clusters of varying sizes with irregular shapes after plasma treatment (Figure 3(b)). It is clear that the surface morphology of the region which was exposed to plasma treatment is not

homogeneous. Inhomogeneous surface is also supported with resistivity measurements.

Roughness can be related to the physicochemical status of the surface under test. Roughness of Cu -rich films was found to be greater than that of In -rich films. One of the reasons for this is identified to be from Cu -agglomerates in Cu -rich films [15]. AFM analyses were used to verify the agglomeration. Thus, roughness could include the physical limit of the solid surface concerned dust, contaminants, subsurface defects etc. which are all resulting in near field complex structures of the diffracted field and the corresponding generated far field propagated modes. In the micron or millimetre range, surface perturbations are spatially coherent (scratches, grooves, grain relief, etc) that is result from the preparation conditions. In [16], Cu -rich films had a surface disturbed with hills and valleys. On In -rich films the topology was of smoother mounts. AFM studies revealed that the surface morphology of these In -rich films is dominated by a high density of relatively small roughly circular clusters with very little height variation from cluster to cluster. This is in sharp contrast to the presence of large, faceted grains in Cu -rich films [12].

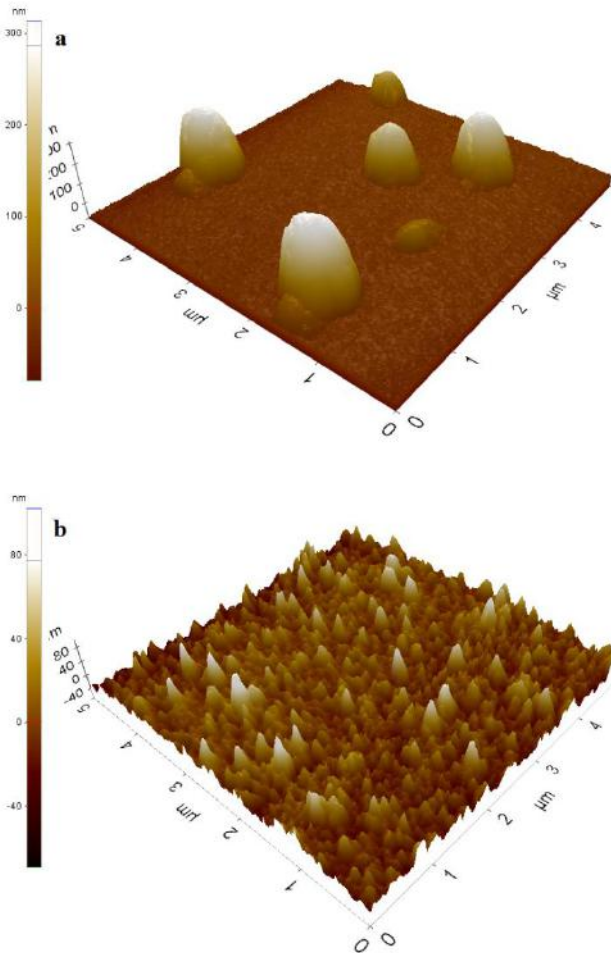


Fig.3. AFM images of the CIS film; a) before plasma treatment, b) after plasma treatment.

It is shown that the PID in a CIS thin film was primarily due to the effectiveness of sputtering and physico-chemical interactions in the discharge gap during the transition from Townsend to the glow type. The surface profilers analysis was carried out to characterize

the surface state of CIS films after plasma treatment, in order to establish the changes in surface roughness. After the plasma treatment process, the CIS films are represented as three-dimensional (3D) charts of the distribution of the DLE intensity as a function of time (see figure 4). The possibilities of the visualization have been evaluated, i.e. a local change in surface inhomogeneity is determined by a local change in DLE intensity. Change of Cu/In ratio in the studied films may cause formation of Cu excess due to In vaporization during plasma process. This causes formation of Cu_2Se and $CuSe$ excess on the surface of CIS , furthermore it leads to change in discharge filamentation and surface inhomogeneity (see figure 4).

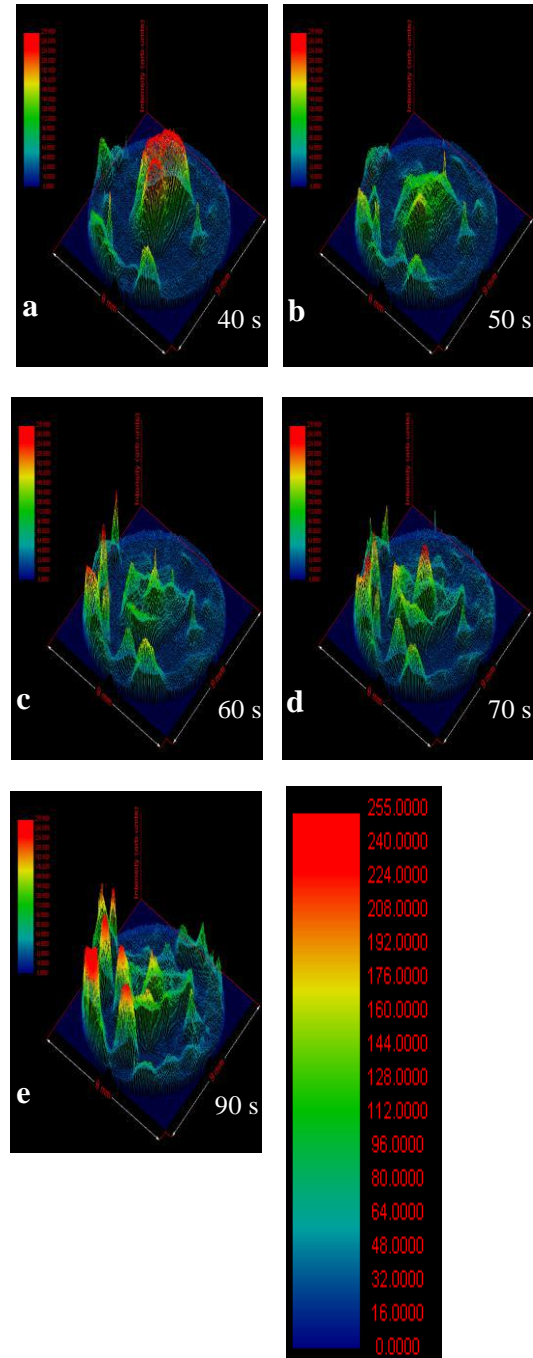


Fig.4. The 3D surface patterns of a $CuInSe_2$ films in the cell.

3.2. OPTICAL PROPERTIES

Transmission spectra in the wavelength range 200-1000 nm for CIS films before and after plasma treatment are shown in figure 5. We think especially *In* segregated from surface CIS samples during the plasma treatment and consequently *Cu/In* ratio increased. It can be seen that as the *Cu/In* ratio increases the transmission will increase. Experimental results show that the plasma etching of the CIS layers is leading to the same effect of annealing in air. This positive influence of plasma etching on the CIS film parameters can be attributed to adsorption and desorption process of oxygen on the grain particles on the surface borders. Nevertheless, the absorbance of all samples has high value in the visible region. Also, the observed increases in the optical transmittance level in *Cu*-rich samples may be due to the existence of $Cu_{2-x}Se$ [17].

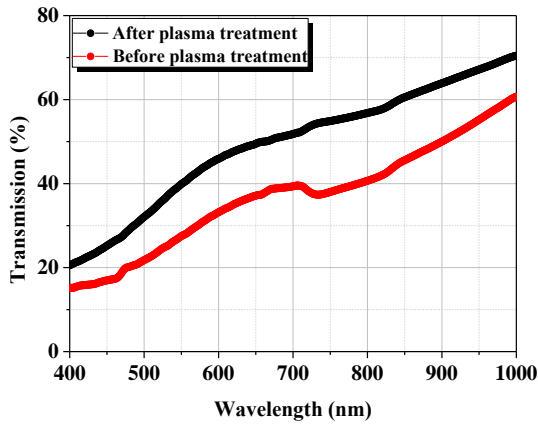


Fig.5. The optical transmission of CIS thin films as a function of plasma treatment.

In an earlier spectroscopy investigation [18], it was established that the change in the value of the absorption coefficient in the CIS films and crystals is not connected with oxide formation. This is due to the fact that if the oxide layer from the sample's surface will be released by plasma etching immediately before to measurement of the absorption, then the value of the absorption coefficient also increased. In study of such films, a significant concentration gradient of selenium near the surface is revealed. Accordingly, changes in the absorption coefficient associated with significant variations in the composition of the film layers.

The optical band gap E_g for direct allowed transitions can be obtained from the graph of $(\alpha h\nu)^2$ versus $h\nu$ [19]. With the treatment of plasma, the band gap energy value decreases from 1.04 to 0.88 eV. This situation is strongly related to the *Cu/In* ratio [17,20].

3.3. ELECTRICAL PROPERTIES

The resistivity of $CuInSe_2$ films is measured at room temperature by two-point probe method before and after plasma treatment. It is clear that resistivity values of the region which expose to plasma treatment is not homogeneous. The variation of the resistivity, ρ , of CIS film is numerically given in table 1. The current filamentation (high current density) primarily has started clusters of given by AFM images in figure 3(a). We think especially *In* segregated from surface CIS samples during

the plasma treatment and consequently *Cu/In* ratio increased. The resistivity is strongly related to the *Cu/In* ratio. The increases of *Cu/In* ratio cause of the decrease in resistivity on the sample. It is seen that from the table 1, resistivity values decrease by three orders of magnitude after the plasma treatment. This result agrees with the resistivity variations reported previously [1]. In [17], *Cu/In* ratio was increased from 0.9 to 1.1 and was observed the resistivity value decrease by five orders of magnitude. The increase of the resistivity when the copper concentration decreases in relation to the indium concentration is a compensation effect due to the excess *In* atoms which act as donors. The observed drastic decrease in resistivity could be attributed to the presence of a high conductivity of $Cu_{2-x}Se$ phase segregated in the grain boundaries [17]. Also, the copper excess causes a whole degeneracy in the deposited films. However, this result clarifies to optical band gap decreasing. It should be noted that, electric characteristics of the CIS layers are determined by interaction of oxygen with natural defects and width of band gaps depends on perfection of crystal structure of the thin film [21].

Table 1. The resistivity of CIS films before and after plasma treatment.

CIS Resistivity (Ωcm)	
Before plasma treatment	After plasma treatment
	1.0×10^4
	8.5×10^4
1.7×10^7	3.5×10^5
	1.1×10^6
	1.2×10^6
	3.3×10^6

4. CONCLUSION

We have investigated the role of plasma-surface interaction on the structural, optical and electrical properties of CIS thin films. XRD analysis revealed that CIS thin films exhibit chalcopyrite phase and preferential (112) orientation. It is found that the plasma treatment plays important role on the electrical and optical properties of CIS films. After plasma treatment, the transmission increases while the absorption coefficient decreases. With the treatment of plasma, the band gap energy value decreases from 1.04 to 0.88 eV. Resistivity values of the region which expose to plasma treatment is not spatially homogeneous and decrease by three orders of magnitude after the plasma treatment. The resistivity of the CIS thin film is strongly related to the *Cu/In* ratio. Change of *Cu/In* ratio in the studied films may cause formation of *Cu* excess due to *In* vaporization during plasma process. This causes formation of Cu_2Se and $CuSe$ excess on the surface of CIS, furthermore it leads to change in discharge filamentation and surface inhomogeneity.

Both the increase of the optical transmittance and the decrease of resistivity require for the improved performance of CIS thin-film. Results of investigation (i.e. interactions of oxygen with surface CIS films and methods of oxidation of this three-componental semiconductor material) allow establishing positive influence of such kind of plasma etching on the parameters of devices on their basis.

ACKNOWLEDGEMENTS

The authors would like to thank Prof. Dr. K. Sato and Mr. K. Tanaka from the Faculty of Technology, Tokyo University of Agriculture and Technology, for supplying

CIS samples. This work was supported by the Gazi University BAP research projects 05/2012-26, 05/2012-19 and 05/2011-28.

-
- [1]. *J.W. Lim, J.H. Choi and I.H. Choi.* J. Korean Phys. Soc. **30**, 293 (1997).
- [2]. *B.J. Stanbe.* Crit. Rev. Solid State Mater. Sci. **27**, 73 (2002).
- [3]. *P. Fan, G.X. Liang, Z.H. Zheng, X.M. Cai and D.P. Zhang.* J. Mater. Sci. Mater. Electron. **21**, 897 (2010).
- [4]. *T. Meyer, F. Engelhardt, J. Parisi and U. Rau.* J. Appl. Phys. **91**, 5093 (2002).
- [5]. *H.W. Schock and U. Rau.* Physica B **308**, 1081 (2001).
- [6]. *U. Rau, D. Braunger, R. Herberholz, H.W. Schock, J.F. Guillemoles, L. Kronik and D.J. Cahen, J. Appl. Phys.* **86**, 497 (1999).
- [7]. *H.Y. Kurt, E. Kurt and B.G. Salamov.* Cryst. Res. Technol. **41**, 698 (2006).
- [8]. *E.L. Gurevich, S. Kittel, R. Hergenröder, Y.A. Astrov, L.M. Portsel, A.N. Lodygin, V.A. Tolmachev and A.V. Ankudinov, J. Phys. D: Appl. Phys.* **43**, 275302 (2010).
- [9]. *L. Gutay, D. Regesch, J.K. Larsen, Y. Aida, V. Depredurand and S. Siebentritt.* Appl. Phys. Lett. **99**, 151912 (2011).
- [10]. *D.F. Marrón, T. Glatzel, A. Meeder, T. Schedel-Niedrig, S. Sadewasser and M.C. Lux-Steiner.* Appl. Phys. Lett. **85**, 3755 (2004).
- [11]. *J. Liu, F. Liu, Y. Lai, Z. Zhang, J. Li and Y.J. Liu.* Electroanal. Chem. **651**, 191 (2011).
- [12]. *V. Alberts, K.T. Hillie and C.M. Demanet.* J. Microsc. **197**, 206 (2000).
- [13]. *K. Tanaka, M. Kosugi, F. Ando, T. Ushiki, H. Usui and K. Sat., Jpn. J. Appl. Phys.* **32**, 113 (1993).
- [14]. *S.M.F. Hasan, M.A. Subhan and K.M. Mannan.* Opt. Mater. **14**, 329 (2000).
- [15]. *R. Jayakrishnan, T. Sebastian, T.T. John, C.S. Kartha and K.P. Vijayakumar, J. Appl. Phys.* **102**, 043109 (2007).
- [16]. *R. Jayakrishnan, P.M. Ratheesh Kumar, C.S. Kartha and K.P. Vijayakumar, Meas. Sci. Technol.* **17**, 3301 (2006).
- [17]. *A.A. Akl and H.H. Afify.* Mater. Res. Bull. **43**, 1539 (2008).
- [18]. *M.R. Balboul, A. Jasenek, O. Chernykh, U. Rau and H.W. Schock.* Thin Solid Films **387**, 74 (2001).
- [19]. *S. Agilan, D. Mangalaraj, S.K. Narayandass and G. Mohan Rao, Physica B* **365**, 93 (2005).
- [20]. *R.R. Philip, B. Pradeep, G.S. Okram and V. Ganesa.* Semicond. Sci. Technol. **19**, 798 (2004).
- [21]. *L. Kronik, U. Rau, J.F. Guillemoles, D. Braunger, H.W. Schock and D. Cahen,* Thin Solid Films **361**, 353 (2000).

Received:19.02.2013

DIELECTRIC RELAXATION AND CONDUCTION OF TlInTe₂ CRYSTAL SUBJECTED TO RADIATION EXPOSURE

**R.M. SARDARLI, O.A. SAMEDOV, P.Sh. AGAYEVA,
A.P. ABDULLAYEV, F.T. SALMANOV, S.Ph. SAMEDOV**

Institute of Radiational Problems of National Academy of Sciences of Azerbaijan

B. Vahabzade 9, AZ 1143.

sardarli@yahoo.com

The investigation of temperature dependence of dielectric loss tangent in TlInTe₂ crystals radiated by γ -quanta shows that at the increase of radiation dose the maximum of dielectric loss tangent shifts to the high temperature region. The activation energy W^a ($D=0$)=0.5 eV and W^a ($D=50$ Mrad) =0.37 eV) of mode jump and its oscillation frequency ($\nu=2 \cdot 10^{12}$ Hz ($D=0$ Mrad) and $\nu=10^{11}$ Hz ($D=50$ Mrad)) which are in frequency region of oscillation spectrum phonon modes, are obtained. It is shown that in TlInTe₂ crystal after radiation by dose 50Mrad the dielectric constant in 6 times and the electric conduction in 3 times exceed the initial value.

Keywords: superior conduction, dielectric constant, dielectric losses, nano-chain, dielectric relaxation, γ -radiation.

PACS: 72.20.-Fr

INTRODUCTION

The triple compound TlInTe₂ is the structural analogue of thallium selenide (TlSe) and crystallizes in volume-centered tetragonal lattice (space group is $I4/mcm$) with parameters: $a=8,075$ Å; $b=6,874$ Å; $Z=4$; $d_p=7,098$ gr/cm³ [1]. This is weakly studied representative of triple analogues of thallium selenide.

Concerning to chemical bond the TlInTe₂ compound formula is written as $Tl^+(In^{3+}Te_2^{2-})^-$. In this compound the In^{3+} ions and their nearest tetrahedral **surrounding** from four Te^{2-} ions form the negatively charged chains - $Te_2^{2-}-In^{3+}-Te_2^{2-}$ along tetragonal axis "c". The univalent Tl^+ ions localize between four chains and have the octahedral **surrounding** from eight ions Te^{2-} . In previous publications [2-8] it is shown that in TlInTe₂ and TlGaTe₂ crystals the conduction has ion (superion) character at temperature higher 300K. It is established that Tl^+ ions diffusing on vacancies in thallium sublattice between nanorods $In^{3+}Te_2^{2-}$ and $(Ga^{3+}Te_2^{2-})$ are responsible for it. The relaxation character of dielectric anomalies that supposes the existence of electric charges weakly connected with it, is established. The dipoles Tl^+ of $In^{3+}Te_2^{2-}$, $(Ga^{3+}Te_2^{2-})$ chains, appearing in the result of thallium sublattice melting and Tl^+ ion jumps from one localized state into another one, are relaxators in TlInTe₂ and TlGaTe₂ crystals at the transition into superior state. The effect induced by the field of crystal transition of TlInTe₂ and TlGaTe₂ into superior state is observed.

In present paper the behavior peculiarities of temperature dependences of dielectric constant ($\epsilon(T)$), electric conduction ($\sigma(T)$) and dielectric dissipation ($tg\delta(T)$) of TlInTe₂ crystal subjected by different doses of γ -radiation, are investigated.

EXPERIMENT TECHNIQUE

The TlInTe₂ compound samples are synthesized by melting of initial components (purity not less 99,99) in vacuumed quartz ampoules and their single crystals are grown up by Bridgman method. The freshly cleaved samples prepared for investigation in which "c" axis is oriented in chip plane, have the rectangular type. Capacitors in which the investigated material plates serve as

dielectric, are prepared for measurements of temperature dependences of TlInTe₂ crystal heat conduction. The capacitor coatings are obtained by marking of silver current-conducting paste on plate surface. Investigations of electric conduction are carried out by impedance numerical measurer E7-25 in temperature interval 100÷450K. After previous measurements of $tg\delta(T)$ и $\epsilon(T)$ samples are subjected to γ -radiation by standard radiation source Co^{60} . The radiation dose accumulates constantly in each of investigated samples by the means of continuous expositions of γ -radiation up to value 100 Mrad.

EXPERIMENTAL RESULTS AND THEIR DISCUSSION

The temperature dependences of dielectric dissipation for TlInTe₂ crystal are given on figures 1 (a,b). The measurements are carried out at measuring field frequencies 10, 100, 500 and 1000 MHz for initial samples (fig.1a) and for samples subjected to γ -radiation of 50 Mrad (fig.1b).

As it is seen from figure 1(a,b) with measuring field frequency increase the values $tg\delta(T)$ shift to more high temperatures and maximum of $tg\delta(T)$ value decreases. The frequency dependences of dielectric dissipation maximal value ($lg\delta_{max}$) on temperature for TlInTe₂ crystal are given on fig.2. The temperature frequency characteristics of dielectric dissipation $tg\delta(\nu, T)$ have clearly expressed peculiarities charactering relaxation processes of Debye type in all investigated temperature region. The last one supposes the existence of electric charges weakly connected with crystal lattice.

For description of relaxation peak of dielectric dissipation one can use the oscillator model with big damping [9,10]. The model is considered the displacements of n particles with e charge in potential wells with the distance between their minimums a and barrier height E . The eigenfrequency ν of particle oscillation in well is the frequency at which the particle jump through barrier is possible, it is less the frequency than particle frequency jumps between minimums ($2\nu e^{-W/kT}$).

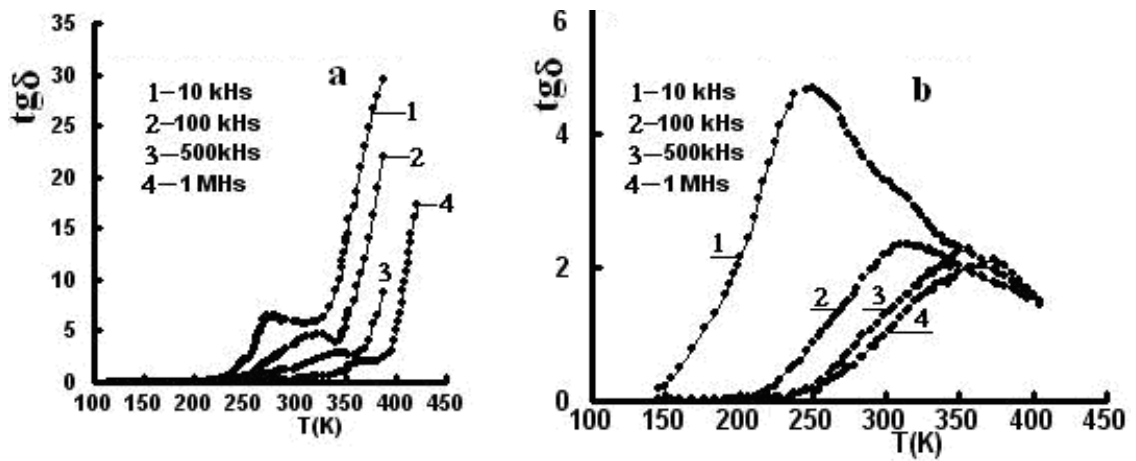


Fig. 1. Temperature dependences of dielectric dissipation for TIInTe₂ (a is 0 Mrad; b is 50Mrad)

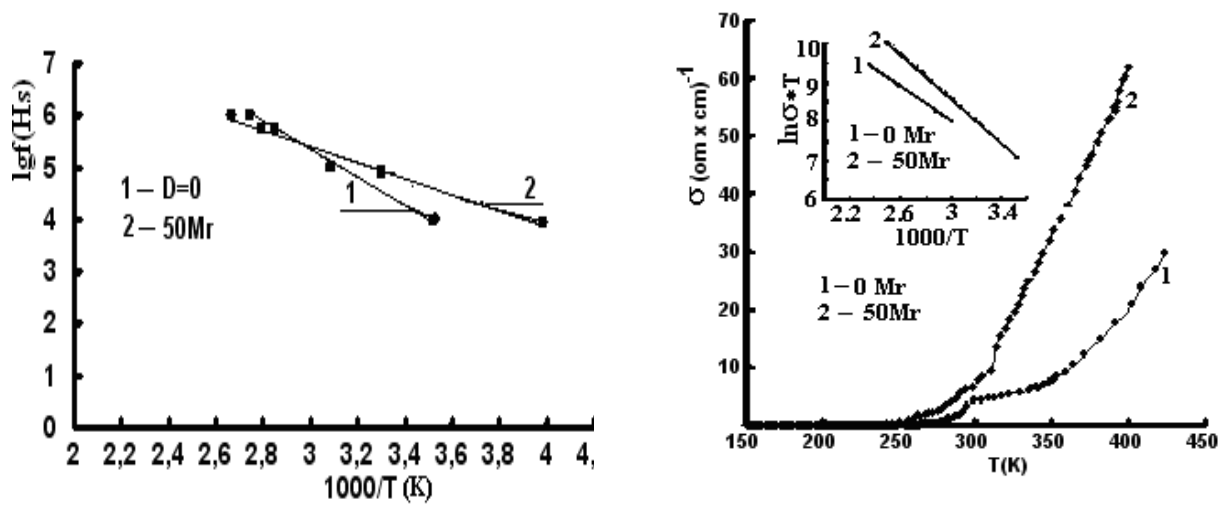


Fig. 2. The frequency of relaxation maximum of dielectric dissipation in function of its reverse temperature for TIInTe₂ (1- 0Mrad; 2- 50Mrad).

Fig. 3. Temperature dependences of electric conduction $\sigma(T)$ for crystal TIInTe₂ treated by γ -radiation (1- 0; 2-50Mrad). The dependences $\ln(\sigma \cdot T)$ on $1000/T$ for initial sample (1) and obtained doze 50 Mrad (2) are given on insertions.

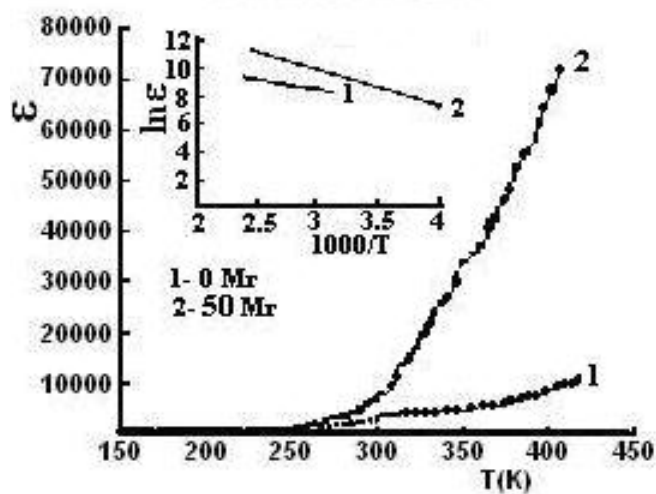


Fig. 4. Temperature dependence of dielectric dissipation $\epsilon(T)$ for TIInTe₂-crystal treated by γ -radiation (1- 0; 2-50Mrad). The dependence $\ln(\epsilon)$ on $1000/T$ for initial sample (1) and radiated doze 50Mrad (2) are given on insertions.

The theoretical consideration shows [9] that relaxation maximum ε on temperature precedes the $\text{tg}\delta$ maximum. This maximum is observed in TlInTe_2 (see [5]), and it is experimentally easily studied as it appears in comfortable frequency intervals (100Hz - 1MHz) and not high temperature (100-450K). Neglecting the open-ended electric conduction in given temperature interval for description of tangent anomaly one can apply the expression [10]:

$$\text{tg}\delta(T) = \frac{\omega e^2 a^2 / \varepsilon_\infty}{kT \left(\frac{\varepsilon_s}{\varepsilon_\infty} + \frac{\omega^2}{4\nu^2} e^{2W/kT} \right)} \cdot \frac{e^{W/kT}}{2\nu} \quad (1)$$

where ε_∞ is dielectric constant on infinite big frequency:

ε_s is statistic dielectric constant.

The extremum finding on temperature for $\text{tg}\delta$ is easily carried out under condition $\frac{\omega}{2\nu} \ll 1, \frac{2W}{kT} \gg 1$ and leads to the equation for temperature maximum.

$$\ln \frac{2\nu}{\omega_{\max}} = \frac{W}{kT} \quad \text{или} \quad \omega_{\max} = 2\nu e^{-W/kT} \quad (2)$$

The obtained data allows us to find the jump activation energy, its oscillation frequency at which the jumps through potential barrier are possible. This frequency is easily found by the way of lgf_{\max} dependence construction in function $1/T$ for TlInTe_2 (fig.2).

The line extrapolation to $1/T \rightarrow 0$ defines the oscillation frequency at which the particle overcomes the potential barrier and gets in frequency region $\nu = 7 \cdot 10^{12}$ Hz (D=0) and $\nu = 10^{11}$ Hz (50Mrad), that corresponds to further part of IR spectrum which gets in frequency region of phonon modes of oscillation spectrum of this crystal.

The line inclination gives the one act energy of charge transfer through the barrier correspondingly to $W^a = 0.5\text{eV}$ (D=0) and $W^a = 0.37\text{eV}$ (D=50Mrad). The given frequency for electronic processes is low.

The TlInTe_2 compound structure can be presented as the one from two subsystems: hard subsystem in the form of negatively charged chains (InTe_2), lying in the plane (001) and more mobile system of thallium ions [8]. Earlier, we mentioned [5] that from crystallographic point of view, the TlInTe_2 structure in most degree fosters to cation mobility Tl^+ .

The temperature dependence lgf_{\max} , at line extrapolation $1/T \rightarrow 0$, gets in oscillation region of low-frequency phonons in phonon spectrum of TlInTe_2 crystal [10] (triple compounds TlGaTe_2 and TlInTe_2 belong to class of TlSe chain semiconductors [1]).

The symmetry of these phonons are A_{2u} and E_u [10], they are observed in spectrum terahertz region and correspond to Tl^{1+} heavy atom oscillations.

Thus, especially thermal oscillations of thallium subsystem, phonons with symmetry A_{2u} and E_u where atomic oscillations Tl^{1+} are presented, lead to the fact that energy of these oscillations is higher than potential barrier after which thallium subsystem melts and crystal transits

into superior state. The investigations of oscillation spectrum of TlGaTe_2 crystal in terahertz region [4] reveal the oscillation which have frequency lower than most low-frequency phonon mode of A_{2u} symmetry at E//C measurements. This oscillation is related to chain libration oscillations ($\text{In}^{3+}\text{Te}^{2-}_2$) at system transition to superior state as especially at this temperature the sublattice Tl^+ begins to melt, the bond between chains and Tl^+ weakens, that is the reason of chain libration oscillations. It is necessary to note that low-frequency oscillations are observed in E//C geometry.

The ion disordering in the dependence on TlInTe_2 crystal temperature is above mentioned. Besides, the disordering degree can change under the influence of γ -radiation in general case. It is known that γ -irradiation of crystals leads to formation of radiation defects in the form of vacancies, intermodal atoms and also defect complexes of different types interacting between each other and chemical impurities.

The temperature dependencies of electric conduction $\sigma(T)$ of initial samples and TlInTe_2 crystals irradiated by γ -quanta are given on fig.3. As it is seen from the figure 3 the conduction increase is observed with increase of radiation dose up to 50Mrad. The temperature dependencies in coordinates $\ln(\sigma T)$ on $1000/T$ are given on insertion to fig.3. As it is seen, the experimental points are well situated on line in the correspondence with equation [12,13] for ion conduction case:

$$\sigma T = \sigma_0 \exp(-E^a/kT) \quad (3)$$

where E^a is conduction activation energy, k is Boltzmann constant. Such character of electric conduction shows on dominating character of ion conduction above the critic temperature [12,13].

The activation energy $E^a = 0.18\text{eV}$ (D=0) and $E^a = 0.24\text{eV}$ (D=50Mr) are defined.

It is shown that electric conduction at dose $D=50\text{Mrad}$ exceeds in 3 times the initial value in TlInTe_2 crystal.

As it is known in [6] the exponential increase of dielectric constant ε which can achieve enough big values at high temperatures is also observed in superior semiconductors at temperature increase besides exponential electric conduction increase.

The temperature dependencies of dielectric constants $\varepsilon(T)$ of initial samples and irradiated crystals TlInTe_2 are given on fig.4.

As it is seen from figure 4 at irradiation dose 50Mrad the dielectric constant increases (in comparison with initial value).

The defects of ionization type (charges defects) play the dominating role in these processes which appear as a result of irradiation by γ -quanta, i.e. the radiation-stimulated healing of structural defects leading to increase of crystal dielectric constant. The further increase of irradiation dose (at 100Mrad) leads to decrease of dielectric constant that is probably caused to increase of crystal structure imperfection under the influence of γ -quanta. The dose power 50Mrad is the critic one at which the dielectric constant of TlInTe_2 increases. At increase of γ -radiation dose the radiation defect quantity increasing leads to mobility decrease and therefore to

decrease of dielectric constant. As it is seen from the insertion to figure 4 the experimental points $\varepsilon(T)$ in logarithmical scale are well situated on direct line [12,13]:

$$\varepsilon(T) = \varepsilon_0 \exp(-E^a/kT) \quad (4)$$

The calculated activation energies by formula (4) are equal ones for initial samples TlInTe₂ $E^a = 0.16\text{eV}$ and $E^a = 0.23\text{eV}$ for ones irradiated by doze in 50Mrad .

The obtained data allows us to find the jump activation energy, its oscillation frequency at which the jump through potential barrier is possible. It is shown that TlInTe₂ crystal dielectric constant at doze D=50Mrad exceeds the initial value in 6 times. The investigations of doze dependences of TlInTe₂ crystal dielectric constant show on appear possibility (at defined value of critic doze) of jump disordering of Tl⁺ ion sublattice which is accompanied by jump change of dielectric constant.

Let's note that described effect by induced by field of jump disordering gives the possibility to realize the superior crystal state TlInTe₂ at crystal radiation by γ - quanta that opens the interesting possibilities of its practice use.

CONCLUSION

Thus, the obtained data allows us to find the jump activation energy, its frequency oscillation at which jump

through potential barrier is possible. This frequency is defined by construction way of $\lg f_{\max}$ dependence in function $1/T$ for TlInTe₂.

The obtained frequency oscillations is equal to $\nu = 7 \cdot 10^{12}$ Hz (D=0) and $\nu = 10^{11}$ Hz (D=50Mrad) that corresponds to terahertz region of electromagnetic spectrum and covers the region of low-frequency oscillation spectrum of TlGaTe₂ crystal (structural analogue of TlInTe₂ crystal).

The supposition that sublattice Tl⁺ begins to melt at system transition to superior state, the bond between chains and Tl⁺ weakens and the libration oscillation chains are possible (Ga³⁺Te²⁻₂). Such oscillations are observed in works [4,10] in experiment geometry E//C and are connected with libration oscillation chains (Ga³⁺Te²⁻₂).

It is shown that the maximal value of dielectric dissipation value shifts to more high temperatures in TlInTe₂ crystal with the increase of irradiation doze. It is established that in TlInTe₂ crystal the dielectric constant value at doze D=50Mrad in 6 times and electric conduction in 3 times exceeds the initial value.

Let's note that the described effect gives the possibility to realize the superior state in TlInTe₂ crystal at irradiation by γ -quanta.

This opens the wide possibilities of practical use of TlInTe₂ crystal superior state.

-
- [1]. V.D. Muller, G. Eulenberger, H. Hahn. Uber ternare Thalliumchalkogenide mit Thallium selenidstruktur // Z. Anorg. Allgem. Chem., 1973, № 398, p.207
- [2]. R.M. Sardarli, O.A. Samedov, A.P. Abdullaev, F.T. Salmanov. FTP, 2011, t.53, v.8, str.1488-1492. (In Russian).
- [3]. R.M. Sardarli, O.A. Samedov, A.P. Abdullaev, E.K. Quseynov, E.M. Qodjaev, F.T. Salmanov. FTP, 2011, t.45, v.8, str.1009-1013. (In Russian).
- [4]. P.M. Sardarly, O.A. Samedov, A.P. Abdullaev, F.T. Salmanov, A. Urbanovic, F. Garet, J-L. Coutaz. Superionic Conductivity in One-Dimensional Nanofibrous TlGaTe₂ Crystals. Jpn. J. Appl. Phys., 2011, 50, 05FC09-1-2.
- [5]. R.M. Sardarli, O.A. Samedov, A.P. Abdullaev, F.T. Salmanov, O.Z. Alekperov, E.K. Quseynov, N.A. Alieva. FTP. 2011, t.45, v.11, str.1441-1445. (In Russian).
- [6]. R.M. Sardarli, O.A. Samedov, A.P. Abdullaev, E.K. Quseynov, F.T. Salmanov, Q.R. Safarova. FTP, 2010, t.44, v.5, str.610-614. (In Russian).
- [7]. R.M. Sardarli, O.A. Samedov, A.P. Abdullaev, E.K. Quseynov, F.T. Salmanov, N.A. Alieva, R.Sh. Aqayeva. FTP, 2013, t. 47, v. 5. s.696-701. (In Russian).
- [8]. P.M. Sardarly, O.A. Samedov, A. Sardarli, N. Aliyeva, R.Sh. Aqayeva, T. Musazade. Superionic Conductivity and Specific Effects Induced by γ -Radiation in Nanofibrous TlGaTe₂ Crystals. International Journal of Theoretical and Applied Nanotechnology, vol.1. Issue 1, 2012, pp.20-28
- [9]. A. Lidyad. Ionnaya provodimost kristallov. Izd-vo IL, M.: 1962, 222s. (In Russian).
- [10]. S.Yu. Stefanovich, L.A. Ivanova, A.V. Astafyev. Ionnaya I superionnaya provodimost v seqnetoelektrikax. M: NIITEXIM, 1989, 80 s. (In Russian).
- [11]. A.M. Panich and R.M. Sardarly: Physical properties of the low dimensional A³B⁶ and A³B³C⁶₂ compounds. (Nova Science Publishers. Inc. New York, 2010, p.287.
- [12]. L.S. Parfeneva, A.I. Shelix, A.I. Smirnov, A.V. Prokofyev, V. Assmus. FTP, 2004, t.46, v.6, str.998. (In Russian).
- [13]. L.S. Parfeneva, A.I. Shelix, A.I. Smirnov, A.V. Prokofyev, V. Assmus, X. Misirek, Ya. Muxa, A.Yejovskiy, I.Q. Vasilyeva. FTT, 2003, t.45, v.11, str.1991. (In Russian).

Received: 18.02.2013

THEORETICAL CONFORMATIONAL ANALYSIS OF PIPERAZINE-2,3,5,6-TETRAONE

METİN BİLGE¹, YENAL GÖKPEK¹, MAHİR TURSUN²,
NESRİN EMİR¹ AND CEMAL PARLAK²

¹ Ege University, Sciences Faculty, Department of Physics, 35100, İzmir, Turkey

² Dumlupınar University, Faculty of Arts and Sciences, Department of Physics, 43100, Kütahya, Turkey

* E-mail: cparlak@dpu.edu.tr, Tel.: +90 (274) 265 20 51 / 3116, Fax: +90 (274) 265 20 56

Theoretical conformational analysis of piperazine-2,3,5,6-tetraone (pp2356to) has been performed in terms of the Becke-3-Lee-Yang-Parr (B3LYP) density functional theory (DFT) methods with 6-31++G(d) basis set. Calculations are employed in gas and solution phases. Solvent effects are investigated using benzene and methanol. Angular distribution of the probability density of populations of its conformers was determined by analysis of the potential energy surface (PES). pp2356to (C₄H₂N₂O₄) molecule is planar and located around an inversion center and, the four O atoms are in the 2,3,5,6-positions of the piperazine ring.

PACS: 31.15. E, 31.70.Dk, 33.15.Hp

Keywords: Piperazine-2,3,5,6-tetraone, Molecular structure, DFT, B3LYP.

1. INTRODUCTION

The synthesis and antitumor activity of some tetraone compounds have been widely studied [1-2]. Most tetraone compounds were found from a naturally occurring alkaloid in a variety of leguminous plant and tree species, including broom, lupine, gorse, and laburnum [3]. On the other hand, it has been known that many piperazine derivatives are of great interest in pharmacy and notable successful drugs [4-5]. pp2356to is both tetraone and piperazine derivatives and today one can easily reach many papers published where pp2356to as piperazine or tetraone derivatives. It has been also used in synthesis of some new biologically-active coumarin derivatives [6].

There is no any information present in literature about its spectroscopic properties except for some crystal data [7]. A detailed quantum chemical study together with solvent effect will aid in determining the molecular structure of pp2356to and in clarifying the obtained experimental data for this molecule. Furthermore, the presented data may be helpful in context of the further studies of pp2356to. In this work, we have theoretically performed the conformations of pp2356to and investigated the geometric parameters (bond lengths, bond-dihedral angles) of its most stable form in solution and gas phase using B3LYP/6-31++G(d) level. Furthermore, the thermodynamics functions, the highest occupied and lowest unoccupied molecular orbitals (HOMO and LUMO) of the title molecule have been predicted.

2. CALCULATION

All the calculations were performed by using Gaussian 09 program [8] on a personal computer and GaussView program [9] was used for visualization of the structure. For the theoretical conformational analysis, it was first investigated the internal rotation in pp2356to about O8-C3-N4-H12 and O10-C6-N1-H11 (Figure 1) dihedral angles scanning from 0 to 360 degrees in 10 degrees increments, which was calculated in the gas phase at B3LYP level of theory using 6-31++G(d) basis set. Figure 2 shows PES graphics for the title molecule. Scan

process has conducted for 361 different conformations of pp2356to and it has been found that pp2356to is the most stable in conformer 181 (Figure 2c). Analysis of PES allowed us to determine the conformational composition of pp2356to with a high accuracy and showed that pp2356to exists as planar which are seen from Figure 1.

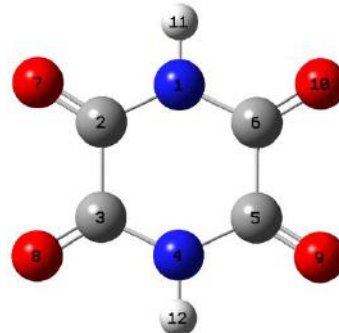


Fig 1. Optimized structure and numbering of pp2356to.

After the scan process, the conformer in the step 181 of pp2356to were optimized by B3LYP method with the basis set 6-31++G(d) in the gas phase, methanol and benzene. The polarizable continuum model, which is the default in Gaussian 09, was used for the geometries and free energies. The absence of imaginary frequencies also confirmed that the optimized structure is a local minimum.

3. RESULTS AND DISCUSSION

The results of the calculations on the molecular conformations and geometrical parameters of pp2356to are discussed first. A brief discussion of the HOMO and LUMO of the title molecule is then presented. Regarding the calculated free energies, 344 of 361 forms relative to the most stable conformer 181 could be neglected for the calculation of equilibrium constant since their energy differences are larger than 2 kcal/mol [4, 10-12]. For B3LYP method with the 6-31++G(d) basis set, form 181 is more stable than the other 16 conformers (143, 144, 160, 161, 162, 163, 179, 180, 182, 183, 199, 200, 201, 202, 218 and 219). Consequently, pp2356to in the gas phase prefers conformer 181 with approximate preference

THEORETICAL CONFORMATIONAL ANALYSIS OF PIPERAZINE-2,3,5,6-TETRAONE

of 93 %. The complete set of conformations investigated is available from the authors as supplementary material.

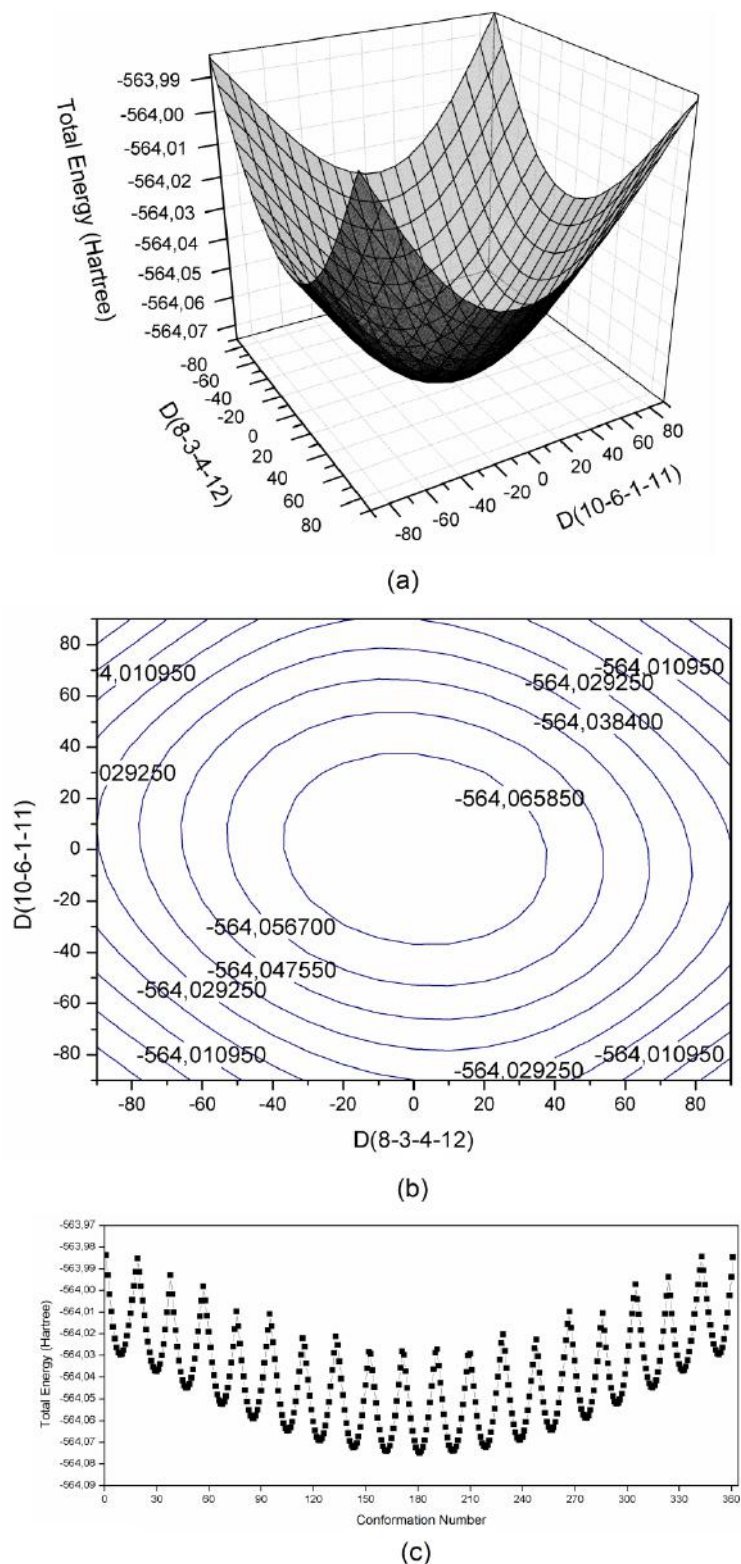


Fig 2. PES (a), contour (b) and conformation scan (c) graphics of pp2356to in the gas phase.

Gibbs free energy and several thermodynamics parameters such as capacity, zero point energy, entropy etc., calculated by B3LYP/6-31++G(d) method are presented in Table 1. Gibbs free energy is expected to be more stable in solution than the corresponding free energy in the gas phase. This situation is clearly observed in

Table 1. The variations in the zero point vibrational energy, vibrational energy, entropy, thermal total energy and heat capacity seem to be insignificant. The total energy and change in total entropy of pp2356to are at room temperature.

Table 1. Thermodynamic parameters for the most stable of pp2356to.

B3LYP-631++G(d)	Gas	Benzene	Methanol
ΔG (Hartree)	-564.036349	-564.046297	-564.057846
Molar Volume (cm ³ /mol)	74.277	-	-
Recommend (a_0)	3.9	-	-
Thermal Total Energy (kcal/mol)	50.193	50.125	50.127
Heat Capacity (kcal/mol.K)	28.676	28.715	28.59
Entropy (kcal/mol.K)	89.208	90.942	90.117
Vibrational Energy (kcal/mol)	48.416	48.347	48.349
Zero Point Vibrational Energy (kcal/mol)	45.21485	45.09219	45.15351
Rotational constant (GHz)			
a	2.30003	2.30723	2.31655
b	1.23864	1.24105	1.24434
c	0.80508	0.80699	0.80951

The optimized geometric parameters (bond lengths, bond and dihedral angles) calculated by B3LYP/6-31++G(d) are listed in Table 2 along with their experimental data. Generally, it is expected that the bond distances calculated by electron correlated methods are longer than the experimental distance. This situation is clearly observed in Table 2 as expected, especially where hydrogen is present. Overall, the calculated bond lengths are in good agreement with experimental results. The mean absolute deviations (MAD) of bond lengths from experiment for gas phase, benzene and methanol are 0.040, 0.039 and 0.038 Å, respectively. Similarly, the correlation values of bond lengths between the experimental and theoretical data are found to be 0.9460 for gas phase, 0.9483 for benzene and 0.9511 for methanol, respectively. The biggest difference between the experimental and calculated bond distances is 0.159, 0.160, 0.160 Å. These differences for all calculations belong to N-H bond distance. The observed differences in NH bond distances are not due to the theoretical

shortcomings since experimental results are also subject to variations owing to insufficient data to calculate the equilibrium structure and which are sometimes averaged over zero point vibrational motion.

In X-ray structure the error in the position of the hydrogen atoms is such that their bonding parameters greatly vary compared to the non-hydrogen atoms. Intra- or intermolecular hydrogen bonding is also an important factor in the crystalline state of compound which usually leads to shortening of the NH bond.

As it can be seen from Table 2, some differences are observed in the calculated C3-N4-C5, C2-C3-O8 and C6-C5-O9 bond angles compared to experimental values. The calculated values for these angles are about 2° larger than the experimental value. All the other bond angles are reasonably close to the experimental data. The MAD values of calculated bond angles from experiment for gas phase, benzene and methanol are 1.66, 1.43 and 1.07°, respectively.

Table 2. Optimized geometric parameters of pp2356to.

Bond Lengths (Angstroms)	B3LYP 6-31++G(d)			
	Exp.	Gas	Benzene	Methanol
C5-O9	1.202	1.208	1.210	1.212
C3-O8	1.210	1.208	1.210	1.212
C3-N4	1.360	1.392	1.388	1.383
N4-C5	1.368	1.392	1.388	1.383
N4-H12	0.860	1.019	1.020	1.020
C2-C3	1.526	1.544	1.544	1.544
Bond Angles (Deg)				
C3-N4-C5	125.31	128.15	127.74	127.09
C3-N4-H12	117.30	115.93	116.13	116.46
C5-N4-H12	117.30	115.92	116.13	116.46
N4-C3-O8	123.60	122.52	122.63	122.77
C2-C3-O8	119.10	121.56	121.24	120.77
C2-C3-N4	117.28	115.93	116.13	116.46
N4-C5-O9	123.30	122.52	122.63	122.77
C6-C5-O9	119.30	121.56	121.24	120.77
N4-C5-C6	117.35	115.92	116.13	116.46
Dihedral Angles (Deg)				
O8-C3-N4-H12	-	0.04	0.25	0.08
H11-N1-C6-O10	-	-0.02	0.14	0.10

The HOMO and LUMO are the main orbitals taking part in chemical stability. The transitions can be described from HOMO to LUMO. The HOMO and LUMO are located over the whole molecule due to its symmetric

structure. The atomic compositions of frontier molecular orbital and their orbital energies of pp2356to in the gas phase are shown in Figure 3.

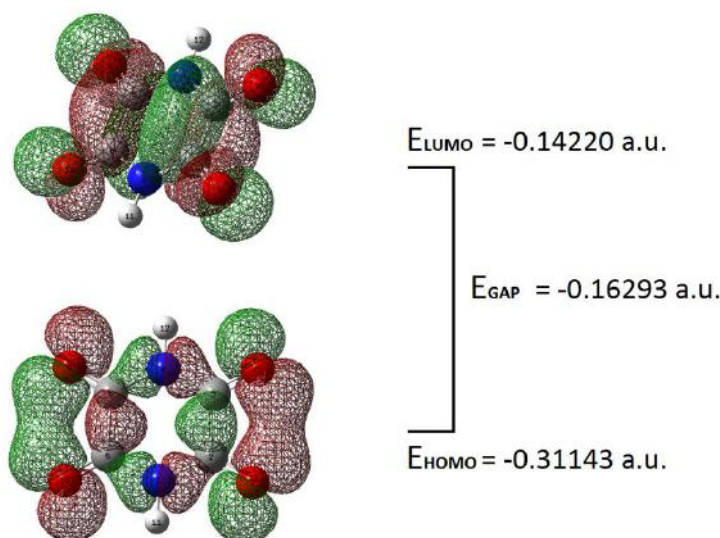


Fig 3. Atomic orbital compositions of the frontier molecular orbital for pp2356to.

4. CONCLUSION

According to the completed theoretical conformational analysis of pp2356to, following results can be summarized:

1. Results of energy calculations for gas phase indicate that form 181 from the 361 different conformers is the most stable conformer of pp2356to. Planar pp2356to is located around an inversion center and the O atoms are in the 2,3,5,6-positions of the piperazine. Furthermore, the conformational energy barrier is independent of the solvent.

2. Some changes are found in the geometric parameters when pp2356to in solvated. Due to dielectric medium, Gibbs free energy is more stable in solution than the corresponding energy in the gas phase.

3. Any differences observed between the experimental and calculated values could be due to the fact that the calculations have been performed for single molecule in the gas and solvations state contrary to the experimental values in the solid phase have been recorded in the presence of intermolecular interactions.

-
- [1] G.Z. Jin, Y. Kim, J.H. Chung, D.E. Sok, B.Z. Ahn, "Anthracene-1,4,9,10-tetraone derivatives: synthesis and antitumor activity", Arch. Pharm. (Weinheim), 331 (1998) 380–384.
- [2] M.A. Sanner, C. Weigelt, M. Stansberry, K. Killeen, W.F. Michne, D.W. Kessler, R.K. Kullnig, "New analogs of cyclo(Prn-Prn):synthesis of unsymmetric octahydro-1H,5H-dipyrrolo[1,2-a:1'2'-d]pyrazine-5,10-diones", J. Org. Chem. 57 (1992) 5264–5268.
- [3] N.R. Norcross, J.P. Melbardis, M.F. Solera, M.A. Sephton, C. Kilner, L.N. Zakharov, P.C. Astles, S.L. Warriner, P.R. Blakemore, "Total synthesis of (±)- α -Isosparteine, (±)- β -Isosparteine, and (±)-Sparteine from a common tetraoxobispidine intermediate", J. Org. Chem. 73 (2008) 7939–7951.
- [4] Ö. Alver, C. Parlak, "Vibrational spectroscopic investigation and conformational analysis of 1-cyclohexylpiperazine", J. Mol. Struct., 975 (2010) 85-92.
- [5] Ö. Bağlayan, M.F. Kaya, C. Parlak, M. Şenyel, "DFT, FT-Raman and FT-IR investigations of 1-cyclobutylpiperazine", Spectrochimica Acta A, 90 (2012) 109-117.
- [6] A.M. El-Sayed, A.B.A.G. Ghattas, M.T. El-Wassimy, O.A. Abd Allah, "Synthesis of some new biologically-active coumarin derivatives", IL Farmaco 54 (1999) 56–63.
- [7] J.J. Jia, X.J. Meng, S.Z. Liang, S.H. Zhangb, Y.M. Jianga, "Piperazine-2,3,5,6-tetraone. Corrigendum", Acta Cryst. E 66 (2010) o3315.
- [8] M.J. Frisch, G.W. Trucks, H.B. Schlegel, G.E. Scuseria, M.A. Robb, J.R. Cheeseman, G. Scalmani, V. Barone, B. Mennucci, G.A. Petersson, H. Nakatsuji, M. Caricato, X. Li, H.P. Hratchian, A.F. Izmaylov, J. Bloino, G. Zheng, J.L. Sonnenberg, M. Hada, M. Ehara, K. Toyota, R. Fukuda, J. Hasegawa, M. Ishida, T. Nakajima, Y. Honda, O. Kitao, H. Nakai, T. Vreven, J.A. Montgomery, Jr., J.E. Peralta, F.

- Ogliaro, M. Bearpark, J.J. Heyd, E. Brothers, K.N. Kudin, V. N. Staroverov, R. Kobayashi, J. Normand, K. Raghavachari, A. Rendell, J.C. Burant, S.S. Iyengar, J. Tomasi, M. Cossi, N. Rega, J.M. Millam, M. Klene, J.E. Knox, J.B. Cross, V. Bakken, C. Adamo, J. Jaramillo, R. Gomperts, R.E. Stratmann, O. Yazyev, A.J. Austin, R. Cammi, C. Pomelli, J.W. Ochterski, R.L. Martin, K. Morokuma, V.G. Zakrzewski, G.A. Voth, P. Salvador, J.J. Dannenberg, S. Dapprich, A.D. Daniels, Ö. Farkas, J.B. Foresman, J.V. Ortiz, J. Cioslowski and D.J. Fox, Gaussian 09, Revision A.1, Gaussian Inc., Wallingford CT, 2009.
- [9] R.D. Dennington, T.A. Keith, J.M. Millam, GaussView 5.0.8, Gaussian Inc., 2008.
- [10] C. Parlak, "Theoretical and experimental vibrational spectroscopic study of 4-(1-Pyrrolidiny)piperidine", J. Mol. Struct. 966 (2010) 1-7.
- [11] Ö. Alver, C. Parlak, "Vibrational spectroscopic investigation and conformational analysis of 1-pentylamine: A comparative density functional study", Journal of Theoretical and Computational Chemistry, 9 (2010) 667-685.
- [12] Ö. Alver, C. Parlak, "DFT, FT-Raman, FT-IR, liquid and solid state NMR studies of 2,6-dimethoxyphenyl-boronic acid", Vibrational Spectroscopy, 54 (2010) 1-9.

Resevied:14.01.2013

**PHASE TRANSITIONS AND THEIR CO-EXISTENCE
IN THE TiGaSe₂ - TiCoS₂ SYSTEM**

**N.Z. GASANOV, MIR-HASAN YU. SEYIDOV, R.Z. SADYKHOV,
F.M. SEYIDOV, R.G. VELIYEV, YU.G. ASADOV, E.M. KERIMOVA,
A.A. ISAYEVA, K.M. HUSEYNOVA**

*Institute of Physics, Azerbaijan National Academy of Sciences, H. Javid ave. 33, Baku, Az-1143
E-mail: nazimgasanov55@gmail.com*

Investigation of dielectric properties of layered compound TiGaSe₂ showed that it is a ferroelectric ($T_c = 114$ K) with an intermediate incommensurate phase ($T_i = 117.2$ K). Magnetic researches of layered compound TiCoS₂ revealed that this compound is a ferrimagnet and the magnetic characteristics are $T_C = 112$ K, $T_C^P = 120$ K, $\mu_{\text{eff}} = 4.6\mu_B$. Using the method of DTA, areas of homogeneous and heterogeneous coexistence of ferroelectric and ferrimagnetic orderings in the system TiGaSe₂ - TiCoS₂ were defined.

Keywords: crystal growth; dielectric properties; ferroelectrics; ferrimagnets; magnetic properties

PACS: 61.44.Fw; 77.22.-d; 77.80.-e; 77.80.Bh.

1. INTRODUCTION

Magnetoelectric (ME) materials compose a main class of multiferroic materials in which an applied magnetic field leads to an electric polarization response or, conversely, an applied electric field results in a magnetization response [1,2,3]. Such materials can be applied in modern solid-state electronics and functionalized materials, including spintronics [4,5]. The fundamental physical and chemical properties of ME materials also look promising. Search and preparation of ME materials could help in designing new original materials with rather unusual magnetic and dielectric properties differing from the properties of the parent phases (ferro-, antiferro-, ferri – electricity /or - magnetism) and with the possibility to manipulate the magnetic properties through electric fields and vice versa.

Due to the structural restrictions, generally ferroelectricity is not compatible with ferromagnetism [4]. It is known that ferroelectricity appears only in a non – centrosymmetric structure in contrast to a magnetic ion preferring a centrosymmetric surrounding. Hence magnetoelectrics are very rare materials and until now only a few compounds have been reported to exhibit both ferroelectric and ferromagnetic properties within the same phase. The requirements for obtaining both ferroelectric and magnetic orders in the same material can be summarized as follows: 1) the presence of adequate structural building blocks, permitting ferroelectric - type ionic movements, i.e. off - centre displacement associated with spontaneous polarization in ferroelectrics, 2) magnetic - interaction pathways for the magnetic order, usually of the super - exchange type, and 3) symmetry conditions [5,6].

ME materials can be either single - phase or composites. There is a scarcity of homogenous single - phase bulk materials exhibiting ME behavior [2,3,4,5,6]. Recently, much attention has been paid to the creation of composites from heterostructural layers piezoelectric and magnetostrictive phases, which could be electromagnetically coupled via stress mediation [2,3,4,5,6]. However, structural noncompatibility and reactivity between the two materials and also the substrate, generates immense difficulties in growing heterostructures and achieving coupling between the two

coupled degrees of freedom based on local off - centered polar distortion and electron spin.

Hence the search for new chemical equilibrium homogenous bulk magnetoelectric compounds with a simple and a cost preparation technology is still relevant.

In the present work, the solid solutions of TiGaSe₂ - TiCoS₂ have been prepared with a view of obtaining co - existence of ferroelectric and ferromagnetic properties in the same compound under the same range of temperatures. We plan to combine ferroelectrics TiGaSe₂ with magnetic material TiCoS₂, creating solid solutions by partly substituting Co at the Ga site without disturbing the ferroelectric properties of TiGaSe₂.

The solid solutions TiGaSe₂ - TiCoS₂ could be a new class of ME materials with effective and simple preparation technology meeting all conditions for ME specified above. In connection with the above the dielectric properties of layered compound TiGaSe₂ and magnetic properties of layered compound TiCoS₂ were investigated. The molar relations in the system of TiGaSe₂ - TiCoS₂ were characterized by differential thermal analysis (DTA).

2. EXPERIMENTAL PART

TiGaSe₂ and TiCoS₂ compositions were synthesized in quartz ampoules evacuated to a residual pressure about 10^{-3} Pa at the temperature ~ 1150 K from binary compounds (Ti₂Se, Ga₂Se₃ and Ti₂S, Co₂S₃), weighted in a equimolecular relation. First these binary compounds were powdered. The synthesis was conducted by an inclined furnace method for 72 hours. The angle of the furnace was about 30 degrees. The reaction product was carefully powdered and the synthesis was repeated. Then, obtained alloys were brought into powder, pressed and subjected to homogenizing annealing in evacuated quartz ampoules at a temperature of 600 K for 480 hours.

X-ray diffraction analysis of TiGaSe₂ and TiCoS₂ samples, specially prepared after annealing, was performed at room temperature (~ 300 K) using DRON-3M diffractometer (CuK _{α} radiation, Ni filter, $\lambda=0.15418$ nm, 35 kV, 10 mA). The angular resolution of continuous scanning was $\sim 0.01^\circ$. The diffraction angles were determined by maximum intensity of diffraction reflections. In the experiments the error for reflection

angles did not exceed $\Delta\theta = \pm 0.02^\circ$. In the angular range $10^\circ \leq 2\theta \leq 70^\circ$, diffraction reflections were observed from TlGaSe₂ and TlCoS₂ samples, which are induced on the basis of syngonies with parameters of the crystalline

lattice (tables 1 and 2): monoclinic ($a=1.0771$ nm, $b=1.0769$ nm, $c=1.5638$ nm, $\beta=100^\circ 04'$, $z=16$, $\rho_x=6425$ kg/m³) and trigonal ($a=0.3726$ nm, $c=2.2510$ nm, $z=3$, $\rho_x=6026$ kg/m³), respectively.

Table 1.

X-ray diffraction analysis of TlGaSe₂.

№	I/I ₀	d _{exp.} (nm)	d _{calc.} (nm)	hkl
1	20	0.44102	0.44102	122
2	5	0.40277	0.40272	202
3	100	0.38430	0.38421	004
4	20	0.35575	0.35598	221
5	5	0.34005	0.34002	130
6	5	0.32514	0.32560	114
7	20	0.32054	0.32252	222
8	70	0.28992	0.28940	312
9	10	0.26749	0.26695	025
10	60	0.25947	0.25947	034
11	5	0.24001	0.24001	240
12	5	0.21190	0.21110	150
13	5	0.20271	0.20377	117
14	20	0.19311	0.19270	153
15	20	0.19143	0.19204	512
16	5	0.18241	0.18221	154
17	20	0.17096	0.17079	208
18	10	0.16199	0.16204	119

Table 2.

X-ray diffraction analysis of TlCoS₂.

№	I/I ₀	d _{exp.} (nm)	d _{calc.} (nm)	hkl
1	40	0.37532	0.37517	006
2	40	0.32282	0.32275	100
3	100	0.31035	0.31039	102
4	20	0.27992	0.27995	104
5	20	0.25013	0.25011	009
6	10	0.22508	0.22510	0010
7	10	0.17320	0.17315	0013

It should be noted that our X-ray data for sample TlGaSe₂ is in good agreement with the crystal structure studies performed in [7]. Unit cell of TlGaSe₂ crystal contains two-dimensional periodic layer of groups of polyhedrons Ga₄Se₁₀ [7], each of which is a combination of four elementary tetrahedrons GaSe₄, located by the diamond rule around a central empty octahedron Se₆. Between polyhedral complexes of Ga₄Se₁₀ from different layers the weak van der Waals bond dominates, and chemical bond within the layer has an ion-covalent character. Therefore, during the separation of the TlGaSe₂ crystal, Ga₄Se₁₀ polyhedrons are preserved, i.e. crystal

unit cell of TlGaSe₂ has two-layer planar construction from the groups of Ga₄Se₁₀ polyhedrons and in spatial crystal structure of the layered compound TlGaSe₂, due to the strong anisotropy of the chemical bond energy between the atomic complexes, both a superstructure and polytype transformations are possible.

For investigation of the temperature dependence of dielectric permittivity $\epsilon(T)$ of the layered compound TlGaSe₂, samples cut out from the single-crystal ingot of this compound were used. The single-crystal ingot of TlGaSe₂ was grown by Bridgman-Stockbarger method; in this case the rate of the movement of crystallization front

was 1 mm/h. The plates of TlGaSe₂ had ~2 mm thickness and ~20 mm² surface area and were cut parallel to [010] axis. For $\epsilon(T)$ measurements, two gold electrodes were attached by the vacuum deposition method along the [010] axis. The distance between the electrodes was ~ 2 mm. A thin copper wire was attached to the electrodes by high - purity silver paste drop.

The sample was placed inside a liquid - nitrogen cryostat equipped with a temperature stabilization system with an accuracy of ± 0.05 K.

The permittivity was measured by the automatic digital precision LCR - meters at a frequency of 1 kHz during heating with the linear rate of ~ 1 K/min. The relative error in the determination of the permittivity was less than ~ 0.2%. The temperature of the sample was measured with a copper – constantan thermocouple. The thermocouple junction was located in the vicinity of the sample surface. Temperature of the sample was controlled by a PID digital temperature controller within ± 0.01 K.

The specific magnetization (σ_{sp}) of the layered compound TiCoS₂ was measured with a Domenicalli pendulum magnetometer and paramagnetic susceptibility (χ) - using Faraday method on magnetoelectric scales. Samples for the measurements had cylindrical shape with dimensions of $h \approx 3$ mm and $d \approx 2.5$ mm.

Research was carried out in the temperature range 77-300 K in the quasi static regime.

Molar relations in the system TlGaSe₂ - TiCoS₂ were characterized by the DTA method, which was carried out on the low frequency thermograph recorder NTR-64, which allowed measurement of the temperature of phase transformation with accuracy of ± 5 K. Heating rate was about 2 - 4 K/min. Temperature was controlled by Pt-Pt/Rh - thermocouple, graded according to fiducial elements in the interval of 430-1560 K.

3. RESULTS AND DISCUSSION

The temperature dependence of dielectric permittivity $\epsilon(T)$ of the layered compound TlGaSe₂ measured at the atmospheric pressure is presented in fig.1.

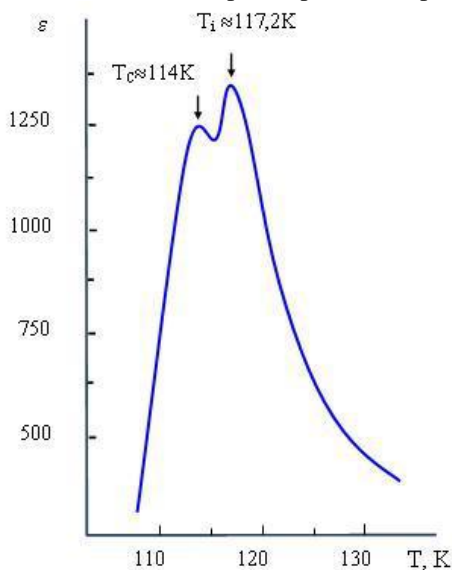


Fig.1. The temperature dependence of the dielectric permittivity of TlGaSe₂.

As it is seen from the figure, the temperature dependence curve $\epsilon(T)$ of TlGaSe₂ contains maxima in connection to the phase transition (PT) points in the incommensurate phase at $T_i = 117.2$ K and commensurate ferroelectric phase at $T_c = 114$ K.

The temperature curves $\epsilon(T)$ of compound TlGaSe₂ in the paraelectric and ferroelectric phases are well approximated by Curie-Weiss law with the value of Curie constant of about 10^3 K. It is noted, that temperature state of the anomalies on the curve $\epsilon(T)$, and the value of Curie constant TlGaSe₂ are also well agreed with the results obtained by others [8-12].

Low symmetry of crystallographic structure of TlMeX₂ type magnets (where Me is 3d metal; X is S, Se or Te) [13-18] predefines dependence of their magnetic properties from basic crystallographic directions, in some cases (structure has plain or chain constructions) – up to occurrence of low-dimensional effect, when spin system (magnetic structure) of the magnet in paramagnetic area, in certain temperature interval, is in quasi-two-dimensional or quasi-one-dimensional magnetic ordering (Ising – Heisenberg model) [19].

According to this model, behavior of low-dimensional spin systems in the area of high temperatures (paramagnetic area), in the vicinity of three-dimensional magnetic phase transition and in the area of low temperatures has specific peculiarities, which sharply differs it from behavior of three-dimensional spin systems.

For example, temperature dependence of magnetic susceptibility of low-dimensional antiferromagnet in paramagnetic area of temperatures with $T \gg T_N$ (T_N – Neel point, which characterizes the long-range magnetic ordering), is characterized by the presence of wide maximum, which is associated with a strong short-range magnetic order [20]. Also on the temperature dependence of thermal capacity of low-dimensional magnets, anomaly with evident deviation from λ -type is observed [21-23]. This experimental fact predetermines T_c^p value much greater in magnitude than T_c (specific feature in the vicinity of three-dimensional magnetic PT).

For three-dimensional magnetics difference between the temperatures that characterize the long-range and short-range magnetic order is small and amounts to 3-5% of the temperature, which characterizes short-range magnetic order [19].

Figure 2 shows the magnetic-field dependences of specific magnetization $\sigma_{sp}(H)$ of TiCoS₂, at 77 K this curve is typical for substances, which have the spontaneous magnetization.

The increase of paraprocess in $\sigma_{sp}(H)$ dependence at the temperatures of 90 and 100 K indicates the approach to the temperature of magnetic PT in TiCoS₂.

This can be seen from figure 3, where the temperature dependence of specific magnetization of TiCoS₂, measured in a magnetic field $8 \cdot 10^5$ A/m, is presented. Also in this figure the temperature dependence of spontaneous magnetization σ_s is shown.

The Curie temperature T_c was determined by the method of thermodynamic coefficients [24] and for TiCoS₂ is 112 K. At 77 K the magnetic moment of saturation is $0.36 \mu_B$ for TiCoS₂.

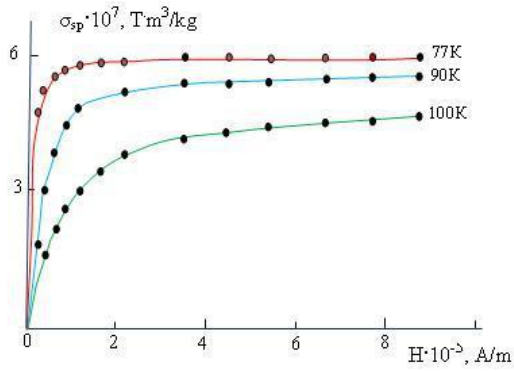


Fig.2. The field dependence of specific magnetization of TiCoS₂.

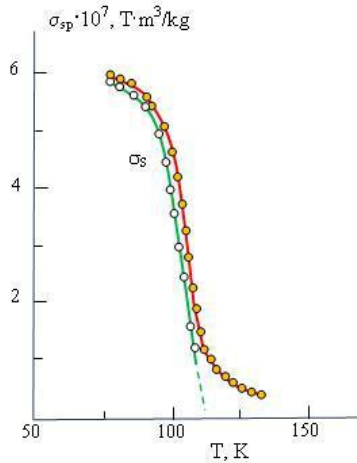


Fig.3. The temperature dependence of specific magnetization of TiCoS₂.

The temperature dependence of the inverse paramagnetic susceptibility $\chi^{-1}(T)$ of the TiCoS₂ compound (figure 4) is characteristic of ferrimagnetic material. The paramagnetic Curie temperature T_C^p , determined by approximation of $\chi^{-1}(T)$ to the temperature axis, is equal to 120 K for TiCoS₂. The effective magnetic moment μ_{eff} was calculated from the dependence of $\chi^{-1}(T)$ and is equal to $4.6\mu_B$ for TiCoS₂. The theoretical value, which is calculated, taking into account the value of spin magnetic moment of the Co³⁺ ion, is $4.9\mu_B$. The proximity of μ_{eff} to the theoretical value for layered compound TiCoS₂ allows us to draw a conclusion that in TiCoS₂ below $T_C = 112$ K isotropic - ferrimagnetic ordering is established.

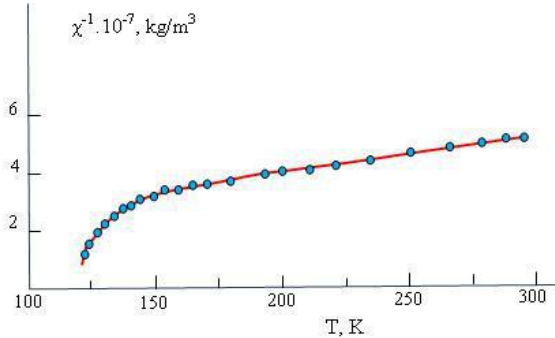


Fig.4. The temperature dependence of the reverse magnetic susceptibility of TiCoS₂.

In order to solve the physical task, presented at the beginning of the article, it is necessary to determine the area of the homogenous and heterogeneous co-existence of the ferroelectric TiGaSe₂ with ferrimagnet TiCoS₂.

State diagram of TiGaSe₂-TiCoS₂ system constructed from the results of DTA is presented in figure 5. This system is eutectic type quasi-binary with solid solutions on the base of TiGaSe₂ (homogenous area of the co-existence of ferroelectric and ferrimagnetic orderings), reaching 6 mol% TiCoS₂ at temperature of 300 K. The eutectic is formed at components ratio of 1:1. The eutectic melts at temperature of 630 K and has the composition (TiGaSe₂)_{0.5}(TiCoS₂)_{0.5}, i.e. in this eutectic alloy ferroelectric and ferrimagnetic orderings heterogeneously (compositionally) co-exist. The solid solutions and eutectic alloys in TiGaSe₂ - TiCoS₂ system can be used as basic materials for various functional recorders.

In the publication [25], in order to obtain a composite magnetoelectric material, mirror surface of layered single crystal samples of ferroelectrics TlInS₂ and TiGaSe₂ was subjected to bombardment by ion beam of cobalt (Co³⁺) with energy of 40 keV and beam density of $1.0 \cdot 10^{17}$ ion·cm⁻². Implanted in this way by nanoparticles of cobalt, samples of layered ferroelectrics TlInS₂ and TiGaSe₂ were tested by the authors [25] for the coexistence of ferroelectric and ferromagnetic phase transitions, however the ferroelectric phase transition in them has not been detected, and implanted nanoparticles Co³⁺ behaved in this case as systems of ultrafine ferromagnetic particles in the state of superparamagnetism.

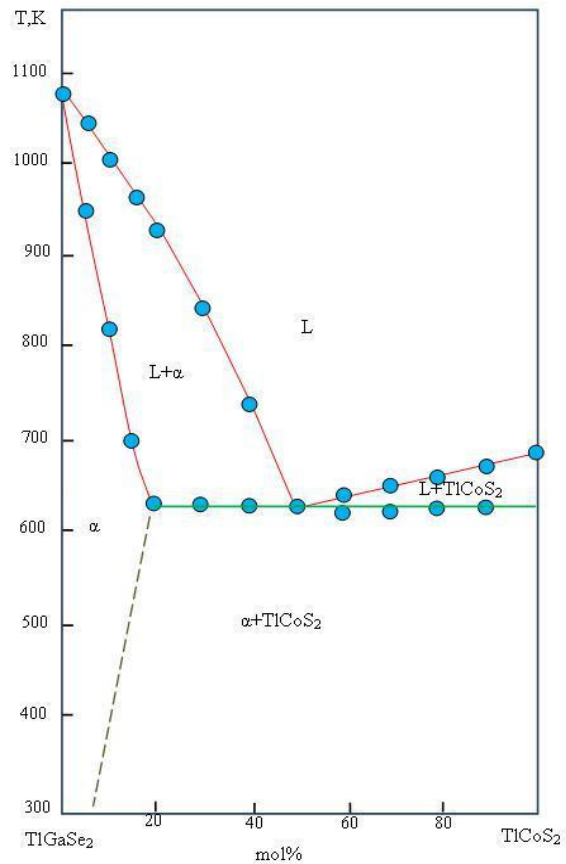


Fig.5. TiGaSe₂ - TiCoS₂ system state diagram.

4. CONCLUSION

Temperature dependence of the dielectric permittivity of the layered compound TlGaSe₂ has two anomalies that are associated with phase transitions in the incommensurate phase at $T_i = 117.2$ K, and the commensurate ferroelectric phase at $T_c = 114$ K. In the paraelectric and ferroelectric phases $\epsilon(T)$ of TlGaSe₂ follows the Curie-Weiss law with Curie constant of about

10^3 K. Magnetic studies of layered compound TlCoS₂ revealed that this compound is a ferrimagnet with magnetic characteristics found to be $T_C = 112$ K, $T_C^P = 120$ K, $\mu_{\text{eff}} = 4.6\mu_B$. By DTA method areas of homogeneous and heterogeneous coexistence of ferroelectric and ferrimagnetic orderings in the system TlGaSe₂ - TlCoS₂ were defined.

-
- [1] *N.A. Hill*. Why are there so few magnetic ferroelectrics?, *J. Phys. Chem. B*, 2000, v.104, pp.6694-6709.
- [2] *Ma Jing, Hu Jiamian, Li Zheng, Nan Ce-Wen*. Recent Progress in Multiferroic Magnetolectric Composites: from Bulk to Thin Films, *Adv. Mater.*, 2011, v.23, pp.1062–1087.
- [3] *M. Fiebig*. Revival of the magnetoelectric effect, *J. Phys. D: Appl. Phys.*, 2005, v.38, pp.R123-R152.
- [4] *L.W. Martin, S.P. Crane, Y-H. Chu, M.B. Holcomb, M. Gajek, M. Huijben, C-H. Yang, N. Balke, R. Ramesh*. Multiferroics and magnetoelectrics: thin films and nanostructures, *J. Phys.: Condens. Matter*, 2008, v.20, p.434220.
- [5] *Testino, L. Mitoseriu, V. Buscaglia, M.T. Buscaglia, I. Pallecchi, A.S. Albuquerque, V. Calzona, D. Marre, A.S. Siri, P. Nanni*. *J. of the European Ceramic Society*, 2006, v.26, pp.3031-3036.
- [6] *M.T. Buscaglia, L. Mitoseriu, V. Buscaglia, I. Pallecchi, M. Viviani, P. Nanni, A.S. Siri*. *J. of the European Ceramic Society*, 2006, v.26, pp.3027-3030.
- [7] *D. Müller, H. Hahn*. Zur Struktur des TlGaSe₂, *Z. Anorg. Allg. Chem.*, 1978, v.438, pp.258-272.
- [8] *K.R. Allakhverdiyev, N.D. Akhmed-zade, T.G. Mamedov, T.S. Mamedov, M.Yu. Seyidov*. Features of the behavior of TlInS₂ and TlGaSe₂ layered crystals near phase transitions in a static electric field, *Phys. Low Temper.*, 2000, v.26, pp.76-83.
- [9] *H. Hochheimer, E. Gmelin, W. Bauhofer*. *J. Phys. B: Condens. Matter*, 1988, v.73, pp.257-263.
- [10] *A.K. Abiyev, N.A. Bakhishov, A.E. Bakhishov, M.S. Gadzhiyev*. The behavior of hysteresis loops in the phase transition in TlGaSe₂, *Izv. VUZov, "Physics"*, 1989, N.12, pp.84-86.
- [11] *D.F. Mc.Morrow, R.A. Cowley, P.D. Hatton, J. Banys*. *J. Phys. Cond. Matter*, 1990, v.2, pp.3699-3712.
- [12] *R.M. Sardarly, O.A. Samedov, I.Sh. Sadykhov*. Ferroelectricity and Polytypizm in TlGaSe₂ Crystals, *Sol. Stat. Commun.*, 1991, v.77, pp.453-455.
- [13] *A. Kutoglu*. Synthese und Kristallstrukturen von TlFeS₂ und TlFeSe₂, *Z. Naturwissensch.*, 1974, v.B61, pp.125-126.
- [14] *K. Klepp, H. Boller*. Die Kristallstruktur von TlFeS₂ und TlFeSe₂, *Z. Monatssh. Chem.*, 1979, v.110, pp.1045-1047.
- [15] *M. Zabel, K. Range*. Ternare phazen im system eisen-tallium-schwefel, *Z. Naturforsch.*, 1979, v.B34, pp.1-6.
- [16] *M. Rosenberg, A. Knulle, H. Sabrowsky, C. Platte*. Magnetic properties and structure of some ternary chromium chalcogenides with thallium and silver, *J. Phys. Chem. Solids*, 1982, v.43, pp.87-95.
- [17] *G.I. Makovetskiy, E.I. Kasinskiy*. State diagram and crystal structure of alloys in TlFeS₂ - TlFeSe₂ system, *Inorgan. Mater.*, 1984, v.20, pp.1752-1753.
- [18] *R.G. Veliyev, R.Z. Sadykhov, Yu.G. Asadov, E.M. Kerimova, A.I. Jabbarov*. Magnetization, paramagnetic susceptibility and electrical conductivity of layered TIMnS₂ and TIMnSe₂ antiferromagnets, *Crystallography Reports*, 2008, v.53, pp.130-133.
- [19] *K.S. Aleksandrov, N.V. Fedoseyeva, I.P. Spevakova*. Magnetic phase transitions in galoid crystals, *Novosibirsk, Science*, 1983, pp.40-85.
- [20] *R.G. Veliyev*. About a magnetic phase transition in the strongly chained semiconductor compounds TlFeS₂, TlFeSe₂, *Semiconductors*, 2011, v.45, pp.158-161.
- [21] *M.A. Aldzhanov, N.G. Guseinov, G.D. Sultanov, M.D. Nadzhafzade*. Magnetic heat capacity and susceptibility of the pseudo-one-dimensional magnetic systems TlFeS₂ and TlFeSe₂, *Phys. Stat. Sol. (b)*, 1990, v.159, pp.K107-K110.
- [22] *M.A. Aldzhanov, A.A. Abdurragimov, S.G. Sultanova, M.D. Nadzhafzade*. Low temperature heat capacity of TlCrS₂, *Phys. Sol. Stat.*, 2007, v.49, pp.309-310.
- [23] *M. Aldzhanov, M. Nadzhafzade, Z. Seidov, M. Gasumov*. Heat capacity and magnetic susceptibility of TlCrSe₂, *Tr. J. Physics*, 1996, v.20, pp.1071-1073.
- [24] *K.P. Belov, A.N. Goryaga*. *Fiz. Met. Metalloved.*, 1956, v.2, pp.441-446.
- [25] *F. Mikailzade, A.G. Şale, S. Kazan, R.I. Khaibullin, N.I. Khalitov, V.I. Nuzhdin, T.G. Mammadov*. Magnetic properties of Co implanted TlInS₂ and TlGaSe₂ crystals, *Sol. Stat. Commun.*, 2012, v.152, pp.407-409.

INFLUENCE OF SMALL PARTICLES ON ELECTROHYDRODYNAMIC INSTABILITY IN THE NEMATIC LIQUID CRYSTAL

T.D. IBRAGIMOV^a, Ch.O. QAJAR^a, SH.YU. SAMEDOV^a, G.M. BAYRAMOV^b

^{a)} *Institute of Physics of Azerbaijan National Academy of Sciences.*

AZ1143, H.Javid Avenue, 33, Baku

^{b)} *Baku State University, AZ1148, Z. Khalilov street, 23, Baku, Azerbaijan*

Influence of silver and aluminum oxide particles on display of electrohydrodynamic instability (EHDI) in the nematic liquid crystalline (LC) mixture H-37 was investigated in the work. It was shown that the occurrence of silver particles in LC reduces the threshold voltage of the EHDI formation in a static field, and then it is more at low frequencies and less at high ones than in the pure H37. Meanwhile, the limiting frequency of the EHDI disappearance increases. While aluminum oxide particles reduce the threshold voltage of the EHDI occurrence at low frequencies on greater value than silver particles and they increase it at the high frequencies. A presence of particles changes rise and decay times in comparison with the pure LC. It is connected with an increase in viscosity and a reduction of elastic properties of LC and also overcoming the additional obstacles by ions.

Keywords: liquid crystal, electrohydrodynamic instability, silver, aluminum oxide, small particles.

PACS: 42.70.Df; 47.20.Cn; 47.32.Cd; 61.30.Gd.

1. INTRODUCTION

One of used electrooptical effects in liquid crystal (LC) is electrohydrodynamic instability (EHDI). It is electric-induced phenomenon that is caused by the flow of a liquid. The reason for the flow is electric conductivity. Purified nematic LC, as well as others organic dielectrics, have low intrinsic electric conductivity. But even at the most careful purifying there is some quantity of an ionic impurity in them, giving appreciable conductivity. Moreover, ions are born by means of electron injection from an electrode with the subsequent capture on neutral molecules of a substance. The flow may arise in any liquid independently on the anisotropic properties of substance [1]. The threshold for EHDI depends on many parameters such as the electric and visco-elastic properties of liquid, temperature and the applied field frequency. Due to the flow distortion of the director alignment, the instability is usually accompanied by characteristic optical pattern [2-6]. Among the instabilities in LC the most known are the Carr-Helfrich instability which is arises in a homogeneously oriented LC layer in a sandwich cell between transparent electrodes [7]. It is caused by a low-frequency electric field and occurs in the form of elongated vortices with their axis perpendicular to the original director alignment. The vortices cause a distortion of the director orientation, which is observed optically as a one-dimensional periodic pattern. They are called by Williams' domains. The reason for this instability is the space charge accumulated in the bulk due to the anisotropy of conductivity. It appears in thin cells (10-100 μm) and has a well-defined voltage threshold that is independent of the thickness. With voltage increasing the domain picture becomes complicated and then is greased, being replaced by a picture of intensive boiling which is accompanied by strong light scattering called by dynamic scattering. In the present work, we have studied influence of embedded particles on Carr-Helfrich instability in a standard cell with planar oriented nematic LC with negative dielectric anisotropy.

2. EXPERIMENTAL

The samples were pieces of chemically pure silver and aluminum oxide. After thoroughly grinding in an

agate mortar with a small addition of alcohol, the powder obtained was separated according to sedimentation time in a column with hexane according to the expression $t = 18h\eta/(\rho_1 - \rho_2) g d^2$, where h is the height of the column; η is the viscosity coefficient of the liquid; ρ_1 and ρ_2 are the densities of solid particles and hexane; g is the gravity acceleration; d is the transverse dimension of the particles.

The obtained fractions were dried under a vacuum of 10^{-2} Torr at $T = 50$ °C for a week. We used liquid crystalline mixture consisting of 4-methoxybenzylidene-4'-butylaniline (MBBA) and 4-ethoxybenzylidene-4'-butylaniline (EBBA) with molar ratio of 1:1 (H-37) as a matrix. Selection of the present mixture is also based on following facts: a dielectric anisotropy is negative and conductive along the director is more than one perpendicular to the director for this LC. It was the opportunity for the EHDI study in nematic LC since the occurrence of field effects was excluded and it was only observed in planar sample of LC with negative dielectric anisotropy [8].

The fractions of conductive silver particles with average sizes of 2.0 μm , 1.5 μm , 1.0 μm , 0.5 μm and less than 0.2 μm , and also dielectric aluminum oxide particles with sizes less than 0.1 μm have been chosen as embedded particles. Dispersion of specified particles in a liquid crystal was carried out by combined method. In the first stage the mechanical mixer with rotational frequency of 1000 rpm and in the second stage the ultrasonic vibrator with limiting frequency of 120kHz were used. Limiting concentration of dispersion for particles was approximately 0.5 %.

Identification of phase state of the composite under polarization microscope and investigation of its electrooptical properties were carried out in the electrooptical cell (Fig.1).

The latter had a sandwich structure and consisted of two plane-parallel glass plates whose inner surfaces were coated with thin transparent and conductive layer ITO (Indium-Tin-Oxide). Planar orientation of molecules was reached by coating of inner substrate surfaces with rubbed polyimide layers. For obtaining homeotropic orientation of LC molecules, we used the surfactants (soup solution or lecithin).

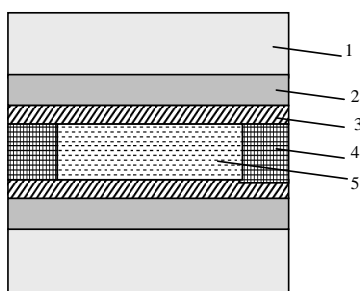


Fig.1. Structure of electrooptical cell with composite: 1- glass plate; 2- thin layer of In_2O_3 or SnO_2 ; 3 - orientate; 4- dielectric gasket; 5- composite.

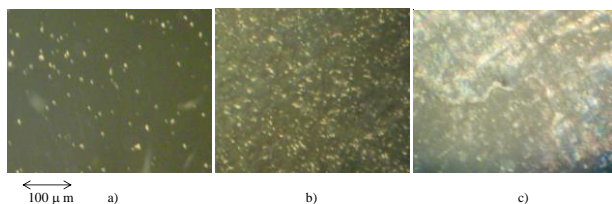


Fig.2. Pictures under polarization microscope: a) homeotropic texture of nematic LC H-37; b) homeotropic texture H-37+ Ag (0.2%); c) homeotropic texture of H-37+ Al_2O_3 (0.4%).

A study of electrooptical effects in composites has been carried out on the equipment assembled on the base of polarization microscope POLAM-111 (Fig.3)

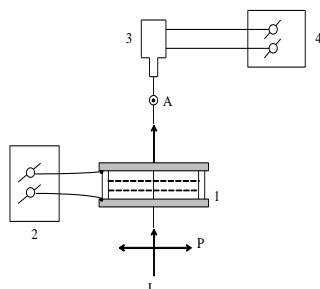


Fig.3. Block scheme of device for investigation of electrooptical properties of the cell with the composite: 1-cell; 2- voltage source; 3-photomultiplier; 4- oscillograph or recorder; P-polarizer; A- analyzer, L - light lamp.

Electro-optical cell with the composite was kept in the spatial heater in which the copper-constantan thermocouple was used for temperature measurements. The threshold voltage of EHDI displaying (Williams domains) was defined visually by observation under polarization microscope (Fig.4).

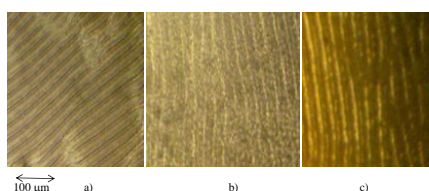


Fig.4. Williams domains observed in following compositions: a- pure H-37, b- H-37+ Ag (0.2%), c-H-37+ Al_2O_3 (0.2%).

The devices TEC-9 (direct voltage), G3-109 (sine voltage), and G6-15 (electrical impulses of spatial form) were the sources of electric field. The threshold voltage and contrast ratio of the electrooptical effect were determined by the dependence of light transmission on voltage (volt-contrast characteristic) applying the slowly changing (0.1 V/sec) saw-tooth voltage. In order to measure the switching times, the unipolar rectangular pulse was applied to the cell and the time dependence of light transmission was defined.

3. RESULTS AND DISCUSSION

Results of preliminary measurements have shown that a low concentration addition of silver and aluminum oxide particles in the liquid crystal practically does not influence on contrast characteristics of the EHDI effect.

Frequency dependence of threshold voltage of the Williams domain formation for both pure H 37 and with an addition of particles is shown in Fig.5. Indicated dependence is similar for all samples: with frequency increasing the threshold voltage increases and it aspires to infinity at some frequency, indicating on disappearance of the EHDI effect. One can note that a variation of particle sizes virtually does not influence on this dependence at low concentration of particles.

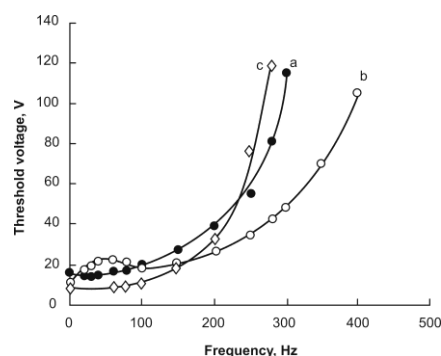


Fig.5. Frequency dependence of the threshold voltage of Williams domains: a - pure H-37, b - H-37+ Ag (0.2%), c - H-37+ Al_2O_3 (0.2%).

The occurrence of silver particles in LC reduces the threshold voltage of the EHDI formation in a static field; it is more at low frequencies and less at high ones than in the pure H37. Meanwhile, the limiting frequency of the EHDI disappearance increases. Aluminum oxide particles reduce the threshold voltage of the EHDI occurrence in a static field and at low frequencies on greater value than silver particles and they increase it at higher frequencies. At the same time, the limiting frequency is displaced towards small values.

Time characteristics of the EHDI effect are resulted in Fig. 6 and Fig. 7. Apparently, a rise time decreases with increasing of the applied voltage in all cases. An addition of particles into H-37 increases a rise time in the region of the large voltage. With voltage increasing a decay time of the EHDI effect increases at low voltages while it almost does not vary at high voltages. An addition of silver particles reduces a decay time while a presence of aluminum oxide particles slightly increases it.

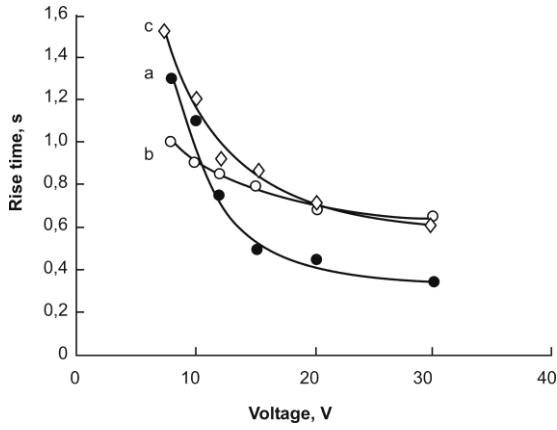


Fig.6. Dependence of rise time of EHD on static field voltage: a –pure H-37, b - H-37+ Ag (0.2%), c - H-37+ Al₂O₃ (0.2%).

The physical mechanism of the instabilities could be described as follows [9]. A homogeneously oriented nematic LC is stabilized by the elastic torque due to anchoring of LC molecules with a substrate surface. Dielectric torque because of both external and space charge fields is stabilizing for LC with negative dielectric anisotropy. Owing to a magnetic field, the arising torque also is stabilizing.

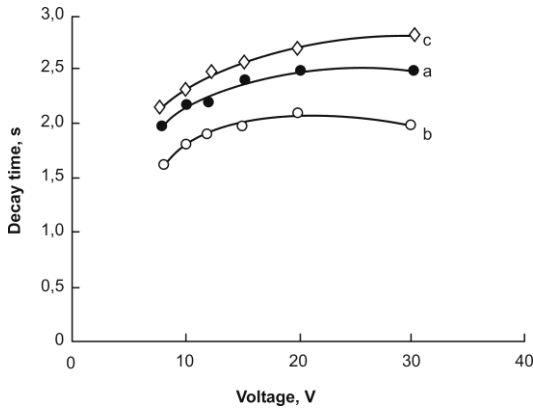


Fig.7. Dependence of decay time of EHD on static field voltage: a –pure H-37, b - H-37+ Ag (0.2%), c - H-37+ Al₂O₃ (0.2%).

The ions are charge carriers in the nematic phase, whose mobility along long molecular axis is greater than the mobility perpendicular to this direction. As a result, the electroconductivity is greater in one direction than in another. Therefore, nematic LC usually has positive anisotropy of electroconductivity. The space charge can be formed owing to this anisotropy because of ion division. The applied field acts on charges, causing occurrence of the substance flow in reciprocal directions. It creates the unstable torque induced by the electroconductivity and acting on molecules. The EHD effect arises if this torque exceeds all other torques. At low frequencies of an applied field, the instability mode is characterized by that a space charge oscillates with a field frequency. At the same time, so far as the threshold of the Williams domain occurrence is low, a reaction time of the director is sufficiently great. Thus, the threshold voltage sharply increases at approaching to the critical frequency

ω_c which is connected with a dielectric relaxation τ_c by the relationship [9]:

$$\omega_c = (\xi^2 - 1)^{1/2} / \tau_c$$

where $\xi^2 = \epsilon_{\parallel}^2 \eta_B (\epsilon_{\perp} / \epsilon_{\parallel} - \sigma_{\perp} / \sigma_{\parallel}) / \Delta \epsilon \epsilon_{\perp} \eta$ is called by Helfrich parameter; ϵ_{\parallel} and ϵ_{\perp} are components of dielectric permittivity, $\Delta \epsilon$ is dielectric anisotropy; σ_{\parallel} and σ_{\perp} are electroconductivities along and normal to the director, respectively.

The threshold voltage for static and low frequency field in the case of planar configuration of nematic LC with negative dielectric anisotropy is defined by the formula:

$$U_{th} = -4\pi^3 \epsilon_{\parallel} K_{33} / \Delta \epsilon \epsilon_{\perp} (\xi^2 - 1),$$

where K_{33} is the bend elastic constant and η_B is the corresponding viscosity for bend deformation; η is the effective viscosity. A rise time of the instability is defined by the expression:

$$\tau_r = \beta \eta_B d^2 / (U^2 - U_{th}^2),$$

While a decay time has the form:

$$\tau_d = \alpha \eta_B d^2 / \pi^2 K_{33},$$

where α and β are the coefficients depending on LC parameters; d is the cell thickness; U is the voltage of applied static field.

Though the ionic current follows an external field, a separation process of a space charge phase lags on the phase from a field with frequency increasing. It leads to reduction of force influence on a space charge from an external field. The torque corresponding to conductivity, decreases and it is required to raise an external voltage for instability achievement that is confirmed by the experiment (Fig. 5). Inclusion of particles in LC feebly alters dielectric permeability and conductivity properties of LC in a static field.

Probably, a change in threshold voltage is connected with other reasons. Aluminum oxide particles in LC induce development of instability at lower threshold because they are the turbulence centers in LC. At the same time, with increasing of the external field frequency nonconducting aluminum oxide particles prevent to a movement of ions and it is required greater voltage to maintain the instability. In connection with it, there is a sharper increase of threshold voltage with a frequency change. Conducting particles of silver at sufficiently low frequencies of an external field prevent a formation of a space charge because they play a role of traps for moving ions. Therefore, the threshold voltage increases at corresponding frequencies. With the further frequency increase of an external field, silver particles participate in liquid movement, increasing conductivity of the colloid. It is proved by direct measurement of conductivity. Thus, the critical frequency of the EHD disappearance increases.

According to the above mentioned expressions, a rise time decreases with voltage increasing that is proved by the experiment. In this case, a presence of particles increases a rise time in comparison with the pure LC. Probably, it is connected with an increase in viscosity and a reduction of elastic properties of LC and also with

overcoming the additional obstacles (particles) by ions. Meanwhile, nonconducting particles of aluminum oxide prevent to a rise of the instability with more degree than conducting silver particles. For the same reasons these particles prevent the instability decay while silver particles promote to this process.

4. CONCLUSIONS.

It was shown that the occurrence of silver particles in LC reduces the threshold voltage of the EHDI formation in a static field, and then it is more at low

frequencies and less at high ones than in the pure H37. Meanwhile, the limiting frequency of the EHDI disappearance increases. While aluminum oxide particles reduce the threshold voltage of the EHDI occurrence at low frequencies on greater value than silver particles and they increase it at the high frequencies. A presence of particles changes rise and decay times in comparison with the pure LC. It is connected with an increase in viscosity and a reduction of elastic properties of LC and also with overcoming of the additional obstacles (particles) by ions.

-
- [1]. *D. Demus, J. Goodby, G.W. Gray, H.W. Spiess, V. Vill*, Handbook of Liquid Crystals, Fundamentals, Wiley-VCH, Weinheim, New York, Chichester, Brisbane, Singapore, Toronto, 1998.
- [2]. *A. Buka, L. Kramer*, Pattern formation in Liquid crystals. Springer-Verlag, New York, Berlin, Heidelberg, 2006.
- [3]. *Sh. Kai, W. Zimmermann*, Pattern dynamics in the electrodynamics of nematic liquid crystals, Progress of Theoretical Physics Supplement, 99 (1989) 458-492.
- [4]. *D.K. Rout, R.N. Choudhary*, Electrohydrodynamic instability in some nematics cyanobiphenyl under a DC field, J.of PhysicsD: Applied Physics, 22 (1989) 127-134.
- [5]. *I.W. Smith, Y. Galerne, S.T. Lagerwall, E. Duboi-Violette, G. Durand*, Dynamic of electrohydrodynamic instabilities in nematic liquid crystals, J.de Physique, 36 (1975) C1-237-C1-259.
- [6]. *S. Chandrasekhar*, Liquid Crystals, Cambridge University Press, Cambridge, 1992.
- [7]. *E.F. Carr, R.W.H. Kozlowski, M. Shamsai*, Liquid Crystals and Ordered Fluids, eds. *A.G.Griffin, J.F.Johnson*, Plenum Press, New York, 1984.
- [8]. *M. Dennin, M. Treiber, L. Kramer, G. Ahlers, D.S. Cannel*, Origin of traveling rolls in electroconvection of nematic liquid crystals, Phys.Rev.Letters, 76 (1996) 319-322.
- [9]. *W. Helfrich*, Conduction-induced alignment of nematic liquid crystal: basic model and stability consideration, J.Chem.Phys., 51 (1969) 4092-4115.

Resevied:15.02.2013

CREATING OF ORDERED POROUS ANODIC ALUMINA TEMPLATES ON GLASS SUBSTRATES

Sh.O. EMINOV, Kh.D. JALILOVA, A.A. RAJABLI, G.Kh. MAMEDOVA,
J.A. GULIYEV, Z.I. BADALOVA

Institute of Physics of Azerbaijan National Academy of Sciences

AZ1143 H. Javid av. 33, Baku, Azerbaijan

E-mail: shikhamir@mail.ru

The preliminary results of the study on synthesis of porous anodic alumina (AAO) in the oxalic acid have been presented. The growth kinetics of AAO in potentiostatic mode has been studied. The transparent porous AAO films with ordered structure of the pores with a diameter between 20-40nm and a depth of 100-150 nm were prepared.

Keywords: anodic alumina oxide, AAO, porous aluminum oxide, PAA, nanoporous, oxalic acid solution.

PACS: 81.05.Rm, 81.16.Pr, 81.07-b, 82.45.Cc

INTRODUCTION

Nanoporous anodic aluminum oxide (AAO) membranes, with their fairly well-defined nanopore arrays have popular in various applications, such as catalysts or catalyst supports, biofilters, evaporation masks and as templates to fabricate of various one-dimensional nanostructures[1-4]. Over the past two decades, porous anodic alumina (PAA) has been widely used as a template to prepare various nanowire and nanotube arrays, including those of metals semiconductors, carbon and polymers. The PAA-assisted approach provides many advantages over conventional lithographic techniques for fabrication of simple sub-100nm nanostructured arrays, its parallel nature allows for the simultaneous preparation of nanostructured arrays over very large areas at low cost[4-6].

The present study aimed at the integrated investigation of the influences of the electrochemical parameters such as applied potential, electrolyte, anodization time and temperature on the micro-performance of AAO membranes.

EXPERIMENTAL DETAILS

Anodization is an electrolytic oxidation process in which the metal surface, when anodic is converted primarily to an adherent oxide coating having desirable thickness and structure.

Oxide layers with different morphological features can be formed by anodic oxidation of aluminum by varying the conditions during the electrochemical process, e.g. temperature, current density, voltage and duration of anodization. Therefore, we feel that it is imperative to include a brief description of the AAO template preparation. There are the following two different types of Al films were used for obtaining porous oxide films in our study: high purity Al foil (99,9 wt.%) with thickness of 10 μm and thin Al film was manufactured by magnetron evaporation on so-called "transparent conductive glass".

In the first case high purity Al foil was used for creating the self-ordering porous of oxide film on aluminum by anodization.

High-purity aluminum foils (99.999%) with smooth were employed in our experiment to fabricate the AAO template. The Al foil surface was first annealed at 500 $^{\circ}$ C

under air atmosphere for 2 h, degreased using acetone and alcohol, by ultrasonic vibration, then rinsed in distilled water. Al foil was electropolished in a mixed solution of $\text{HClO}_4:\text{C}_2\text{H}_5\text{OH}=1:4$ (V/V) for 5 min to provide a, then promptly rinsed with distilled water. Afterwards, the clean Al foil was anodized in an electrochemical bath at 4-6 $^{\circ}$ C for 2-4 hours with anodization voltage 40 V using the Al sample as anode plate and Pt mesh as the cathode in 0.3 M oxalic acid solution.

After 1 h anodization, the sample was immersed in a mixture of phosphoric acid and chromic acid to remove the porous aluminum oxide formed in the first anodization. The remaining Al foil was anodized for a second time under the same conditions for 8 h. Then the sample was etched by CuCl_2 solution to remove the aluminum substrate. During the second anodization, a thick porous alumina layer gradually grows over a very thin dense barrier oxide layer, which acts as an interface between the pure Al surface and porous alumina oxide layer. Fig. 1 is presented the anodization process of Al foil.

With the aim to create solar cells based on porous anodic alumina template on so-called transparent conductive glass, AAO templates were grown on a certain substrate such as indium tin oxide-coated glass (ITO-glass). In comparison with aluminum oxide fabricate from a pure aluminum foil, this kind of template is relatively short, its thickness ranging from a few hundreds of nanometers to a few microns. The substrate usually functions as an electrode as well as mechanical support.

The glass/ITO substrate were cut into 1 by 4 pieces and cleaned in ultrasonic acetone and rinsed in de-ionized water. Next in asset of experiments titanium layer with thickness from 1-50 nm were sputtered on ITO for comparison. Annealing in air was performed for some of these samples at 400 $^{\circ}$ C for up to 5 hours. We use thermoelectric refrigerators and also use mini motors for mixing. The current density we can regulate with potentiostat П-5827 and also power pack БП-50. For electrodeposition a current density of 15mA/sm 2 was applied for several second. The 1 μm aluminum films deposited on cleaned plain glass by thermal vacuum evaporation at a rate of 2nm/s with a chamber pressure of 3 $\cdot 10^{-6}$ Torr by Z-550 Leybold-Heraeus. The aluminum source had a purity of 99,9%.The anodic alumina film

CREATING OF ORDERED POROUS ANODIC ALUMINA TEMPLATES ON GLASS SUBSTRATES

was fabricated by an anodization process which conducted in 0.4 M oxalic acid solutions at 15⁰C under a constant voltage of 40-60 V, while the electrolyte was mechanically stirred. To get highly ordered pores of aluminum oxide ,the produced alumina layer was removed by wet chemical etching in a phosphoric acid

(6%) at 60⁰C. A relatively dark anodic alumina film with a well-defined pore structure was produced in this process. The film thickness was 300-400nm, measured by a scanning electron microscope AIST-NT Smart SPM. The transmittance of this patterns measured by Specord - 250-222P192.

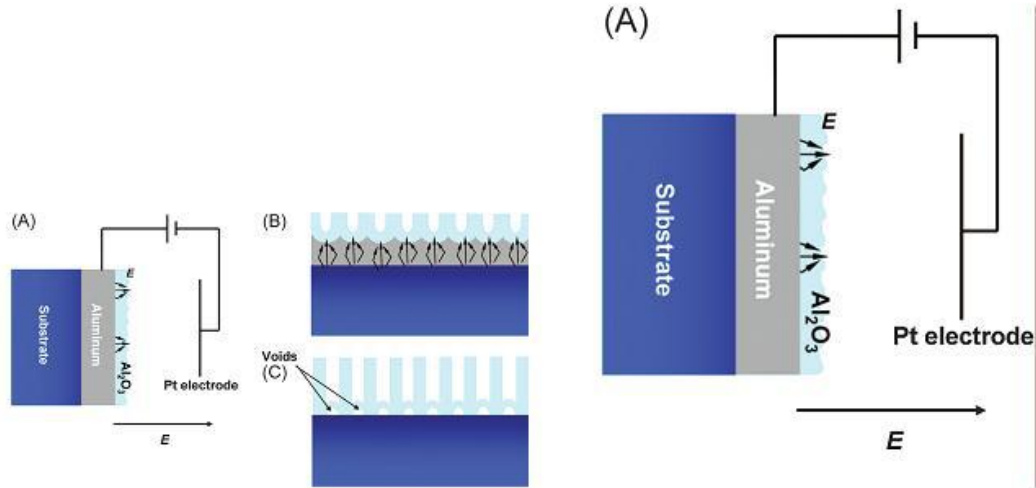


Fig. 1. Schematic of the anodization process. (a) The Al-coated substrate is placed opposite to an inert Pt-mesh counter electrode in an acidic electrolyte and a voltage is applied across the electrodes. (b) Due to higher local electric field and temperature, the Al₂O₃ formed at depressions in the Al film are more rapidly dissolved than the rest of the film resulting in pore formation. (c) Inverted-U shaped barrier layers are formed at the bottom of the AAO pore channels at the end of the anodization process.

RESULTS AND DISCUSSIONS.

From the results of experiments, the integrated impact of the anodization parameters, including the applied potential, electrolyte temperature and time, on the average pore diameters, thickness and regularity of the AAO were concluded. The average pore diameters were mainly affected by potential and electrolyte. The image of the AAO sample with a porous layer is presented in the Fig.2. This sample is transparent for visible light, but for demonstration of the interference from the surface to around on the corresponding angle.

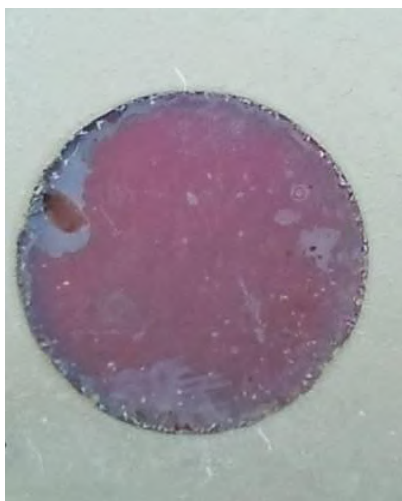


Fig.2. Photograph of PAA sample with a porous layer

The Fig.3 shows the current versus time data obtained during the formation of the PAA template and explain well the process anodization.

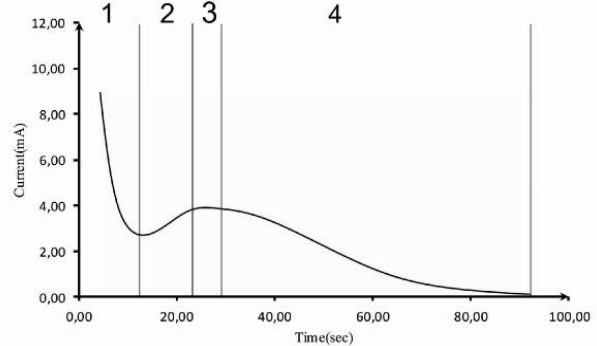


Fig.3. Anodization current vs. time of Al anodization

This sample was taken out of the electrolyte after 100 seconds of anodization, where a current rise was detected. Four stages can be distinguished from the plot. At the 1st the current is very high due to the high conductivity of metal Al and the lack of any oxide layer. As O₂ and OH ions diffuse to the Al surface, an Al₂O₃ anodization front is created. So aluminum oxide layer formed on the top surface of the evaporated aluminum film, greatly increasing the resistance. Correspondently, this stage can be called the *oxidation stage* and generally lasts for 20~30 seconds. Because the Al₂O₃ at the anodization front is not perfectly smooth, the electric field in the sample concentrates at depressions in the Al₂O₃ layer. Due to higher local electric field and temperature, its formed at the depressions is preferentially dissolved resulting in the for-

mation of pore channels as the anodization proceeds. This resulted in the 2nd stage, during which the pre-formed oxide layer started to dissolve from some random sites on the oxide surface and nanopores were initiated. This had an overall effect of thinning the oxide layer, thus the resistance decreased and current increased a bit. This can be called the *dissolution stage*, and lasts for a few minutes. In the 3rd stage, the oxide formation the process and dissolution process gradually balanced each other and an equilibrium state was achieved. Also the pores started to form an ordered structure by self-adjusting pore sizes and inter-pore spaces. The anodization current was constant during this stage. Note that the time period of this stage could range from a few seconds to several tens of minutes or even longer, depending upon the thickness of the aluminum layer. This can be called the steady stage. The three stages mentioned above commonly exist in all kinds of aluminum anodization, but the last following stage 4th can be observed only when the whole Al layer is consumed. Fig.4 is shown transmission spectrum of PAA obtained from Al foil. The transmittance spectrum in fig. 5 of PAA on ITO is pretty close to the ITO substrate itself. The transmittance of such a template on ITO was measured to demonstrate the capability of its application in electric optical devices.

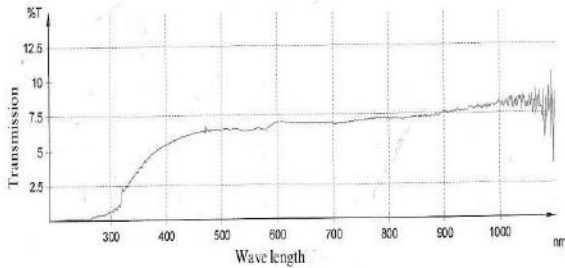


Fig.4. Transmittance spectrum of PAA, obtained on 10 μ m thick alumina foil.

It shows the transmittance of waveband between 200-1000nm for Al(200nm) /Ti(5nm) /ITO /glass. Absorption edge of this films is 250 nm, which coincided for the sapphire and other configuration of Al₂O₃. In wave length 500nm the transmittance had 7-8% ,that coincided in 1-2 % ultraviolet range. The extent of transmittance depends on both the thickness of AAO films and remaining non oxidized aluminum layer. From ellipsometric characterization the thickness of AAO layer is 1.2 nm.

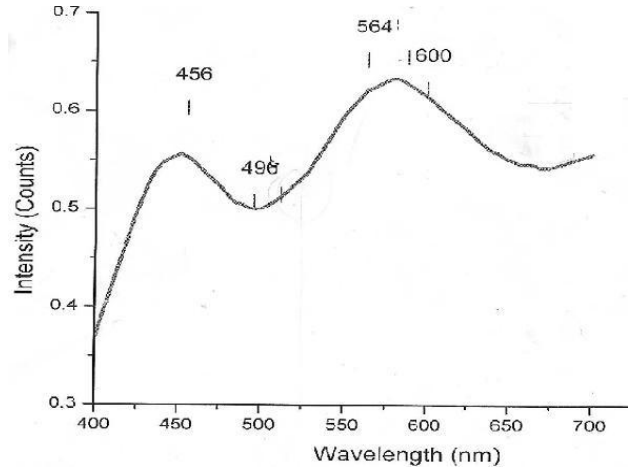


Fig.5. Transmittance spectra of PAA prepared on Al-ITO-Glass system.

The AFM image of the AAO sample with the porous are presented in Fig.6 in 2D-3D scale, in the currents density 15 mA/cm². It showed the nanowire diameters of about 20-30 nm, depth of about 100-150nm and distance between them 5nm.

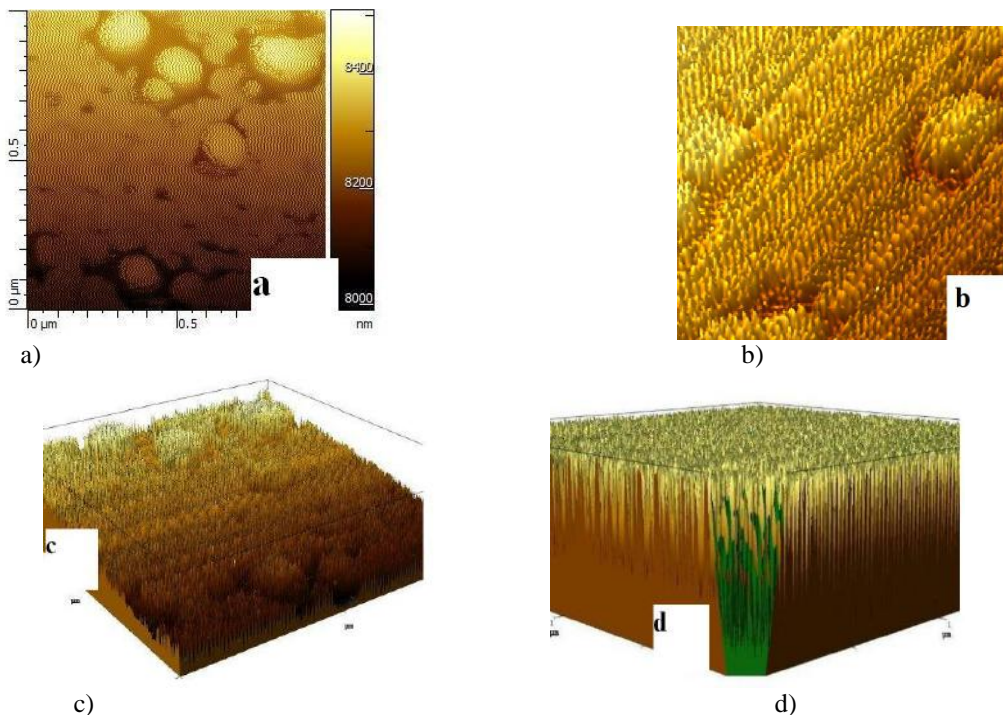


Fig. 6. AFM images in 2D and 3D scale of AAO templates

CONCLUSION

The preliminary results of the study on synthesis of porous anodic alumina AAO in the oxalic acid have been presented. The growth kinetics of AAO in potentiostatic mode has been studied. The transparent porous AAO films with ordered structure of the pores with a diameter between 20-40nm and a depth of 100-150 nm were prepared.

It was believed that during the anodization of aluminum the porous layer formed is assumed to be of Al₂O₃. The atomic density of aluminum in Al₂O₃ is lower than that of metallic aluminum by a factor of two. The volume expansion of Al₂O₃ will be nearly twice that of the original aluminum metal. This volume expansion takes place at the metal/oxide interface leading to a compressive stress during oxide formation. This stress is the origin of the repulsive forces that appear between the neighboring pores and it is believed that volume expansion in the vertical direction pushes the pore wall upward.

The spontaneous high-ordered which happen on Al₂O₃ oxide both surface and volume, suppose the tendency of the system to take the corresponding of the minimum potential energy configuration. It is the motive force of many self-organized processes. Apparently, the system's condition with minimum of the mechanical strains on the interface of oxide-metal is more stabilities and at any mechanism of charge carriers through border (the anodizing mechanism) such system will be more predisposed to the ordering of process. Transparent porous anodic aluminum oxide films on glass have been prepared. The residual aluminum layer in porous anodic aluminum oxide films was fully converted to aluminum oxide by an ion-drift process without alternating its nanostructure. The adhesion between the anodic alumina film and the glass substrate and the transparency of the films were greatly improved. The ion-drift process not only converts the residual aluminum to transparent aluminum oxide but also forms strong chemical bonds at the interface.

-
- [1] *H. Masuda, K. Fukuda.* "Ordered metal nanohole arrays made by a two-step replication of honeycomb structures of anodic alumina." *Science*, **268** (1995) 1466 -1468.
 - [2] *Wei Wei., Songmei Li, Jianhua Liu Jun Zhang.* "Size-controlled synthesis of highly ordered nanoporous AAO membranes." *Nanoscience*, **11** (2004) 157-160.
 - [3] *A.N. Belov, S.A. Gavrillov, V.I. Shevyakov.* "Osobenosti poluceniya nano-strukturuirovanogo anodnogo oxide aluminiya." *Rossiyskikie nanotexnologii*. **1** (2006) 223-227.
 - [4] *R.P. Cowburn, A.O. Adeyey.* "Configurational anisotropy in nanomagnets" *Phys Rev Lett.*, **81** (1998) 5414-5417.
 - [5] *X. Zhang, Y. Hao, G. Meng et al.* "Fabrication of highly ordered InSb nanowires arrays by electrodeposition in porous anodic alumina membranes." *J. Electrochem. Soc.* **25** (2005) 664-668.
 - [6] *Sung-Jin Park, Hyung Sup Lee et.a.* "Nanoporous anodic alumina film on glass. Improving transparency by an ion-drift process." *Electrochem. and Solid-State Letters* **8**(3) (2005)D5-D7.
 - [7] *V.A. Sokol.* "Osobenosti rosta poristogo oxide aluminiya." *Dokladi BGUIR* **1** (2003) 75 82.
 - [8] *P.G. Miney, P.E. Colavita, M.V. Shiza, et.al.* "Growth and Characterization of a Porous Aluminum Oxide Film formed on an Electrically Insulating Support." *Electrochem. Solid-State Lett.*, **6**, (2003) B42 - B46.

Resevied:12.02.;2013

DECREASE IN RISK ERRONEOUS CLASSIFICATION THE MULTIVARIATE STATISTICAL DATA DESCRIBING THE TECHNICAL CONDITION OF THE EQUIPMENT OF POWER SUPPLY SYSTEMS

E.M. FARHADZADEH, Y.Z. FARZALIYEV, A.Z. MURADALIYEV
Azerbaijan Scientific-Research and Design-Prospecting Institute of Energetic
 AZ1012, Ave. H.Zardabi-94, e-mail:fem1939@rambler.ru

Objective estimation of parameters of individual reliability is an indispensable condition of an opportunity of decrease in operational expenses for maintenance service and repair of the equipment and devices of electro power systems. The method of decrease in risk of erroneous classification of multivariate statistical data offered. The method based on imitating modeling and the theory of check of statistical hypotheses.

Keywords: risk erroneous classification, equipment of power supply systems

PACS: 89.20.Bb; 52.80; 52.59 84.40;84.70

Estimation parameters of individual reliability of the equipment of power supply systems provides classification of final population of multivariate statistical data of operation, tests and restoration of deterioration on the set versions of attributes (VA) [1].

VA reflects features of a design, a condition of operation, feature of occurrence of refusals and carrying out of repairs of the equipment. Expediency of classification on each of population VA is established by comparison of statistical functions of distribution (s.f.d.) final population of statistical data $F_{\Sigma}^*(X)$ and s.f.d. samples n random variables from this population on i versions of V attribute $F_{v,i}^*(X)$, where $v=1, k$; k -number of attributes of random variable X (for example, durations of emergency repair); $i=1, rk$; r_k - number of versions k an attribute. If s.f.d. $F_{\Sigma}^*(X)$ and $F_v^*(X)$ differ not casually, in other words, sample $\{X\}_n$ where n -number of random variables of sample, it is not representative classification of data at an estimation of parameters of individual reliability is expedient and on the contrary. It is necessary to note, that unlike sample of a general data population (analogue: infinite set of random variables with uniform distribution in an interval $[0,1]$), which imposing appearance is set by some significance value α , sample of final population of multivariate data on set VA is not casual, as a matter of fact, and it can appear only representative. In particular, sample can appear representative, if for considered data set VA not significant.

In a basis of comparison $F_{\Sigma}^*(X)$ and $F_v^*(X)$ there is a statistical modeling (by means of computer program RAND) n pseudo-random numbers ξ , random variables of sample equal to number, with uniform distribution in an interval $[0,1]$.

Indispensable condition thus is consistency s.f.d. $F_v^*(\xi)$ to the uniform law of distribution $F_{\Sigma}(\xi)$, in other words, casual character of distinction $F_{\Sigma}(\xi)$ and $F_v^*(\xi)$. It is obvious, that from the uniform law of change of random numbers ξ at all consistency does not follow the uniform law s.f.d. $F_v^*(\xi)$ with the set significance value

α . Use at modeling statistical analogue $F_v^*(X)$ s.f.d. $F_v^*(\xi)$, essentially differing from $F_{\Sigma}(\xi)$, leads to erroneous increase in value of the greatest divergence of distribution of this analogue $F_v^{**}(X)$ from $F_{\Sigma}^*(X)$ and by that to growth of probability of the erroneous decision at classification of data.

Representative character of sample $\{\xi\}_n$ at the decision of a problem of an estimation of expediency of classification of multivariate data it was supervised Kolmogorov's by criterion [2]. According to this criterion sample $\{\xi\}_n$ it is unrepresentable, if

$$D_n > d_{n,(1-\alpha)} \tag{1}$$

where: $D_n = \max(D_n^+, D_n^-)$ (2)

$$D_n^+ = \max\{D_i^+\}; \quad 1 \leq i \leq n \tag{3}$$

$$D_i^+ = \left(\frac{i}{n} - \xi_i\right) \tag{4}$$

$$D_n^- = \max\{D_i^-\}; \quad 1 \leq i \leq n \tag{5}$$

$$D_i^- = \left(\xi_i - \frac{i-1}{n}\right) \tag{6}$$

$d_{n,(1-\alpha)}$ – critical value of statistics D_n provided that $F_{\Sigma}(\xi)$ and $F_v^*(\xi)$ differ casually

In [3] it is marked, that estimation D_n under the formula

$$D_n' = \max\left\{\left|D_i^+\right|\right\}; \quad 1 \leq i \leq n \tag{7}$$

leads to incorrect decisions on a parity $F_{\Sigma}(\xi)$ and $F_v^*(\xi)$.

The similar remark can be found and in [4]. The reason of such discrepancy does not stipulate. At uncertain in advance n , decrease in time of calculation, according to [3], is reached by application of exact approach Stephens, which tabulated critical values $d_{n,(1-\alpha)}$, depending from n and α , reduces to dependence only from α . Sample $\{\xi\}_n$ it is unrepresentable, if

$$A \cdot D_n > C_{1-\alpha} \quad (8)$$

where:

$$A = \left(\sqrt{n} + 0.12 + \frac{0.11}{\sqrt{n}} \right) \quad (9)$$

For example, at $n=4$ size $A=2,175$ and for $\alpha=0,1$ critical value $C_{1-\alpha}=1,224$, and at $\alpha=0,05$ size $C_{1-\alpha}=1,358$.

Application of a method of the decision of «a return problem» when it is in advance known, that sample $\{\xi\}_n$ it is unrepresentable, has shown, that criteria (1) and (8) for values most often used in practice $\alpha=0,05$ and $\alpha=0,1$ not

casual character of divergence $F_\Sigma(\xi)$ and $F_V^*(\xi)$ at small n establish only for those cases when it does not raise the doubts. For acknowledgement of this statement, we shall consider a following example.

Let random numbers ψ have uniform distribution $F_\Sigma(\psi)$ in an interval $[0.5; 1]$. Casual sample is set $\{\psi\}_n$ with $n=4$: $\{0,86346; 0,50672; 0,91424$ and $0,67210\}$. Check up the assumption of imposing appearance of this sample for the uniform law of distribution of a random variable ξ in an interval $[0,1]$.

Results of calculations are resulted in table 1.

Table 1

Example of an estimation of imposing appearance of sample

i	$F_\Sigma(\psi_i)$	i/n	D_i^+	D_i^-	The note
1	0.507	0.25	-0.257	+0.506	$D_i^+ = 0.086$; $D_i^- = 0.506$ $D_n=0.506$; $D_{n<d4; 0.9}=0.565$ $AD_n=1.101$; $AD_n < C_{0.9}=1.224$
2	0.672	0.5	-0.172	+0.422	
3	0.863	0.75	-0.113	+0.363	
4	0.914	1.00	+0.086	+0.164	

As sample follows from table 1 $\{\psi\}_4$ does not contradict the assumption of imposing appearance rather $F_\Sigma(\xi)$ at $\alpha=0,1$.

These features and some assumptions of the reasons of their occurrence [5] have demanded to pass from the analysis of absolute values of the greatest divergence of distributions $F_\Sigma(\xi)$ and $F_V^*(\xi)$, to the analysis of the valid values of the greatest divergence (St_n). Thus under

«the greatest divergence $F_\Sigma(\xi)$ and $F_V^*(\xi)$ » we shall understand the greatest on the module vertical distance between $F_\Sigma(\xi)$ and $F_V^*(\xi)$ with $i=1, n$.

Calculations St_n were spent according to the algorithm, integrated which block diagram is resulted in figure 1.

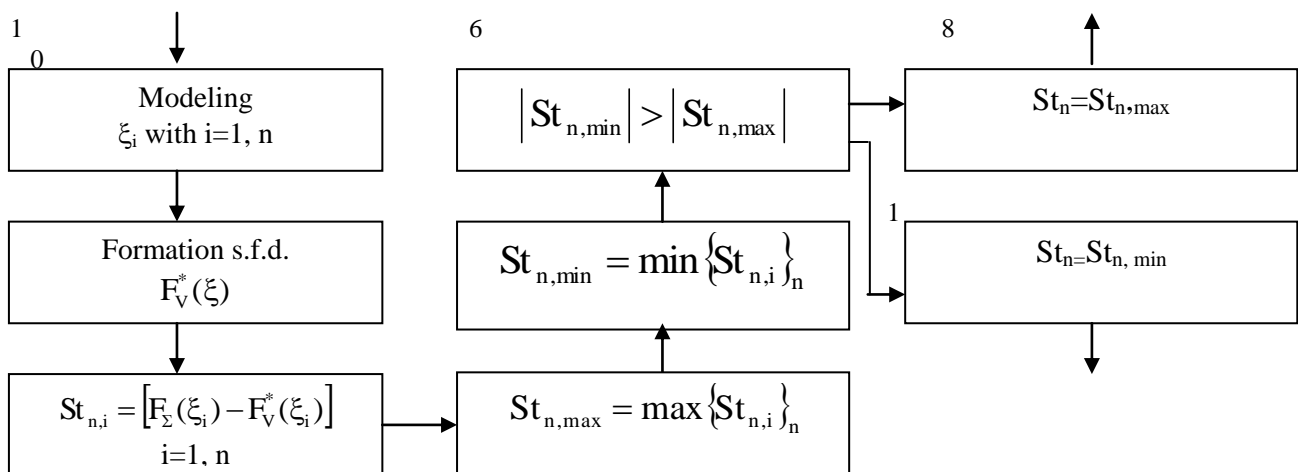


Fig.1. Block diagram of algorithm of calculation of the greatest divergence of distributions $F_\Sigma(\xi)$ and $F_V^*(\xi)$

Application of formulas of type

$$St_n = \max \left(\xi_i - \frac{i}{n} \right) \quad 1 \leq i \leq n \quad (10)$$

calculation on the computer leads to erroneous results. For example, according to table 1 the maximal value among four realizations of size D_i^+ will, $D_i^+ = 0.086$, and the greatest vertical divergence between $F_\Sigma(\xi)$ and $F_V^*(\xi)$ it is equal $D_i^+ = -0.256$

Results of ordering of given realizations St_n presented in table 2 and allow concluding:

1. Quintile distributions $F^*(St_n)=\alpha$ and $n \geq 2$ are equal on size and are opposite on a sign (distinction in a sign is caused by distinction of formulas 4 and 10) quintiles distributions $F(D_n)=2\alpha$ {see tabl.16 [2]};
2. Distribution $F^*(St_n)$ is asymmetrical. In the illustrative purposes on fig. 2 are resulted s.f.d. $F^*(St_n)$ for of some n . The assumption of symmetry of distribution

$F(St_n)$ it is possible to explain discrepancy of probability practically equal quintile distributions $F^*(St_n)$ and $F(D_n)$;

3. Than ξ_n it is less, that negative value on sign St_n on size will be more, since $St_n=(\xi_{n-1})$. On experimental data the least value St_n for $n=2$ has appeared equal $St_n=-0,992$, and the greatest $St_n=+0,489$ at sup equal, accordingly, 1 and 0,5.

4. In distribution $F^*(St_n)$ distinguish the bottom St_n and top $\overline{St_n}$ boundary values with a significance value α , i.e.

$$\left. \begin{aligned} F^*(St_n) &= \alpha/2 \\ F^*(\overline{St_n}) &= (1-\alpha/2) \end{aligned} \right\} \quad (11)$$

It is established, that if $0,25 \geq F^*(St_n) \geq 0,75$, i.e. if $\alpha \leq 0,5$

$$\overline{St_n} = -\left(\frac{1}{n} + St_n\right) \quad (12)$$

For example, for $n=4$ and $\alpha=0.10$ according to distribution $F^*(St_n)$ (see tabl.2) size $St_4 = -0.567$, and $\overline{St_4} = +0.319$. At the same time under the formula (12) $-(0,25-0,567=0,317=\overline{St_4}$

If $n=29$ and $\alpha=0,2$, that $St_n = -0.193$ and $\overline{St_n} = 0.158$. The size $\overline{St_n}$ under the formula (12) is equal $-(0,034-0,193)=0,159$
On fig. 3 histograms of distribution of negative and positive values St_n for $n=4$ and $n=29$ are resulted.

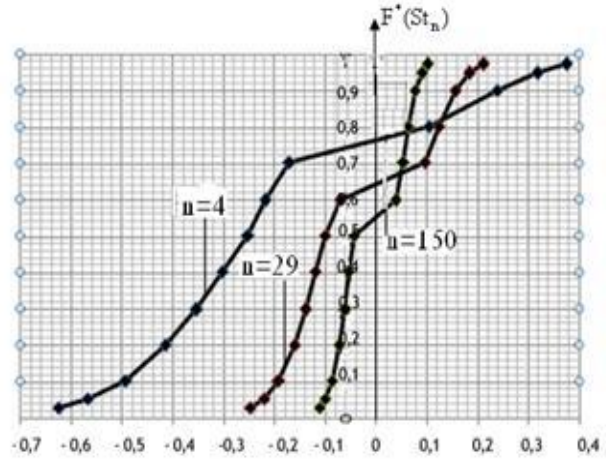


Fig.2. S.f.d. $F^*(St_n)$ for of some n

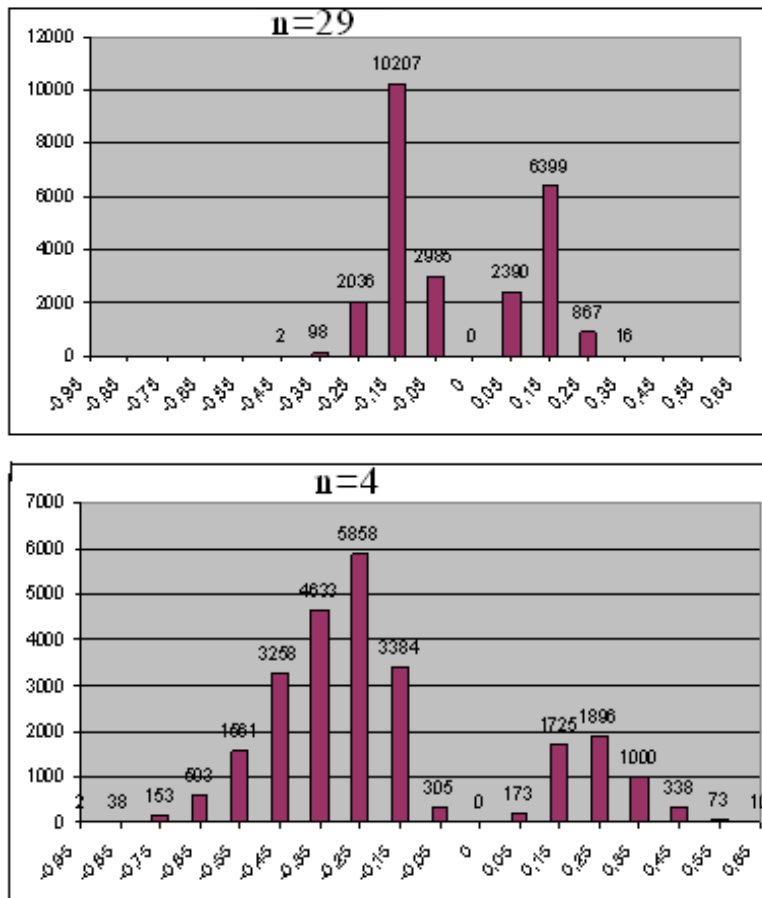


Fig.3. Histograms of distribution of the greatest divergence of distributions $F_{\Sigma}(\xi)$ and $F_V^*(\xi)$

Table 2

Some results of an estimation s.f.d. $F^*(St_n)$

$F^*(St_n)$ n	0,025	0,05	0,1	0,2	0,3	0,4	0,5	0,6	0,7	0,8	0,9	0,95	0,975
2	-0.842	-0.775	-0.684	-0.551	-0.473	-0.149	-0.363	-0.304	-0.239	-0.060	0.184	0.285	0.343
3	-0.7094	-0.635	-0.566	-0.471	-0.400	-0.335	-0.296	-0.252	-0.200	-0.145	0.231	0.299	0.372
4	-0.623	-0.567	-0.494	-0.414	-0.355	-0.302	-0.253	-0.217	-0.173	0.155	0.240	0.319	0.377
5	-0.567	-0.511	-0.449	-0.370	-0.318	-0.274	-0.232	-0.190	-0.147	0.164	0.246	0.309	0.360
6	-0.523	-0.469	-0.411	-0.338	-0.292	-0.252	-0.215	-0.173	-0.127	0.171	0.244	0.303	0.358
7	-0.481	-0.438	-0.384	-0.318	-0.274	-0.235	-0.201	-0.162	-0.113	0.165	0.235	0.290	0.342
11	-0.389	-0.353	-0.309	-0.255	-0.219	-0.189	-0.110	-0.129	-0.097	0.160	0.216	0.260	0.302
16	-0.33	-0.295	-0.258	-0.215	-0.184	-0.158	-0.134	-0.103	0.107	0.150	0.194	0.232	0.264
22	-0.280	-0.253	-0.221	-0.183	-0.157	-0.135	-0.113	-0.083	0.105	0.137	0.176	0.210	0.235
29	-0.246	-0.219	-0.193	-0.160	-0.138	-0.119	-0.099	-0.068	0.098	0.126	0.158	0.186	0.212
40	-0.208	-0.187	-0.164	-0.136	-0.119	-0.102	-0.084	-0.050	0.089	0.112	0.140	0.164	0.185
60	-0.173	-0.156	-0.137	-0.114	-0.097	-0.083	-0.069	0.054	0.077	0.096	0.118	0.138	0.155
90	-0.142	-0.127	-0.111	-0.092	-0.079	-0.068	-0.055	0.051	0.067	0.081	0.100	0.116	0.130
120	-0.122	-0.110	-0.096	-0.080	-0.068	-0.059	-0.047	0.047	0.060	0.072	0.089	0.102	0.114
150	-0.110	-0.099	-0.086	-0.071	-0.062	-0.053	-0.042	0.041	0.053	0.065	0.079	0.092	0.104

As follows from fig. 3, negative values St_n essentially exceed positive values St_n on relative number and an interval of change. Proceeding from i. 3 it is clear, that it not casually and does not testify about unrepresentable samples. With growth n the parity of negative and positive values St_n decreases and aspires to unit. For $n=2$ negative values St_n make 87,5%, and for $n=29$ - 61%, and for $n=150$ - 55%. Thus, even at $n=150$ quintile distributions $F^*(St_n)$ at $\alpha=0,05$ and $\alpha=0,95$ are not equal $[-0.099; +0.092]$. Histograms also explain laws of distribution $F^*(St_n)$ resulted on fig.2.

On fig. 4 curve changes of boundary values of statistics St_n for of some values s.f.d. are resulted, $F^*(St_n)$. Criterion of the control of imposing appearance of sample $\{\xi\}_n$ with a significance value α thus looks like:

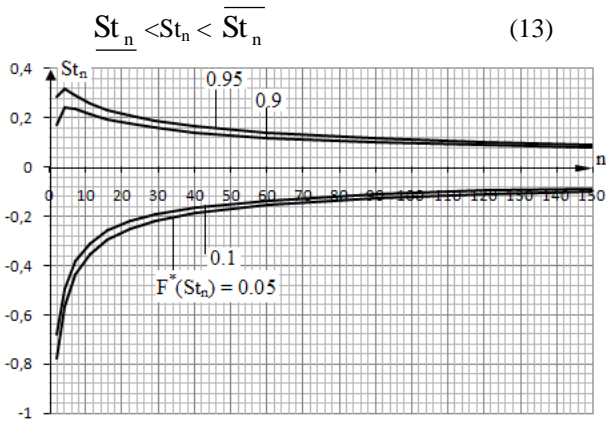


Fig.4. Laws of change of boundary values of the greatest divergence of distributions $F_Z(\xi)$ and $F_V^*(\xi)$

Let's designate positive values St_n through St_n^+ , and negative values- St_n^-

In view of i.1. and the equations (12), sample $\{\xi\}_n$ with a significance value $\alpha \leq 0,5$ can be accepted

representative, if

$$\left. \begin{aligned} St_n^+ &< \left[d_{n,(1-2\alpha)} - \frac{1}{n} \right] \\ |St_n^-| &< d_{n,(1-2\alpha)} \end{aligned} \right\} \quad (14)$$

As

$$\left(St_n^+ + \frac{1}{n} \right) = |St_n^-|$$

criterion (13) for a significance value α can be presented, as

$$\left(\overline{St_n^+} + \frac{1}{n} \right) = |St_n^-| = d_{n,(1-2\alpha)} \quad (15)$$

Here it is necessary to pay attention to discrepancy of the equations of importance St_n and $d_{n,(1-2\alpha)}$. If again to address to data of table 1 it is easy to notice, that the interval criterion (13), allowing to consider a sign on the greatest divergence St_n , also is unable to establish unrepresentable character of sample $\{\psi\}_n$.

It is known, that decrease in risk of the erroneous decision at classification of data can be reached by the account not only errors I type, but also the II types [4].

The most simple decision of this problem would be comparison St_n between $F_Z(\xi)$ and $F_V^*(\xi)$ with boundary values of the interval $[St_n^-; St_n^+]$ corresponding a significance value $\alpha=0,5$. It is that limiting case of values α when $St_n=0$. Thus a errors II type $\beta=(1-\alpha)$, i.e. also it is equal 0,5. If α to accept it is less, than 0,5 the errors II type increases β .

In real conditions:

- configurations $F_Z(\xi)$ also $F_V^*(\xi)$ are various, i.e. $St_n \neq 0$;
- for the same value St_n size $(\alpha+\beta)$ less or it is equal to unit;
- in process of increase St_n size $(\alpha+\beta)$ decreases, reaches the minimum ($St_{n,opt}$) and then increases;
- if $St_n < St_{n,opt}$, then $\alpha > \beta$, if $St_n > St_{n,opt}$, then $\alpha < \beta$;
- distinction between α and β increases in process of increase in a divergence between St_n and $St_{n,opt}$.

Comparison of realizations St_n to boundary values St_n^- and St_n^+ , calculated accordingly, for $F^*(St_n^-) = 0.25$ and $F^*(St_n^+) = 0.75$, allows to not calculate s.f.d., which defines a errors II type β , that it is possible to carry to advantages of this way. Its lacks are necessity of increase twice numbers of modeled realizations of distribution $F_V^*(\xi)$, unjustified decrease in disorder St_n , the heuristic approach.

Algorithm of calculation s.f.d., describing the greatest deviation $F_Z(\xi)$ and $F_V^*(\xi)$, provided that $F_V^*(\xi)$ it is unrepresentable, consists of following sequence of calculations:

1. It is modeled next (from necessary N realizations) their sample n random numbers;
2. It is formed s.f.d. $F_V^*(\xi)$;
3. The greatest divergence between F is defined $F_Z(\xi)$ and $F_V^*(\xi)$. Designate this size as $St_{n,e}$ where the index «e» corresponds to empirical character of sample.

Having defined statistical characteristics of this sample $\{F_V^*(\xi)$ and $St_{n,e}\}$, start formation s.f.d. $F^*(St_n^*)$ on realizations of the greatest divergence between functions of distribution $F_Z(\xi)$ and set (N) s.f.d. $F_V^*(\psi)$, modeled on s.f.d. $F_V^*(\xi)$. For what:

4. On s.f.d. $F_V^*(\xi)$ distribution is formed

$$F_V^*(\psi) = \begin{cases} 0 & \text{if } \psi \leq \psi_1 \\ \frac{i-1}{n+1} + \frac{(\psi - \psi_i)}{(\psi_{i+1} - \psi_i)(n+1)} & \text{if } \psi_1 < \psi < \psi_{n+1} \\ 1 & \text{if } \psi \geq \psi_{n+1} \end{cases} \quad (16)$$

5. Under standard program RAND the random number is modeled ξ with uniform distribution in an interval $[0,1]$;

6. On distribution (16) calculated corresponding probability ξ random number ψ . Calculations are spent under the formula

$$\psi = \psi_i + (\psi_{i+1} - \psi_i)[\xi \cdot (n + 1) - (i - 1)] \quad (17)$$

with $i=1, (n+1)$

7. Items 5 and 6 repeat n time;

8. On sample $\{\psi\}_n$ is under construction s.f.d. $F_V^*(\psi)$;

9. The greatest divergence between $F_\Sigma(\xi)$ and $F_V^*(\psi)$ is defined. Designate it through St_n^* ;

10. Items (5÷9) will repeat N time;

11. Average value of a random variable St_n^* defined. Designate it through $M^*(St_n^*)$;

12. On N to values, St_n^* it is formed s.f.d. $F^*(St_n^*)$.

If to assume, that distribution $F^*(St_n^*)$ corresponds to the normal law of distribution, average value $M^*(St_n^*)$ is equal $St_{n,e}$ and corresponds $F^*(St_n^*) = \beta = 0,5$, for all realizations $St_{n,e}$, which probability $0.1 < \alpha < 0.5$, the preference should be given to assumption H_2 . However, the assumption of the normal law of distribution of function $F^*(St_n^*)$ mismatches the validity. As an example on fig.5 the histogram of distribution of realizations St_n^* for s.f.d. is resulted. $F_V^*(\psi)$, resulted in table 1.

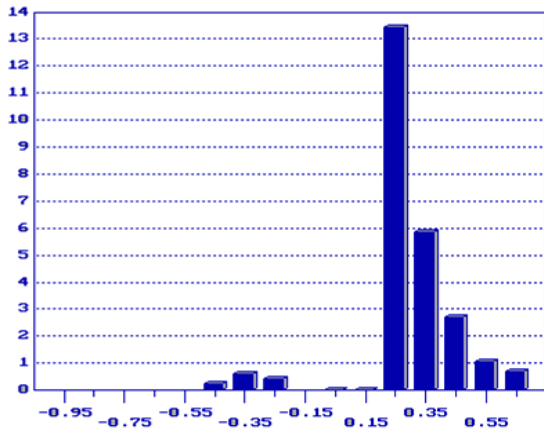


Fig.5. Histogram of realizations St_n^*

Let's enter into consideration two assumptions:

H_1 - sample $\{\psi\}_n$ reflects laws of distribution $F_\Sigma(\xi)$;

H_2 - sample $\{\psi\}_n$ does not reflect law of distribution $F_\Sigma(\xi)$.

The recommended algorithm of decision-making depends on a parity of average values of realizations St_n and St_n^* . In this connection the distribution describing risk of the erroneous decision in function St_n designate $Sh1(St_n)$, and in function $St_n^* - Sh2(St_n)$.

$$\text{At } M^*(St_n) < M^*(St_n^*)$$

$$\left. \begin{aligned} Sh1(St_n) &= 1 - F^*(St_n) \\ Sh2(St_n) &= F(St_n^*) \end{aligned} \right\} \quad (18)$$

Algorithm of decision-making looks like:

$$\left. \begin{aligned} \text{If } St_{n,e} &\geq \overline{St_n}, \text{ then } H_2, \text{ else} \\ \text{If } St_{n,e} &\leq \underline{St_n^*}, \text{ then } H_1, \text{ else} \\ \text{If } Sh1(St_n) &\ll Sh2(St_n), \text{ then } H_2, \\ \text{Otherwise } &H_1 \end{aligned} \right\} \quad (19)$$

$$\left. \begin{aligned} Sh1(St_n) &= 1 - F^*(St_n^*) \\ Sh2(St_n) &= F^*(St_n) \end{aligned} \right\} \quad (20)$$

Algorithm of decision-making looks like:

$$\left. \begin{aligned} \text{If } St_n &\geq \overline{St_n^*}, \text{ then } H_1, \text{ else} \\ \text{If } St_{n,e} &\leq \underline{St_n}, \text{ then } H_2, \text{ else} \\ \text{If } Sh1(St_n^*) &\gg Sh2(St_n), \text{ then } H_2, \\ \text{Otherwise } &H_1 \end{aligned} \right\} \quad (21)$$

Otherwise H_1

In the illustrative purposes on fig. 6 functions of distribution $Sh1(St_n)$ and $Sh2(St_n)$ are resulted. calculated according to table 1.

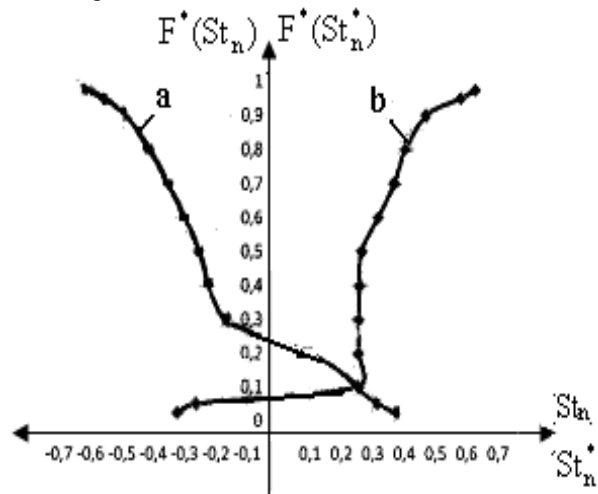


Fig. 6. Laws of change s.f.d. $F^*(St_n)$ and $F^*(St_n^*)$ for $n=4$:

a - s.f.d. $F^*(St_n)$; b - $F^*(St_n^*)$

As $M^*(St_n)$ it has appeared less than $M^*(St_n^*)$ functions of distribution $Sh1(St_n)$. and $Sh2(St_n)$. were calculated accordingly under the formula (18).

In table 3 numerical values of the parameters defining result of the decision are systematized. As follows from tab. 3 as $Sh1(St_{n,e}) \ll Sh2(St_{n,e})$, the preference, according to (19) is given assumption H_2 . In other words, attraction to the statistical analysis of size of a errors I type and errors II types, allows distinguish unrepresentable samples.

Table 3

The basic parameters of calculation

Parameter	Conditional designation	Estimation
1. Number casual sample	n	4
2. Average value of the greatest divergence of distributions $F_{\Sigma}(\xi)$ and $F_V^*(\xi)$	$M^*(St_n)$	-0,207
3. Average value of the greatest divergence of distributions $F_V^*(\psi)$ and $F_V^*(\psi)$	$M^*(St_n^*)$	0,292
4. Empirical value of the greatest divergence of distributions $F_{\Sigma}(\xi)$ and $F_V^*(\xi)$	$St_{n,e}$	0,257
5. Boundary values of an interval of change St_n c $\alpha=0.1$ top bottom	$\overline{St_n}$ $\underline{St_n}$	0,319
6. Boundary values of an interval of change St_n^* with $\alpha=0,01$ top bottom	$\overline{St_n^*}$ $\underline{St_n^*}$	-0,567 0,544
7. Probability $St_{n,e}$ on s.f.d. $[1 - F^*(St_n)]$ on s.f.d. $F^*(St_n^*)$	$\underline{St_n^*}$ $Sh1(St_{n,e})$ $Sh2(St_{n,e})$	0,292 0,09 0,42
8. The assumption is accepted	H	H_2

It is necessary to note, that attraction to an estimation of character of a divergence of distributions $F_{\Sigma}(\xi)$ and $F_V^*(\psi)$ distributions $F^*(St_n^*)$ for all realizations samples it is unjustified, as for of some from them, for example at $Sh1(St_n) \geq 0,5$ sample $\{\psi\}_n$ it is most truly representative, and at $Sh1(St_n) \leq 0,1$ – it is unrepresentable.

There fore calculations s.f.d. $F^*(St_n^*)$ offered to spend for following conditions:

$$\left. \begin{aligned}
 1. \quad & M^*(St_n) < M^*(St_n^*) \\
 & \underline{St_{n,0.05}} < St_{n,\vartheta} < \overline{St_{n,0.95}} \\
 & \underline{St_{n,0.25}} \geq St_{n,\vartheta} \geq \overline{St_{n,0.75}}
 \end{aligned} \right\} \quad (22)$$

$$\left. \begin{aligned}
 2. \quad & M^*(St_n) > M^*(St_n^*) \\
 & \underline{St_{n,0.05}} < St_{n,\vartheta} < \overline{St_{n,0.95}} \\
 & \underline{St_{n,0.25}} \geq St_{n,\vartheta} \geq \overline{St_{n,0.75}}
 \end{aligned} \right\} \quad (23)$$

Critical values of statistics St_n for $F^*(St_n)=0,25$ and average values $M^*(St_n)$ for $N=25000$ realizations St_n and of some n are resulted in table 4.

Table 4

Bottom boundary $(\underline{St_n})$ and average $M^*(St_n)$ values of statistics St_n

N	n	St_n ($F^*(St_n)=0.25$)	$M^*(St_n)$	N	n	St_n ($F^*(St_n)=0.25$)	$M^*(St_n)$
1	2	-0.498	-0.33	9	22	-0.17	-0.047
2	3	-0.435	-0.254	10	29	-0.149	-0.037
3	4	-0.385	-0.207	11	40	-0.127	-0.027
4	5	-0.343	-0.173	12	60	-0.105	-0.019
5	6	-0.312	-0.146	13	90	-0.086	-0.012
6	7	-0.294	-0.133	14	120	-0.074	-0.00-
7	11	-0.235	-0.87	15	150	-0.067	-0.008
8	16	-0.198	-0.063				

The computer technology of an estimation of parameters of individual reliability assumes automation of process of classification of multivariate data. For what, as initial data boundary values of statistics St_n should entered. In this

connection, by analogy to formulas (8) and (9), the opportunity of an estimation of dependence of boundary values St_n from n was of interest.

The equations of regress received under the standard program of sedate transformation, are characterized by factor of determination R^2 : ($R^2 > 0.999$) and for of some $Sh1(St_n) = \alpha/2$ look like:

- for $Sh1(\overline{St_n}) = 0,025$ $\overline{St_n} = (1.23n^{0.52} - 1)/n = (B_1n^{0.52} - 1)/n$ (24)

and $Sh1(\underline{St_n}) = 0,975$ $\underline{St_n} = -1.23n^{-0.48} = -B_1/n^{0.48}$ (25)

- for $Sh1(\overline{St_n}) = 0,05$ $\overline{St_n} = (1.12n^{0.52} - 1)/n = (B_2n^{0.52} - 1)/n$ (26)

and $Sh1(\underline{St_n}) = 0,95$ $\underline{St_n} = -1.12n^{-0.48} = -B_2/n^{0.48}$ (27)

- for $Sh1(\overline{St_n}) = 0,1$ $\overline{St_n} = (0.98n^{0.52} - 1)/n = (B_3n^{0.52} - 1)/n$ (28)

and $Sh1(\underline{St_n}) = 0,9$ $\underline{St_n} = -0.98n^{-0.48} = -B_3/n^{0.48}$ (29)

- for $Sh1(\overline{St_n}) = 0,25$ $\overline{St_n} = (0.75n^{0.52} - 1)/n = (B_4n^{0.52} - 1)/n$ (30)

and $Sh1(\underline{St_n}) = 0,75$ $\underline{St_n} = -0.75n^{-0.48} = -B_4/n^{0.48}$ (31)

The equation of dependence of constant factors B from α with factor of determination R^2 : ($R^2 > 0.993$) looks like:

$$B = 0.652 \left[Sh1(\overline{St_n}) \right]^{-0.175} \quad (32)$$

Thus, the bottom and top boundary values of statistics St_n in view of the equation (12) calculated under following formulas:

$$\underline{St_n} = -0.652 \left[Sh1(\underline{St_n}) \right]^{-0.175} \cdot n^{-0.48}$$

$$\overline{St_n} = - \left[\underline{St_n} - \frac{1}{n} \right] \quad (33)$$

For practical calculations $\underline{St_n}$ and $\overline{St_n}$ more often formulas (27) and (12) used.

CONCLUSIONS

1. The interval nonparametric criterion of the control of conformity samples from n pseudo-random numbers is offered to the uniform law in an interval $[0,1]$;
2. In a basis of criterion there is a distinction of distributions of positive and negative values of the greatest divergence of distributions $F_\Sigma(\xi)$ and $F_V^*(\xi)$;
3. Transition from statistics D_n to statistics St_n allows not only to simplify algorithm of calculation greatest divergences $F_\Sigma(\xi)$ and $F_V^*(\xi)$, but also to

- estimate an opportunity of use of statistics St_n at an estimation of the greatest divergence s.f.d. $F_\Sigma^*(X)$ and $F_V^*(X)$, to estimate risk of the erroneous decision $Sh1(St_n)$;
4. Increase of accuracy of the control of conformity of distribution St_n^* to the uniform law reached by practical realization of recommended algorithm of the decision-making considering not only a errors I type, but also the errors II type.

[1] *E.M. Farhadzadeh, A.Z. Muradaliyev, Y.Z. Farzaliyev.* Quantitative estimation of individual reliability of the equipment and devices of the power supply system. Journal: «Reliability: Theory&applications. R&RATA (Vol.7 No.4 (27)) 2012, December., USA, p.53-62.

[2] *B.V. Gnedenko, J.K. Beljaev, A.D.Solovyov.* Mathematical methods in the theory of reliability. "Science", 1965, 524 p.

[3] *B. Kelton, A. Law.* Imitational modeling. Classics CS. 3 CP6.: Peter, Kiev: Publishing group BHV, 2004, 847 p.

[4] *I.A. Ryabinin.* The heart of the theory and calculation of reliability of ship electro power systems. Shipbuilding. 1971, 454 p.

[5] *E.M. Farhadzadeh.* Technique of a statistical estimation of critical values of empirical distribution from theoretical. «Methodical questions of research of reliability of greater systems of power» SEI SO SA USSR, 16, Grozny, 1978, p.39-49.

Received: 15.03.2013

THE NONEQUILIBRIUM RADIATIVE STATES IN EXTERNAL CONSTANT AND ALTERNATING MAGNETIC FIELDS

E.R. HASANOV

BDU. Physical problem Institute

B.Z. ALIYEV

Technology University, Gendja

The energy radiation theory in constant and alternating magnetic fields of conducting mediums with one type current carrier is constructed. The analytic expression for radiation expression is obtained. The substance and impedance imaginary part are calculated. The change intervals of electric and magnetic fields are defined. The impedance plot in radiation conditions is constructed.

Keywords: instability, impedance frequency

PACS: 76.60.Jx

The investigation of kinetic properties of conducting mediums with theory and practice point of view is very interesting. The metals, semi-metals and semi-conductors and their mixtures are the bases of practice device, amplifiers, generators and etc preparation. The main interest presents the application and multi-valley semiconductors on the base of which Gann generators are prepared. These devices work in frequency interval $10^7 \div 10^{11}$ Hz and are well used in cosmic engineering. At frequencies $10^7 \div 10^{11}$ Hz the total current in GaAs oscillates and electric charges distribute in heterogeneous form. The nonhomogeneous charge distribution leads to dependences mobility and concentrations on electric field. The drift velocity $v_n(E)$ and carrier concentration $n(E)$ on electric field depend on nonlinear form.

Because of $v(E)$ and $n(E)$ nonlinearity the theoretic investigation is difficult. The radiations take place with very high frequency and the sample is in nonequilibrium state. This state is unstable. The theory of nonequilibrium states requires practically clear approximations [1]. The electric current amplitude complexly depends on time. By this reason the equations describing the unstable states are nonlinear ones [2]. When current oscillations begin, the sample divides on different parts with electric field different values. These parts (domains) appear and disappear with frequency $10^7 \div 10^{11}$ Hz. The dimensions of these domains are less than sample dimension. Inside the sample the domain

motion velocities are $v < v_d$, $v = v_d$, $v > v_d$. The unstable sample states strongly depend on type. If only the conduction forms by electrons, radiation frequency strongly differs from radiation frequency at presence of both carrier types (electrons and holes). Inside the sample the wave can appear in one point (absolute) or distributes (convection) along the sample [3].

If appearing wave goes out (i.e. current oscillations take place), then crystal impedance becomes complex one. Gann's effect takes place because of sample resistance decrease. The impedance calculations at radiation state leads to theoretical study of unstable states. At impedance calculations one can take into consideration the electric field value on sample boundaries (boundary conditions). The current oscillations at the presence of both type current carries are theoretically studied in [1]. In given theoretical paper we will construct the oscillation current theory in the sample with one type carrier at the presence of constant external electric field E_0 and alternating magnetic field H_0 . We obtain intervals of external electric and magnetic field variation by impedance calculation. In the given theoretical work we will use the approximations which are satisfied in different experiments and also the new experiment conditions will be discussed.

The current density with one carrier type in external electric field E_0 and magnetic field has the form.

$$\vec{j} = \frac{\epsilon}{4\pi} \frac{\partial \vec{E}_1}{\partial t} + \sigma \vec{E} + \sigma_1 \left[\begin{matrix} \vec{E} \\ \vec{H} \end{matrix} \right] + \sigma_2 \vec{H} \left(\begin{matrix} \vec{E} \\ \vec{H} \end{matrix} \right) + D \nabla \rho - D_1 \left[\nabla \vec{\rho} \vec{H} \right] + D_2 \vec{H} \left(\nabla \vec{\rho} \vec{H} \right) \quad (1)$$

Here $\sigma = en\mu$ is ohmic conductivity, $\sigma_1 = en\mu_1$ is Hall conductivity, $\sigma_2 = en\mu_2$ focusing conductivity, D, D_1, D_2 are corresponding diffusion coefficients, $\rho = en$ is charge carrier density.

The connection of electric and magnetic fields and also electric field with charge density has the following form:

$$\frac{\partial \vec{H}}{\partial t} = -c \text{rot } \vec{E}; \quad \text{div } \vec{E} = \frac{4\pi}{\epsilon} \rho \quad (2)$$

(C is spreading rate of electromagnetic field in vacuum, ϵ — is dielectric constant).

The equations (1-2) under following conditions

$$\vec{E} = \vec{E}_0 + \vec{E}'; \quad \vec{H} = \vec{H}_0 + \vec{H}'; \quad \rho = \rho_0 + \rho', \quad \left(\vec{E}', \vec{H}', \rho' \right) \sim e^{i(\vec{k} \vec{r} - \omega t)} \quad (3)$$

for current density have the form:

$$\begin{aligned} \vec{j}' = & \frac{\varepsilon}{4\pi} \frac{\partial \vec{E}'}{\partial t} + \sigma_0 \vec{E}' + \left(\frac{\varepsilon}{4\pi} \mu_0 \text{div} \vec{E}' + \rho_0 \mu_0 \varphi_\mu \frac{\vec{E}_0 \vec{E}'}{E_0^2} \right) \vec{E}_0 + i \frac{c\sigma_{10}}{\omega} \left[\vec{E}_0 \text{rot} \vec{E}' \right] - \\ & - \sigma_{10} \left[\vec{E}' \vec{H}_0 \right] - \left(\frac{\varepsilon}{4\pi} \mu_{10} \text{div} \vec{E}' + \rho_0 \mu_{10} \varphi_{\mu 1} \frac{\vec{E}_0 \vec{E}'}{E_0^2} \right) \left[\vec{E}_0 \vec{H}_0 \right] - \frac{ic\sigma_2^0}{\omega} \text{rot} \vec{E}' \left(\vec{E}_0 \vec{H}_0 \right) + \\ & + \sigma_2^0 \vec{H}_0 \left(\vec{E}' \vec{H}_0 \right) - \frac{ic\sigma_2^0}{\omega} \vec{H}_0 \left(\vec{E}_0 \text{rot} \vec{E}' \right) + \left(\frac{\varepsilon}{4\pi} \mu_{20} \text{div} \vec{E}' + \rho_0 \mu_{20} \varphi_{\mu 2} \frac{\vec{E}_0 \vec{E}'}{E_0^2} \right) \vec{H}_0 \times \\ & \times \left(\vec{E}_0 \vec{H}_0 \right) + \frac{\varepsilon D}{4\pi} \text{graddiv} \vec{E}' - \frac{\varepsilon D_1}{4\pi} \left[\text{graddiv} \dots \vec{E}' \vec{H}_0 \right] + \frac{\varepsilon}{4\pi} D_2 \vec{H}_0 \left(\text{graddiv} \vec{E}' \vec{H}_0 \right) \\ \varphi_\mu = & \frac{d \ln \mu}{d \ln E_0^2}; \quad \varphi_{\mu_1} = \frac{d \ln \mu_1}{d \ln E_0^2}; \quad \varphi_{\mu_2} = \frac{d \ln \mu_2}{d \ln E_0^2} \quad (4) \end{aligned}$$

From vector equation (4) it is seen that for definition of current density components j'_x, j'_y, j'_z one should direct the external electric field \vec{E}_0 , and magnetic one \vec{H}_0 on concrete coordinates. Let's choose the concrete direction:
 $\vec{E}_0 = \vec{i} E_{0x} + \vec{i} E_0, \quad \vec{H}_0 = \vec{k} H_{0z} = \vec{k} H_0, \quad (\vec{i} \text{ is unit vector by } x, \vec{k} \text{ is unit vector by } z).$

Then current density components have the following form:

$$\begin{aligned} j'_x = & -\frac{i\omega\varepsilon}{4\pi} E'_x + \sigma_0 E'_x + \left(\frac{\varepsilon}{4\pi} \mu_0 \text{div} \vec{E}' + \rho_0 \mu_0 \varphi_\mu \frac{E'_x}{E_0} \right) E_0 + \sigma_{10} H_0 E'_y + \frac{\varepsilon D}{4\pi} \times \\ & \times \left(\frac{\partial^2 E'_x}{\partial x^2} + \frac{\partial^2 E'_y}{\partial x \partial y} + \frac{\partial^2 E'_z}{\partial x \partial z} \right) - \frac{\varepsilon D_1}{4\pi} H_0 \left(\frac{\partial^2 E'_x}{\partial x \partial y} + \frac{\partial^2 E'_y}{\partial y^2} + \frac{\partial^2 E'_z}{\partial y \partial z} \right) \\ j'_y = & -\frac{i\omega\varepsilon}{4\pi} E'_y + \sigma_0 E'_y + \frac{ic\sigma_{10} E_0}{\omega} \left(\frac{\partial E'_z}{\partial x} - \frac{\partial E'_x}{\partial z} \right) + \sigma_{10} H_0 E'_x + \frac{\varepsilon D}{4\pi} \times \\ & \times \left(\frac{\partial^2 E'_x}{\partial x \partial y} + \frac{\partial^2 E'_y}{\partial y^2} + \frac{\partial^2 E'_z}{\partial y \partial z} \right) + \frac{\varepsilon D_1 H_0}{4\pi} \left(\frac{\partial^2 E'_x}{\partial x^2} + \frac{\partial^2 E'_y}{\partial x \partial y} + \frac{\partial^2 E'_z}{\partial x \partial z} \right) \\ j'_z = & -\frac{i\omega\varepsilon}{4\pi} E'_z + \sigma_0 E'_z + \frac{ic\sigma_{10} E_0}{\omega} \left(\frac{\partial E'_x}{\partial y} - \frac{\partial E'_y}{\partial x} \right) + \sigma_2^0 H_0^2 E'_z - \frac{ic\sigma_2^0 H_0 E_0}{\omega} \times \\ & \times \left(\frac{\partial E'_z}{\partial y} - \frac{\partial E'_y}{\partial z} \right) + \frac{\varepsilon D}{4\pi} \left(\frac{\partial^2 E'_x}{\partial x \partial z} + \frac{\partial^2 E'_y}{\partial y \partial z} + \frac{\partial^2 E'_z}{\partial z^2} \right) + \frac{\varepsilon D_2 H_0^2}{4\pi} \left(\frac{\partial^2 E'_x}{\partial x \partial z} + \frac{\partial^2 E'_y}{\partial y \partial z} + \frac{\partial^2 E'_z}{\partial z^2} \right) \quad (5) \end{aligned}$$

From (5) it is seen that current density values by directions x, y, z are different and by these directions the sample has the different resistance (impedance Z)

$$Z(x, y, z) = \frac{1}{\sigma_0 S} \iiint_0^{L(x,y,z)} E(x, y, z) dx dy dz \quad (6)$$

One must calculate the impedance by directions x, y, z . However, it is known that experiment observes the sample studies by one direction. Then impedance values by x have the form:

$$Z(x) = \frac{1}{\sigma S} \int_0^{L_x} E'(x) dx \quad (7)$$

(S is sample cross-section)

Let's define E'_y and E'_z values from $j'_y = 0, j'_z = 0$ condition and substituting j'_x , obtain $E'(x)$.

At calculation $Z(x)$ from (7) one can take into consideration that radiations by y and z ($j'_y = 0, j'_z = 0$) are absent. Then appearing waves inside the sample by y and z directions are stable ones and wave vectors of these waves are defined by following form:

$$K_y = \frac{2\pi}{L_y} m_y; \quad K_z = \frac{2\pi}{L_z} m_z$$

(L_y, L_z are corresponding lengths, $m_{y,z}=0, \pm 1, \pm 2, \dots$.)

Taking into consideration the above mentioned, we write:

$$E'(x) = A(x, t) e^{i(\vec{k} \vec{r} - \omega t)} \quad (8)$$

Taking into consideration (8) we obtain:

$$j'_x = -\frac{\varepsilon D}{4\pi} \left(1 + i \frac{4\pi\sigma_0\alpha}{ck_x} \right) \frac{\partial^2 E'_x}{\partial x^2} + \frac{\varepsilon \omega_0}{4\pi} \left(1 + i \frac{3}{2} \frac{\sigma_0 D \alpha^2}{\nu_0 c} \right) \frac{\partial E'_x}{\partial x} - \sigma_0 \left[\frac{\alpha \sigma_0}{k_x \nu_0} + i \left(\frac{2\pi}{\varepsilon} \right)^2 \frac{\sigma_0^2}{k_x^2 \nu_0 c} \cdot \frac{2}{\alpha} \right] E'_x \quad (9)$$

$$\text{Here } \sigma_0 = \varepsilon n_0 \mu_0; \quad \alpha = \frac{\mu H}{c} \gg 1, \nu_0 = \mu_0 E_0; \quad \omega = \frac{4\pi}{\varepsilon} \sigma_0 \quad (10)$$

The solutions of differential equation (9) we obtain in the following form:

$$E'(x) = c_1 e^{i\Gamma_1 x} + c_2 e^{i\Gamma_2 x} + c_0 \quad (11)$$

C_1, C_2 constants are defined from boundary conditions of electric field, C_0 is private solution of (9), Γ_1 and Γ_2 are roots of quadratic law of equation (9) at $j'_x = 0$.

At $j'_x = 0$ from (9) we obtain:

$$\Gamma_1 = \frac{\nu_0 N}{2D} + \left[\left(\frac{\nu_0 N}{2D} \right)^2 (1 - i2\delta - \delta^2) - \frac{\sigma_0 f}{D} (a - ib) \right]^{1/2}$$

$$\Gamma_2 = \frac{\nu_0 N}{2D} - \left[\left(\frac{\nu_0 N}{2D} \right)^2 (1 - i2\delta - \delta^2) - \frac{\sigma_0 f}{D} (a - ib) \right]^{1/2} \quad (12)$$

$$\text{Here } N = \left(\frac{ck_x}{4\pi\sigma_0\alpha} \right)^2; \quad \delta = \frac{4\pi\sigma_0\alpha}{ck_x}; \quad f = \frac{4\pi\sigma_0}{D} \left(\frac{ck_x}{4\pi\sigma_0\alpha} \right)^2$$

$$a = \frac{32\pi^3}{\varepsilon^2} \frac{\sigma_0^3}{k_x^2 v_0 k_x c^2}; b = 4\pi\alpha^2 \frac{\sigma_0^3}{k_x^2 v_0 k_x c^2};$$

For finding of C_1 and C_2 we will use the homogeneous condition for electric field on sample boundary.

$$E'(0) = E'(L_x) = 0 \quad (13)$$

$$C_1 = \frac{C_0(1 - e^{\alpha_2})}{e^{\alpha_2} - e^{\alpha_1}}; C_2 = \frac{C_0(e^{\alpha_1} - 1)}{e^{\alpha_2} - e^{\alpha_1}} \quad (14)$$

$$\alpha_1 = i\Gamma_1 L_x, \alpha_2 = i\Gamma_2 L_x$$

$$\Gamma_1 = \frac{v_0 N}{2D} + x + i\left(y - \frac{v_0 N \delta}{2D}\right); \Gamma_2 = \frac{v_0 N}{2D} - x - i\left(y + \frac{v_0 N \delta}{2D}\right)$$

Substituting (11) in (7) we obtain the expression for sample impedance

$$\frac{Z}{Z_0} = \Phi \left[1 + \frac{\Gamma_2 - \Gamma_1}{L_x \Gamma_1 \Gamma_2} \cdot \frac{(1 - e^{\alpha_2})(e^{\alpha_1} - 1)}{e^{\alpha_2} - e^{\alpha_1}} \right] \quad (15)$$

Here; $\Phi = c_0 \sigma_0$, $c_0 = \frac{1}{\sigma_0 \left[\frac{\alpha \sigma_0}{k_x v_0} \right] + i \left(\frac{2\pi}{\varepsilon} \right)^2 \cdot \frac{\sigma_0^2}{k_x^2 v_0 c} \cdot \frac{2}{\alpha}}$; $z_0 = \frac{L_x}{\sigma_0 S}$;

From (15) it is seen that sample impedance complexly depends on electric and magnetic fields. The simple algebraic calculations show that at $\frac{v_0 c}{D \sigma_0} \gg 4\pi\alpha$ (16) show that real and imaginary parts of impedance have the following form:

$$\frac{R_e Z}{Z_0} = -2l\Phi_0 y e^{2r\delta} \left(\cos 2r + \frac{a}{b} \sin 2r \right) - 2l e^{2r\delta} (\Phi_1 y + \Phi_0 x) \sin 2r + \Phi_0 (1 + 2ly) \quad (16)$$

$$\frac{Z_m Z}{Z_0} = -\Phi_1 (1 + 4ly) - 2l\Phi_0 e^{2r\delta} \sin 2r + 2l\Phi_0 \left(x + \frac{ay}{b} \right) e^{2r\delta} \cos 2r \quad (17)$$

$$r = \frac{v_0 N L_x}{2D}; l = \frac{D}{L_x \sigma_0 f b}$$

Here $\Phi_0 \gg \Phi_1$; $y > 0$, $x > 0$, $\Phi_1 > 0$

From expression (16) it is seen that at all positive values of trigonometric functions $\sin 2r$, $\cos 2r$ ($2r$ must change from zero up to π) the impedance real part has the negative sign and the sample will receive the energy. At $2r = \frac{\pi}{2}$ $\cos 2r = 0$ the impedance imaginary part also has the negative sign.

The changes of real and imaginary parts of the impedance are presented by following plot.

The figures 1 and 2 show that approximate oscillation motion of real and imaginary parts of impedance is presented by following plot:

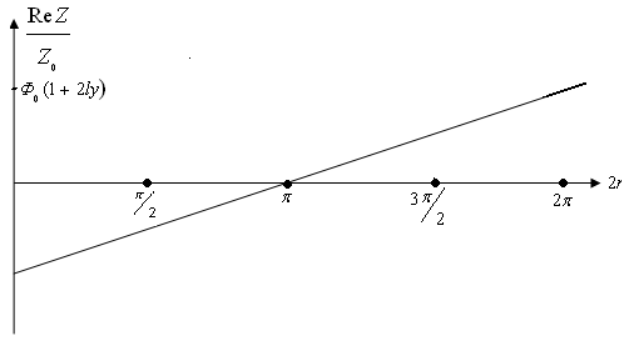


Fig.1

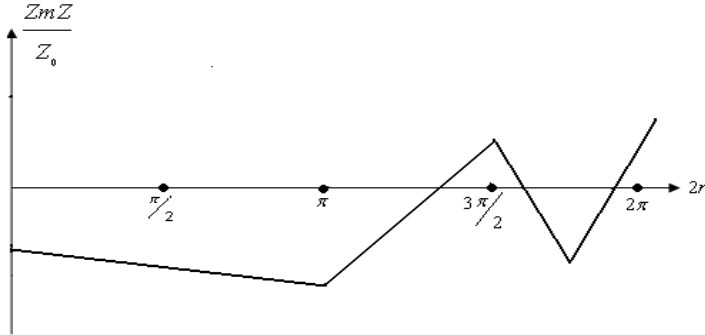


Fig.2

RESULTS

If the external electric and magnetic fields are perpendicular, $\vec{E}_0 \perp \vec{H}_0$ then the wave radiations of electromagnetic character take place in direction perpendicular to magnetic field with frequency

$$\omega = \frac{4\pi}{\epsilon} \sigma_0. \text{ This radiation takes place if the magnetic}$$

$$\text{field is } H \gg \frac{c}{\mu} \text{ and electric field is } E_0 \gg \frac{4\pi D \sigma_0}{c^2} H$$

If we take into consideration the diffusion coefficient values at high values of electric field

$$D = \frac{T}{3e} \mu_0 \left(\frac{SH}{cE_0} \right)^2 \text{ [4],}$$

then for the $\frac{E_0}{H_0}$ relation we obtain:

$$\frac{E_0}{H_0} \gg \left(\frac{4\pi n_0 T}{3} \right)^{1/2} \cdot \frac{\mu S}{c^2}$$

(n_0 is current equilibrium carrier concentration, S is sound wave velocity in the sample).

[1] L.E. Qurevich, E.R.Qasanov, FTP, 1201, 1969. (In Russian)
 [2] Bonch-Bruevich, FTT, 2, 356, 1966. (In Russian)
 [3] V.L. Bonch-Bruevich, I.P. Zvyagin, A.Q. Mironov. Domennaya elektricheskaya neystoychivost v poluprovodnikax, Izd.: Nauka, Moskva 1972, str.291-296. (In Russian)

[4] R.F. Kazarinov, V.Q. Skobov, JETF, 42, 1047, 1962. (In Russian)
 [5] E.R. Hasanov, R.K. Qasimov, A.Z. Panahov and A.I. Demirel, Adv. Studies Theor. Phys. vol.3, 2009, №8, 299-298.
 [6] A.I. Demirel, E.R. Hasanov, A.Z. Panahov, Adv. Studies Theor. Phys. vol.6, 2012, №22, 1077-1086.

Received:12.02.2013

PIEZOELECTRIC PROPERTIES OF POLYMER COMPOSITE DIELECTRICS

M.A. KURBANOV¹, A.A. BAYRAMOV², T.G. MAMMADOV¹, M.M. KULIEV³

¹*Institute of Physics Azerbaijan National Academy of Sciences*

²*Azerbaijan High Army College after Heydar Aliyev*

³*Institute of Radiation Problems Azerbaijan National Academy of Sciences*

Investigations results of ferroelectric particle basic structural parameters responsible for piezoelectric effect – formation in polymer compositions are presented in paper. Composite piezoelectric properties are found to be determined by polarization at polymer-ferroelectric interface. Piezofiller basic parameters and boundary polarization processes are determined which are responsible for large piezoelectric effect formation in composites.

Keywords: piezoelectric, polymer, polarization processes, composites.

PACS: 77.84.Lf

1. BACKGROUND

Physics of active dielectrics gave techniques principal new materials based on the semiconductive solid solutions for successful solution of many complex problems of radiotechniques, hydrolocation, optoelectronics, pyro- and piezotechniques. There are important polymers, dispersed or filled by various semiconductors and ferroelectric active solid solutions among of these materials: polymer-piezoelectric (composite) systems, in possession of high piezoelectric, electret and physic-mechanical properties.

There are many articles devoted to problems of technology obtaining piezoelectric composites [1-9]. But they mainly consider either only technological problems directed to revelation of possibility of the volume content increasing of piezocomponent or problems of correlation between conditions of obtaining such active dielectric materials and their main electro physical properties. And when choice of components of compositions it is take account of dielectric constant, piezoelectric coefficients of polymer matrix and piezoparticles. But up to now few investigations are devoted to establishing couplings both qualitative and quantitative between piezoelectric properties of composites and remanent reorientation polarization P_r , degree of non 180° domain reorientations in polarization process, number N possible directions of spontaneous polarization vector, volume conductivity of ferroelectric filler, and also supramolecular structure, electro physical characteristics of polymer matrix.

Preliminary investigations have shown that there is a noticeable divergence between piezoelectric characteristics of composites obtained by experimental and theoretical calculations [1]. The results of the investigation of main structure characteristics of ferroelectric particles responsible for forming of piezoelectric effect in polymer composite compositions are presented in paper.

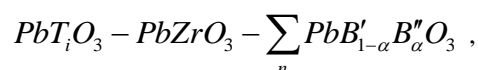
Next main tasks were been solved:

1. Investigations of structure change, thermo- and electrophysical properties of polar and nonpolar polymers, dispersed by ferroelectrics.
2. Investigations of polarization processes when there is thermoelectretting in forming piezoelectric effect in composites.

3. Investigations of dependence of the composite piezocoefficients (piezomodulus d_{ij} and piezosensitivity g_{ij}) on volume content (Φ) and parameter d_{ij}/ε of piezoparticles.

4. Investigations of contribution of remanent reorientation polarization P_r , number N possible directions of spontaneous polarization vector, degree of domain reorientations η and conductivity ferroparticles to forming high piezoelectric effect in composites.

Composite materials obtained based on the various polymer dielectrics and multicomponents materials are more effective, and possess high electret and piezoelectric properties in comparison with composition having fillers with double components of PZT. Under this a morphotropy region is important factor when choice fillers dividing system on regions of rhombohedral (P_e) and tetragonal (T) phases. So, used by us main piezoceramic materials are solid solutions of multicomponents system as



where $n = 2,3$, which in dependence on location relatively to a morphotropy region possess various symmetry, piezo- and pyroelectrics characteristics and dielectric properties. Materials with cipher PCR were developed in Institute of Physics Rostov State University using technology of hot pressing [8].

2. SAMPLE PREPARATION AND EXPERIMENTAL TECHNIQUE

The obtaining process of some composite, particularly polymer, include minimum 3 stages: 1) preparation and choice of initial components; 2) mixing of components; 3) obtaining composite material based on the mixture by extruding, chemical deposition or hot pressing. Choice components and obtaining method of composite material is defined by complex of properties which active composite must possess. It was based on the next principles: high flexibility, mechanical and electrical strength, and no porosity of composite. Namely these physic-mechanical properties of composite make theirs more actually and allow to develop transducers various size and configurations.

So, polymer matrix is laid claim to certain demands: light process, high plasticity and heightened dielectric constant. The analysis of physic-mechanical properties of polymer showed that thermoplastic polyolefines and fluorocarbon polymer: polyethylene, polypropylene (PP), polyvinylidene fluoride and copolymerphenylfluoride with tetrafluoroethylene meet these demands.

The measurement of piezoelectric modulus g_{ij} of composite was carried out in quasistatic regime. Charge state of composite was investigated by method of registration of spectrum of the thermostimulated depolarization current.

3. EXPERIMENTAL RESULTS

Below we consider change of piezoelectric and dielectric properties of compositions based on the polyolefines and ferroelectrics with various structures, piezomodulus and piezosensitivity in dependence on volume content (Φ) of filler, electric field intensity (E_n) and polarization temperature (T_n) [1-7].

The dependences of piezomodulus and piezosensitivity of compositions based of the polypropylene and 50% vol. of PKR-7M ferroceramics on electric field intensity and polarization temperature, respectively have been shown in fig. 1 and 2.

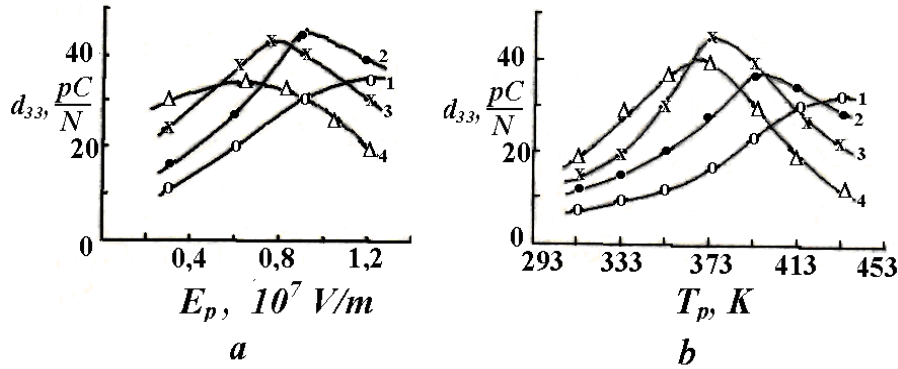


Fig.1. a) Dependence of $d_{33}=f(E_n)$ of PP+50% vol. PKR-7M composition: 1 - $T_p=373$ K; 2 - $T_p=393$ K; 3 - $T_p=413$ K; 4 - $T_p=433$ K.
b) Dependence of $d_{33}=f(T_n)$ of PP+50% vol. PKR-7M composition: 1 - $E_p=0,3 \cdot 10^7$ V/m; 2 - $E_p=0,6 \cdot 10^7$ V/m; 3 - $E_p=0,9 \cdot 10^7$ V/m; 4 - $E_p=1,2 \cdot 10^7$ V/m.

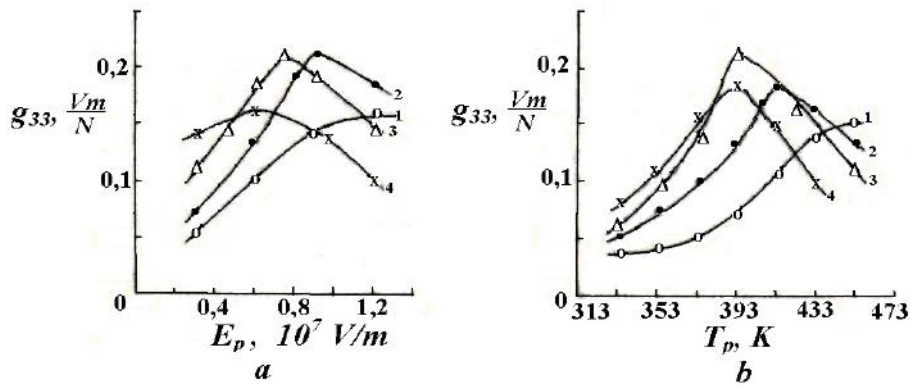


Fig. 2. a) Dependence of $g_{33}=f(E_n)$ of PP+50% vol. PKR-7M composition: 1 - $T_p=373$ K; 2 - $T_p=393$ K; 3 - $T_p=413$ K; 4 - $T_p=433$ K.
b) Dependence of $g_{33}=f(T_n)$ of PP+50% vol. PKR-7M composition: 1 - $E_p=0,3 \cdot 10^7$ V/m; 2 - $E_p=0,6 \cdot 10^7$ V/m; 3 - $E_p=0,9 \cdot 10^7$ V/m; 4 - $E_p=1,2 \cdot 10^7$ V/m.

The distinctive peculiarity of PKR-7M ferroceramics is a very high dielectric constant ($\epsilon = 5000$), coefficients of electromechanical coupling and piezomodulus. It was obtained by modification of ferrosoft PKR-7M ferroceramics, has tetragonal structure and possesses piezomodulus of $d_{33}=760$ pC/N. But PKR-7M has heightened dielectric and mechanic losses. From figures for d_{33} and g_{33} dependences on E_n at all T_n for PP+PKR-7M compositions we can see curves with maximums. The values of E_n at which d_{33} and g_{33} of compositions reach a maximum depend on temperature of polarization. With increasing T_n the field intensity with

maximums of d_{33} and g_{33} decreases. Also, dependences of $d_{33}=f(T_n)$ and $g_{33}=f(T_n)$ of compositions have extreme character and maximums of these dependences shift to low temperature with increasing of E_n .

PKR-12, PKR-8 and PKR-25 piezoceramic are ferroelectric rigid piezomaterials with tetragonal structure and their ferroelectric rigid property increases with decreasing of dielectric constant [1]. These materials have relatively low piezomodulus, dielectric and mechanic losses in comparison with PKR-7M.

PKR-26 piezoceramic is located for from morphotropy region in tetragonal phase and has a high

Curie temperature and enough high piezoelectric parameters at low dielectric constant. Investigation results of piezoelectric properties of composites based on the polypropylene dispersed by PKR-7M, PKR-12, PKR-8 and PKR-26 piezoceramic in dependence on polarization temperature at $E_n = \text{const}$ and on electric field intensive at $T_n = \text{const}$ have shown that for equal conditions of polarization we don't watch a direct proportionality

between $(d_{33}^k, \frac{d_{33}^k}{\epsilon_k})$ parameters of ferroparticles and

piezoelectric properties of composites. Among mentioned composites PP+PKR-8 composition is more effectively. At the same time though a piezosensitivity of PKR-12 and PKR-26 is more in about 2 times than analogous parameter of PKR-7M ceramic, the piezocomposites based on theirs have practically equal piezomodulus. Analogous results had obtained in case using low density polyethylene and high density polyethylene as polymer matrix.

Dependences of d_{33} and g_{33} on Φ for PP+PKR-7M compositions polarized at optimal E_p and T_p are presented on fig. 3. We can see that the regularities of changes of $d_{33} = f(\Phi)$ and $g_{33} = f(\Phi)$ dependences are differed because the degree of change of composition dielectric constant in dependence on Φ , E_n and T_n is differed from the degree of Φ change on analogous arguments as piezosensitivity is determined

$$\text{as } g_{33} = \frac{d_{33}}{\epsilon_0 \epsilon_{kom}}$$

$$d_{33} = \Phi \frac{3\epsilon_p}{2\epsilon_p + \epsilon_k + \Phi(\epsilon_p - \epsilon_k)} \cdot \frac{5C_k \cdot d_{33}^k}{3C_p + 2C_k - 3\Phi(C_p - C_k)} \quad (1)$$

where ϵ_p and ϵ_k are dielectric constants of polymer matrix and ferroelectric filler, C_p and C_k are modules of elasticity of matrix and filler, d_{33}^k is a piezomodulus of ferroelectric filler. Taking into account $\epsilon_k \gg \epsilon_p$ and $C_k \gg C_p$ from (1) we have

$$d_{33} = \frac{15\Phi}{(1-\Phi)(2-3\Phi)} \cdot \frac{\epsilon_p}{\epsilon_k} \cdot d_{33}^k \quad (2)$$

We can see that piezomodulus of composition is proportional to dielectric constant of polymer matrix and piezosensitivity ($\frac{d_{33}^k}{\epsilon_k}$) of ferroelectric. With increasing Φ

the piezomodulus of composite must increase. So, when dielectric constant of polymer matrix and volume content of ferroparticles are constant then piezomodulus of composite must whole determined by $\frac{d_{33}^k}{\epsilon_k}$ that is a value

of polarization reorientation in ferroelectric and their dependence on mechanic disturbance. But numerous experiments showed that when $\epsilon_p = \text{const}$ there aren't

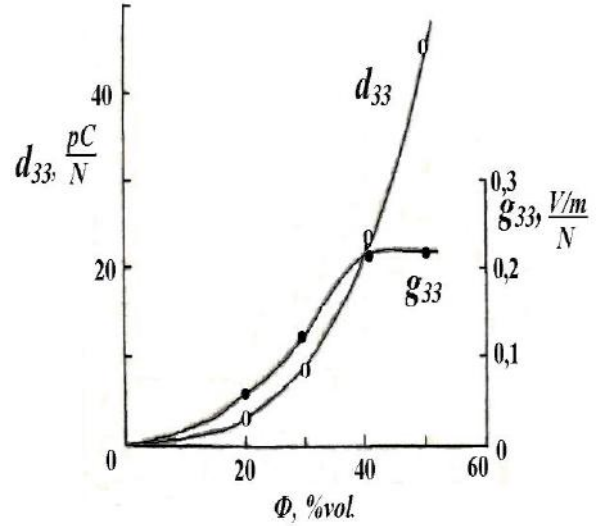


Fig.3. Dependence of d_{33} and g_{33} on Φ of PP+PKR-7M composition. $T_p = 393\text{K}$ и $E_p = 0,9 \cdot 10^7 \text{ V/m}$

4. DISCUSSION

Theoretical consideration of double phase system based on the polymer dielectric dispersed by statistic uniform distributed spherical particles on volume had shown [14] that d_{33} of composition increases by linear with increasing a volume content of ferroelectric in accordance to dielectric constant and piezomodulus of component, that is

direct proportional between d_{33}^k and $\frac{d_{33}^k}{\epsilon_k}$ of ferroelectric and piezomodulus of composite.

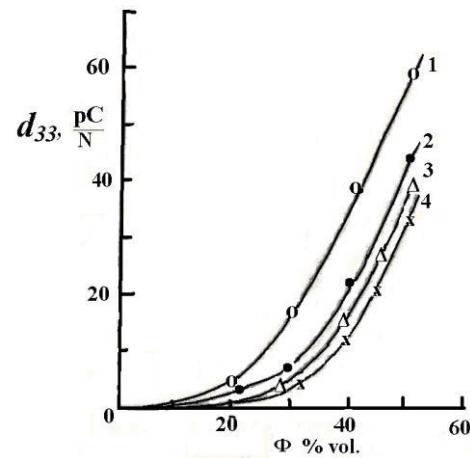


Fig.4. Dependence $d_{33} = f(\Phi)$ for compositions: 1 - PP+PKR-8; 2 - PP+PKR-7M; 3 - PP+PKR-12; 4 - PP+PKR-26 $T_n = 393\text{K}$ and $E_n = 9 \text{ MV/m}$.

The changes of d_{33}^k in dependence on volume content of ferroelectric are presented in fig. 4 for composites based on the PP dispersed by ferroelectric of tetragonal structure with various $\frac{d_{33}^k}{\varepsilon_k}$, for example PKR-7M, PKR-12, PKR-8 and PKR-26.

Piezoceramic PKR-8 and PKR-12 have the most piezosensitivity ($g_{33} \approx 23,5 \cdot 10^{-3} \text{ V}\cdot\text{m/N}$) among selected ferroelectric fillers of tetragonal structures [1]. But when $\varepsilon_p = \text{const}$ piezomodulus of composite in dependence on Φ doesn't change always proportional to $\frac{d_{33}^k}{\varepsilon_k}$ coefficient. If

compare piezoelectric coefficients of composites based on the PKR-7M, PKR-8 and PKR-12 then we can see that d_{33} of composites based on the PKR-26, PKR-7M and PKR-12 are approximately equal and is more for PKR-8

although piezosensitivity of PKR-7M is practically less in 2 times than analogous parameter for PKR-26 and PKR-12.

5. CONCLUSION

So, there have been presented the investigation results of ferroelectric particle basic structural parameters responsible for piezoelectric effect – formation in polymer compositions. Composite piezoelectric properties are found to be determined by polarization at polymer-ferroelectric interface. Piezofiller basic parameters and boundary polarization processes are determined which are responsible for large piezoelectric effect formation in composites. When development of high effectively

composite we should not take into account only $\frac{d_{33}^k}{\varepsilon_k}$.

-
- [1] *M.K. Kerimov, M.A. Kurbanov, A.A. Bayramov, A.I. Mamedov.* Matrix Active Micro- and Nanocomposites Based on the Polymer, Semiconductive and Ferropiezoceramic Materials. Nanocomposites and Polymers with Analytical Methods / Book 3. Book edited by: John Cuppoletti, 2011, INTECH Open Access Publisher. ISBN 979-953-307-136-6, pp.375-404.
- [2] *M.A. Kurbanov, A.A. Bayramov.* Electret composites polymer-piezoelectric with deep trapping centers on the interphase boundary. Scientific Israel- Technological Advantages Vol.14, no 3, 2012, pp.73-79.
- [3] *Ch.O. Gajar, M.A. Kurbanov, A.A. Bayramov, I.S. Sultanahmedova, F.N. Tatardar, O.A. Aliev, F.F. Yaxyayev, Z.A. Dadashev.* Hybrid piezoelectric materials based on the matrix nano- and microcomposites. Abstracts Book of Joint ISFD-11th-RCBJSF Symposium on Ferroic Domains and Micro- to Nanoscopic Structures, 2012, Ekaterinburg!, Russia, P-079, p.183.
- [4] *M.K. Kerimov, M.A. Kurbanov, A.A. Bayramov, I.S. Sultanahmedova, G. Guliyeva, B. Xudoyarov, K.K. Azizova, U.V. Yusubova.* Electret composite materials based on the polymer and ferro-piezoelectric with high reorientation polarization. Abstracts Book of Joint ISFD-11th-RCBJSF Symposium on Ferroic Domains and Micro- to Nanoscopic Structures, 2012, Ekaterinburg!, Russia, P-011, p.116
- [5] *M.A. Kurbanov, A.A. Bayramov, N.A. Safarov, F.N. Tatardar, I.S. Sultanahmedova.* Hybrid piezoelectric composites with high electromechanical characteristics. Scientific Israel- Technological Advantages Vol.14, no 1, 2012, pp.1-6.
- [6] *M.A. Kurbanov, A.A. Bayramov, N.A. Safarov, F.N. Tatardar, A.A. Mextili, I.S. Sultanahmedova.* Hybrid piezoelectric composites with high electromechanical characteristics. Patent US 8030829; 10/04/2011
- [7] *M.A. Kurbanov, A.A. Bayramov, N.A. Safarov, I.S. Sultanahmedova, S.N. Musaeva.* Electret composites polymer-piezoelectric with deep trapping centers on the interphase boundary. Patent US 8187488; 29/05/2012
- [8] *E.G. Fesenko, A.Ya. Danziger, O.N. Razumovskaya.* New piezoceramic materials. Rostov State University, 1988, 154 p.
- [9] *T. Furokawa et al.* Piezoelectric properties in composite system of polymer and PZT-ceramics. –J. Appl. Phys., 1979, v.50, №7, pp.4904-4912.

Received: 14.03.2013

ELECTROPHYSICAL PROPERTIES OF PHOTODIODE ON THE BASE OF IRIDIUM-SILICON SILICIDE

E.A. KERIMOV

Space Research of Natural Resources Institute

National Aerospace Agency

AZ 1106, S.S.Achundov st. 1.

One can achieve the additional information about transfer mechanism of charge carriers by the photoelectric measurements. The investigations of photoelectric properties of IrSi - n - Si and IrSi - p - Si structures are carried by us in the present paper. The two device types are used for these photoelectric measurements. At first case the planar ohmic layer has the total form and the diffusion - barrier layer has the ring one.

Keywords: Schottky diodes, potential barrier, iridium silicide, ohmic contact, photodetector, potential well.

PACS: 73.40.Ns, 73.40.Sx, 78.20.-e

The use of multielement receivers of radiation in IR-systems especially in the systems without optico-mechanical scanning requires the presence of high homogeneity of the sensitivity of receiving element in matrix so in opposite case the geometric noise strongly increases. The geometric noise of multielement matrixes can be eliminated in receiving apparatus of two standard radiating surfaces with high and low levels of radiation with following digital signal processing of each receiving element by special algorithm. The etching method not requiring the mask or additional photoresist is used at preparing of structures with Schottky barrier on IrSi - Si base. The transversal structure section is based on fig.1.

At lightening of such structure the photo-current appears in only that case if the polarity of applied voltage corresponds to positive potential on low non-transparent aluminum electrode.

At reversal voltage polarity the photo-current insignificantly increases in the comparison with dark current, however, this current change is in the limits of experiment error.

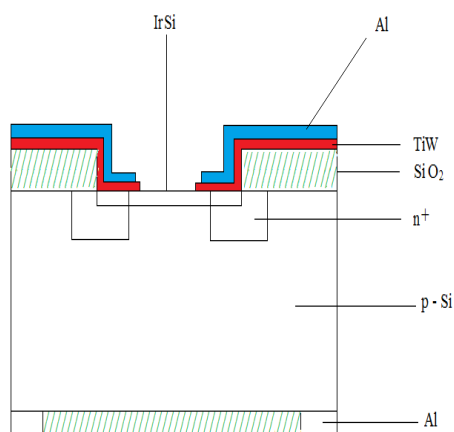


Fig.1. The transversal section of structures with Schottky barrier on IrSi - Si barrier.

This circumstance show on the fact that the observable photo-current is connected not with volume photo-conductivity of semiconductor plane and with

photo-electric phenomena on contacts: photoemission from metallic electrode in silicon substrate.

The current sensitivity for IrSi - n - Si structures in maximum achieves 43mA/Vt on wave length $\lambda = 0,62\mu\text{m}$ at room temperature. The low photo-sensitivity is connected with the fact that at thickness 100 Å IrSi has the absorption maximum. The radiation receivers on the base of IrSi - n - Si structures by the form of spectral characteristic from p-n photo-diodes differ by the fact that they have the wider spectral range. VAC structures IrSi - p - Si in the absence and at the presence of incident radiation are presented on fig.2.

As it is seen the significant current change through the investigated structures at the lightening is observed. The current through the investigated structures at lightening increases in 150-250 times at small values of applied reversal voltage (0,2-0,8V), in 300-350 times at more higher reversal shifting (1-2V), at voltage 6-8V the current change is almost 10^3 times, i.e. the more optimal mode of working of the structures with SchB (Schottky barrier) on IrSi - p - Si base is in the range $U_R = 6 - 8 \text{ V}$. At high voltages the leakages increase and also the breakdown of the investigated samples takes place. (The spectrophotometer ИКС - 14А constructed on wave length $\lambda = 8 \mu\text{m}$ is used in the capacity of light source and the light shines on IrSi from Si side).

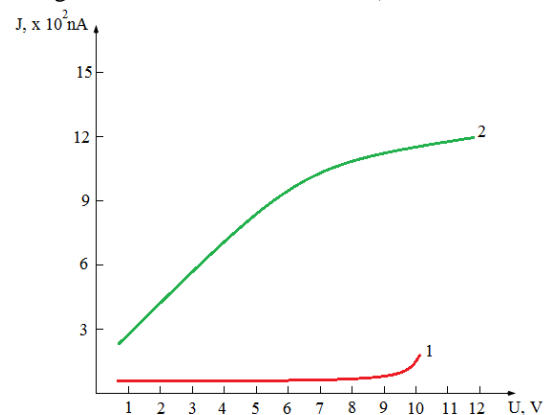


Fig.2. The reversal VAC IrSi - p - Si (in the absence - 1, at lightening - 2) at 80K.

The current for the structures with total planar ohmic contact through structures significantly lower changes at the lightening than in the structure with ring contact. Probably it is connected with the fact that in the case of total contact the photogenerated holes are recombined by metal electrons and don't achieve from one interface to another.

The spectral sensitivity distribution of IrSi – p - Si structure at 80K is presented on fig.3. The spectral sensitivity region totally overlaps the spectral window 8-14μm. The spectral dependence of quantum yield of SchD (Schottky diodes) inner photoemission is described by the formulae:

$$Y = C_1(h\nu - \varphi_B)^2 / h\nu$$

where φ_B is barrier height for holes, C_1 is quantum emission coefficient which depends on geometric, optical and physical properties of Schottky contact.

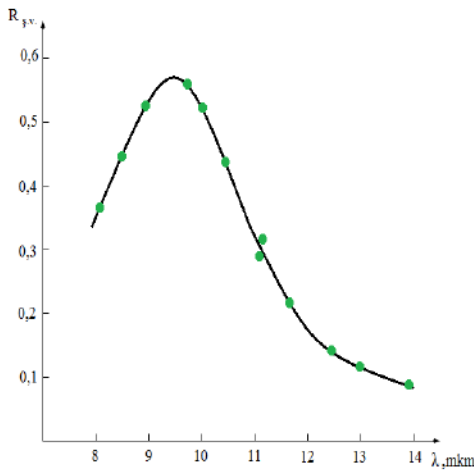


Fig. 3. The spectral characteristics of IrSi – p – Si at 80K.

For IrSi – p - Si structures the photoresponse monotonously increases with energy increase of IR-radiation. The photo-diode photosensitivity mechanism on the base of IrSi – Si contact isn't studied enough, the models in literature are opposite to each other. The spectral sensitivity is defined by the transition process physics through the barrier but not photoabsorption processes. In [1,2] it is shown that electron photoexcitation in metal (IrSi) creates the empty states (holes) some of which have the energy less than barrier one. Later either the hole emits from metal in the semiconductor or electron passes the barrier from the semiconductor in order to fill the empty states. Note that the supposed mechanism has the disadvantages, i.e. because of IR-radiation electrons in semiconductor don't have the additional energy and that's why they can't pass the barrier. From the other hand it is known that Schottky photo-diodes work on charge main carriers. It is supposed that the photo-excited electrons pass on higher energy levels at lightening of structures with Schottky barrier on the base of IrSi – Si contact. Moreover, electrons in IrSi pass on higher levels with $h\nu$ energy increase. Correspondingly the energy of forming holes changes.

The holes with energy which is bigger than barrier height of IrSi - Si contact will pass in semiconductor. With $h\nu$ increase or decrease of light wave length the increment of hole number increases. This leads to photo-current formation, i.e. for p-Si the holes are the main carriers.

The quantum photo-emission coefficient value C_1 for structures with ring and planar contact, obtained from the inclination dependence

$$\sqrt{Y \cdot h\nu} = \sqrt{C_1} (h\nu - \varphi)$$

is equal to 0,126 и 0,048 eV⁻¹. The dependence of C_1 coefficient is very sensitive to IrSi thickness. The simplified one-dimension model for photo-response PhDSchB (photo-diode with Schottky barrier) with dielectric film is supposed for explanation of experimental results. This model supposes the ideal reflection of the holes on silicide-isolator and silicide-semiconductor boundaries besides the holes emitting in silicon. One should take under consideration the many hole reflections on IrSi - Si и IrSi – isolator boundary for photo-detector with ring contact. In this case it is comfortable to introduce the new factor W_i is probability of the fact that hot hole from one interface is the function of average hole free length and silicide thickness:

$$W_i = \exp(-d / l)$$

Then the improvement factor Y presents itself the photo-response relation and is expressed by the following factor:

$$Y = Y_1 / Y_2 = 1 / [1 - \exp(-d / l)]$$

where at $d = 100 \text{ \AA}$ and $Y = 5$ the free length of hot holes are equal to 460 \AA . The last ones are prepared by the way of chemical reaction with silicide formation having the metallic conductivity for exclusion of surface state influence on potential barrier height φ_B and on photoelectric properties of IR-radiation receivers on Schottky diodes. In this case Schottky barrier appears on interface silicon-metal silicide. The absence of the influence on barrier properties of surface defects, oxides and pollutions on silicon surface is its advantage. One can supply such barrier height which defines the sensitivity in required range of IR-spectrum by the way of necessary material selection.

The radiation absorption degree in photo-sensitive structure IrSi – Si depends also on IrSi thickness and dielectric. The absorption maximum is observed at IrSi thickness near 90 \AA achieving the value $0,30 \pm 0,05 \%$; at thickness SiO_2 $0,75 \text{ \mu m}$ ($\lambda = 4,2 \text{ \mu m}$). At structure lightening the photo-current appears only in that case if applied voltage polarity corresponds to negative potential on IrSi. The observable photocurrent is connected not with volume photo-conductivity of semiconductor plane but with photoelectric phenomena on contact, i.e. with photo-emission from metallic electrode in silicon substrate.

The simplified one-dimension model for PhD photo-response with dielectric film is supposed for explanation

of experimental results. . This model supposes the ideal reflection of the holes on silicide-isolator and silicide-semiconductor boundaries besides the holes emitting in silicon and ideal passing the silicide-metal boundary. . One should take under consideration the many hole reflections on IrSi - Si и IrSi – isolator boundary for photo-detector with ring contact. In this case it is comfortable to introduce the new factor W_i is probability of the fact that hot hole from one interface is the function of average hole free length and silicide thickness:

$$W_i = \exp\left(-\frac{d}{l}\right)$$

Then the improvement factor $\gamma, (\gamma = \frac{Y_1}{Y_2})$ presents itself the photo-response relation and is expressed by the following factor:

$$\gamma = \frac{Y_1}{Y_2} = \frac{1}{\left[1 - \exp\left(-\frac{d}{l}\right)\right]}$$

where at $d = 90 \text{ \AA}$ and $Y = 5$ the free length of hot holes are equal to $450 \text{ \AA} \sim 45 \text{ nm}$.

[1] *Kukovecz, Z. Konya, I. Kiricsi.* Single wall carbon nanotubes, In. Encyclopedia of nanoscience and nanotechnology, Edited by H.S.Nalwa. Amer., Sci., Publ., 2004, Vol. 9, P. 923-946.

[2] *E. Gmaly.* Single-walled carbon NT formation with a continuous CO₂-laser: experiments and theory, Appl. Phys., 2000, A, 70, P. 161.

Received:07.03.2013

CHARACTERIZATION OF LYOTROPIC LIQUID CRYSTALLINE PHASES FORMED IN SODIUM DODECYL SULPHATE/OCTANOL/WATER TERNARY LYOTROPIC SYSTEM

EMIR HALIKI¹, OZGUR MASALCI¹ AND NADIDE KAZANCI¹

¹*Department of Physics, Faculty of Science, Ege University, İzmir, 35100, Turkey*
E-mail: omasalci@gmail.com, Tel.: +90 (232) 3115439, Fax: +90 (232) 3881036

Phase states in system of sodium dodecyl sulphate (SDDS) + octanol + water lyotropic liquid crystal have been investigated at constant temperature. First binary and then ternary systems have been studied. The phase diagram of the binary and ternary lyotropic systems have been determined by polarizing microscopy. Addition of octanol as a third component to the SDDS+water lyotropic system has contributed to the essential expansion of the lyotropic mesomorphism.

The correlation between phase states and physical properties (such as surface tension) in the binary system has been established. The results on the phase states of the system investigated by both optical microscopy and surface tension have been found to be consistent with each other.

Keywords: liquid crystal, surface tension, nematic, lyotropic, phase transition

PACS: 47.53.+n; 61.30; 64.70

1. INTRODUCTION

Surfactant mixtures are common in biological systems. Interaction of surfactants with water has been extensively studied considering their widespread uses in industry. Because of their characteristic physicochemical properties in a variety of different possible combinations, the mixed systems are of great interest [1]. Since the discovery of liquid crystals (LCs), investigations and studies on that mesophase or the fourth state of matter has attracted attention of many scientists from a variety of fields of research [2]. With large range of applications, LCs are significant objects of the condensed matter physics and chemistry [3]. LCs are fluid systems with an orientational order but without any positional order. In two types namely thermotropic and lyotropic, LCs are the mesophases between isotropic liquid and anisotropic solid forms of matter. Showing liquid crystal properties, thermotropics depend on temperature primarily and on pressure secondarily. Unlike thermotropics, the lyotropic liquid crystals are based on the relative concentration of the solutes solved in the solvent consisting of long amphiphilic molecules [2–7] which can be absorbed through surface.

In aqueous solutions, amphiphilic molecules occur in a wide variety of structures and phases [8,9]. Due to their compositions, the system organizes into various lyotropic phases as the concentration of amphiphilic molecules is increased, becoming ordered over long distances and forming distinct lyotropic liquid crystal phases [10,11].

A temperature–composition phase diagram is fundamental and useful data to investigate the mixture systems since it predicts the phases of the mixture as a function of temperature and composition [12]. Adding second alkyl chain (alcohol) to the aqueous system, with the other factors being constant, we can easily understand that structure of other geometries may become favoured. While correlation of chemical structure with aggregate structure is much more complex, it can be an illustrative and useful starting point, in particular in analysing trends in phase behaviour. Basically, the formed structure is the

result of the equilibrium between the polar and non-polar parts of a amphiphilic molecule [13].

In the present work, we first investigated the aqueous phase behaviour of SDDS using three different techniques. Then in this study, we have studied the phase states of SDDS + water + octanol lyotropic system to determine phase diagram in such systems. We have investigated the mesomorphic and morphologic properties of in this system. Based on the experimental results, phase diagram of this mixture occurred, which would be helpful for researchers and engineers to work in the field of practical applications.

2. EXPERIMENTAL

2.1 Materials and sample preparation

SDDS (cat. No: 8.22050) and octanol (cat.No.1.00991.1) were obtained from MERCK and used without further purification of bi-distilled water used as a solvent. The required amount of components has been weighed by an And HR-120 scale with an accuracy of 10^{-4} g. The mixtures kept in hermetically-closed vessels have been preserved for homogenisation in a Memmert 400 thermostat at a temperature of 323 ± 0.1 K. Homogeneous lyotropic systems have later been studied using polarized light microscope for textures and sample heating, and Kruss tensiometer for surface tension measurements.

2.2 Methods

The method of polithermic polarized microscopy is based on type of texture, properties of the structure built up of structural units of liquid crystal system and on variation of the structure with temperature and concentration. Accordingly, there are textures which enable us to recognise the phases and have characteristics of the phase concerned. Textures change depending on temperature and concentration. This method allows us to determine the phases and observe the phase transitions.

Textural analysis has significantly contributed to the definition of complex-disordered material and continuous attempts have been made to correlate the interesting physical properties with those textural parameters obtained from the microscopic designs in particular [14]. Birefringence textural morphologies are of importance as

they provide knowledge of the molecular ordering as well as of defect structures and thus their use has been recognized to be a standardized method to characterize distinct phases of liquid crystals [15]. The experimental instruments used are Olympus BX-P polarized microscope, Olympus SC35 microphotographic system, special stage, differential thermocouples, special heater-thermostat, λ -plates and inference filters.

The optical mapping method has been used to find out properties of schlieren textures, aspects of inversion walls and signs and disclinations of the strength of singularities [16].

As for sample heating, we begin to heat the SDDS+water lyotropic samples in a sealed and top-windowed chamber under the polarised microscope. To observe the increasing temperature, a thermocouple attached to a multimeter with two probes, one in the chamber and the other in iced water has been used. While the temperature of the samples is increasing, critical temperature value to signal phase transition is obtained [17]. By means of microphotography through polarised microscope, the textures of the samples have been easily obtained.

The surface tension data for different SDDS concentrations is another part of our phase transition measurement. A Kruss tensiometer, in which Wilhelmy Plate method is used, enabled us to obtain surface tension data for all samples in chosen temperatures (301.0K and 305.0K). This method by which a plate is directly penetrated into the sample and pulled back has allowed us to have the average surface tension value related to the SDDS concentration that we have worked on [18,19]. Surface tension-concentration data which have been shown in two figures can be seen to be consistent with the phase transition.

3. RESULT AND DISCUSSION

3.1 Binary system

3.1.1 Mesomorphism and morphology of SDDS+water lyotropic system

Phase transition is of morphological importance for heterogeneous structures such as lyotropic liquid crystals. The increased temperature enables phase transitions to occur in the system from a phase to another [20,21]. The samples have been studied by a polarized microscope with optical mapping method to identify mesophases as explained before [22]. Thus far, there have been numerous studies on the sodium dodecyl sulphate chosen as an amphiphile component [23-29]. SDDS + water binary system has also been investigated in other studies [25,29]. Sulek et al. [29] found the initial values of the hexagonal mesophase in the ratio of 40.0%wt SDDS + 60.0%wt water. Our study has obtained these values by the ratio of 37.5%wt SDDS + 61.5%wt water.

In such a structure, amphiphilic aggregates associated with accomplish the free energy minima. The major forces involved in these structures are electrostatic and dispersive. The dispersive are generally weak forces but sometimes they may be arranged the ordering interactions between molecules. The electrostatic are attractive forces between ions and dipoles (ion-ion, dipole-dipole, ion-dipole). Increases in temperature may disturb such arrangements. Depend on temperature and

concentration, all lyotropic phases can arise in the same solution which passes through multiple phase transition [30].

When we heated the samples, a rare situation has been seen, which has shown that the hexagonal E mesophase transforms into another anisotropic phase first then into the isotropic phase. It follows from the figures below that schlierens have appeared in the dark region, which is nematic-calamitic (N_c) [5]. The N_c phase transforms into the isotropic form with temperature increasing.

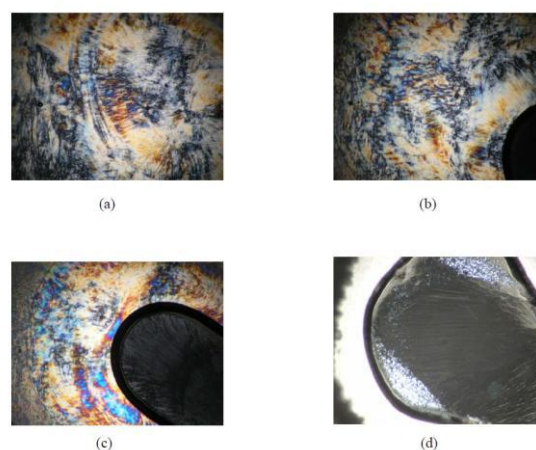


Fig. 1. (a) Hexagonal E, T=303.0 K (1st step) (b) Growth of heated region, T= 310.5 K (2nd step) (c) N_c before isotropic, T=313.0 K (3rd step) (d) Fully isotropic, T=323.0 K (4th step)-magX40

Hexagonal E mesophase occur when long cylindrical rods of amphiphilic molecules are arranged in long axes of the rods in a hexagonal array. These phases are viscous and anisotropic [31,32,4]. Figure 1.a indicates a typical hexagonal E pattern. In figure 1.b, as seen in right bottom corner, heated region starts to grow. The region in figure 1.c denotes a new lyotropic pattern called N_c and the system becomes isotropic in figure 1.d. All the samples between 38.0%wt and 42.0%wt SDDS conform to the similar pattern observed in figures 1a-d. However, they differ in interference pattern textures and phase transition temperature values shown in figure 2.

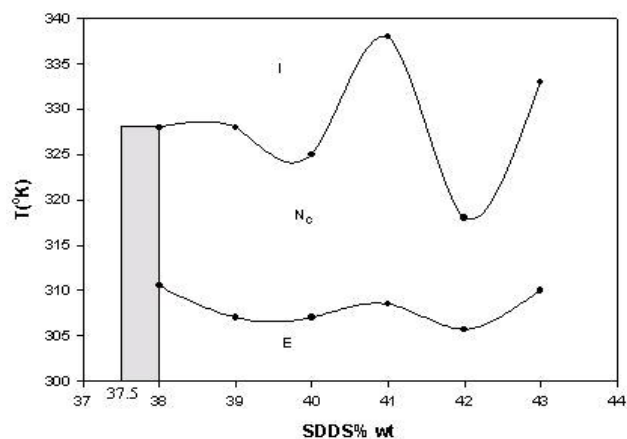


Fig. 2. The phase diagram of SDDS + water binary lyotropic liquid crystalline system determined by method of

polythermic polarising microscopy (gray region shows the transition region from isotropic to lyotropic)

3.1.2 Surface tension measurement

We plotted the surface tension concentration graphs after the measurements were explained in the section of methods as can be seen in Figure 3. Usually the increased temperature and solute concentration result in a reduction in surface tension [33-35]. Amphiphilic molecules contain polar hydrophilic heads and apolar hydrophobic tails which are generally hydrocarbon chains. They are a special class of surface active molecules called surfactants, which are compounds that lower the surface tension of a liquid [4]. However, it can be seen that around and after the critical micelle concentration and in the border of phase transition from isotropic to lyotropic there is a decrease in the surface tension in a small interval. On the other hand, the increase of surface tension proportional to the solute concentration can be observed in some electrolytic substances solved in solvent or in some ionic liquids [20,36-39]. There are also some studies in which the surface tension has been measured and SDDS chosen as the anionic surfactant [1,33,38-40]. In these studies, the critical micelle concentration (CMC) of the system was determined by measuring the surface tension. Thus these studies were performed in low concentration regions. The concentration intervals in which liquid crystal phases occur have not been examined yet.

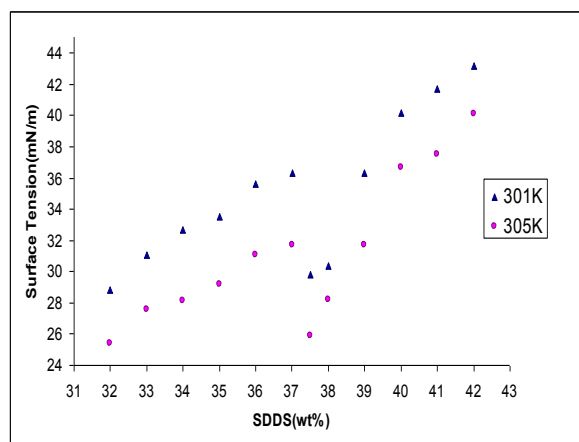


Fig. 3. Surface tension as a function of concentration at certain temperature in SDDS + water binary system.

It is interesting to note that as SDDS is added beyond the point (37.5%wt SDDS) the surface tension begins to rise steadily [1]. The surface tension data distribution shows us the changes in phase states from isotropic to lyotropic LC.

3.2 Ternary system

Addition of a third component, octanol as an alcohol to the SDDS + water lyotropic system has caused the lyotropic mesomorphism of this lyotropic system to widen significantly. The impact of different alcohols on properties of aqueous surfactant solution was extensively studied in recent years [41,42]. Ternary system of the SDDS+octanol+water were previously studied [43] in

which liquid crystal mesophases and the concentration region concerned were not examined although critical micelle formations were discussed unlike our study. Our studies have shown that the integration of linear alcohols into the micelles leads to a remarkable variation in micellar shape and their transport properties and also causes micelle swelling and a decrease of micelle charge density thus increasing the level of ionization. All such structural changes influence reaction levels of micelle-modified processes. Accordingly, figure 4 indicates a partial phase diagram of the SDDS+octanol+water system at 298 K.

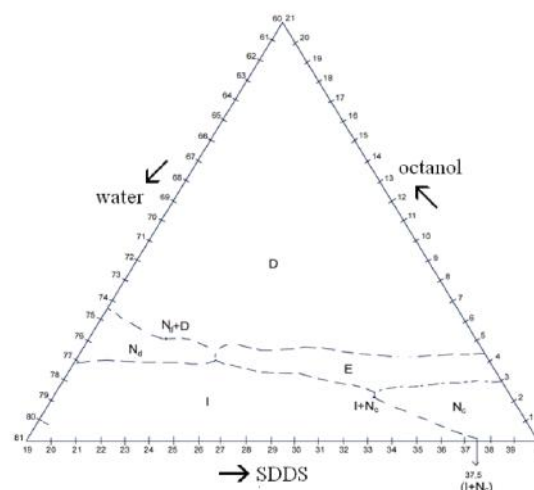


Fig. 4. Phase diagram of the SDDS + octanol+ water system at 298 K. Nematic - calamitic N_c , Nematic- discotic N_d , Hexagonal E, Lamellar D. Interrupted lines are transition Region.

All of the textures in the SDDS + water and SDDS + water + octanol lyotropic systems were stable, reproducible and characterized by evident mesophases. Property of liquid crystal textures in hermetically-closed sandwich-cells did not change without external influences, which indicates that the obtained textures were thermodynamically stable.

Lyotropic nematic liquid crystal phases formed by micellar aggregates with a long range orientational order have been observed in many systems in various compositions and temperature ranges [42].

Direction vector of amphiphile molecules to form nematic-discotic N_d mesophase is parallel to vector-director. Nematic discotic N_d mesophase whose optical anisotropy is positive is uniaxial ($\Delta n > 0$) [44]. In addition, nematic discotic N_d mesophase is of homeotropic orientation, that is to say molecules orient perpendicularly to the reference surfaces of the prepared sandwich-cell [45]. Therefore, when microscope table on which the sample lies rotates, the textures do not blink in dark and bright intervals. Using the above two features, we have been able to distinguish nematic calamitic N_c from nematic discotic N_d mesophases, textures of which have both schlieren formations. From this system, complicated texture of nematic discotic N_d mesophases has appeared (Figure 5.a).

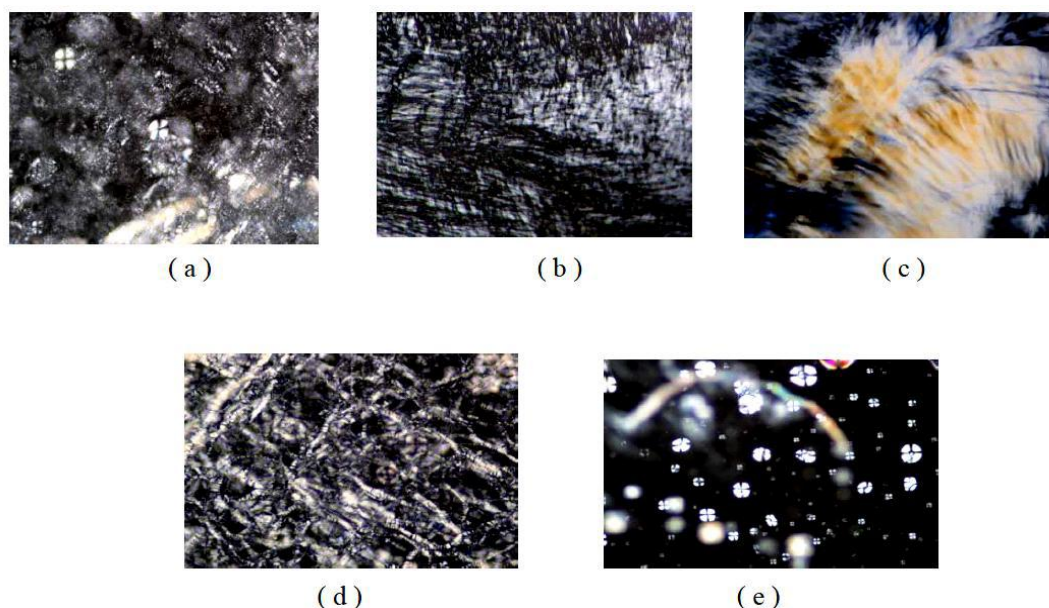


Fig. 5. (a) Specific nematic discotic N_d texture (magx100,21% SDDS+5% octanol+74% water) **(b)** Specific nematic-calamitic N_c texture (mag x100, 37% SDDS+1% octanol+ 62% water) **(c)** Specific hexagonal E texture (mag x100, 28% SDDS+4% octanol+68% water) **(d)** Specific lamellar D texture (mag x100, 25% SDDS+9% octanol+66% water) **(e)** Rounded droplets texture of lamellar D mesophase (magx100, 31% SDDS+7% octanol+ 62% water)

Examination of nematic N_d mesophases obtained from the system can evidently show that schlieren formations of schlieren textures which N_d mesophase exhibited were denser than those of schlieren texture that N_c mesophase presented (Figure 5.b).

The related observations have indicated that disclination strengths of singular points in N_c mesophase are $S = \pm \frac{1}{2}, \pm 1$ while those of singular points in N_d mesophase of schlieren texture are $S = \pm 1$.

Figure 5.c presents typical fibrous textures of hexagonal E mesophase of typical structure [16]. When microscope table was rotated, the texture was found to be blinking in dark and bright intervals, which is caused by its planary orientation. That is, the optic axis is parallel to the long axis of the micelle [44].

In the ternary SDDS+water+octanol system, lamellar D mesophase not observed in binary system emerged at high octanol rates due to interactions between micelles. Lamellar D mesophase has a planary structure, consisting of plate-like micelles with the same thickness and quasi indefinite diameters, which are all separated from one another by aqueous layers [46]. This plate-like structure is accounted for by the equilibrium between repulsive (electrostatic) and attractive (Van der Waals) interactions [47]. Amphiphile molecules to form the layers in the lamellar D mesophase are located in direction of vector-director, which creates a positive birefractance in lamellar D mesophase [48].

TTAB+water+octanol system has exhibited two different types of lamellar D mesophase. Figure 5.d shows a strip-like texture which is composed of irregularly spreading strips blinking in dark and bright series when microscope table has been rotated. On the other hand, figure 5.e is of a textural design consisting of rounded droplets which exhibit crosses when examined under polarized microscope.

4. CONCLUSION

It is important to investigate determination of phases and transitions of binary and ternary lyotropic systems [49]. Optical microscopy is available to determine the phase states of the samples from the interference patterns known as textures. The texture properties and optical mapping method permit us to establish identification of the phases.

Binary system has been found to exhibit isotropic L_1 and Hexagonal E phases whose transition concentration has also been studied. Transition concentration between the established two phases has been examined by two different methods, which has indicated that there is a phase transition for the same value (%37.5 SDDS).

The study for the first time investigated measurements of surface tension in high concentration interval regions. Additionally, the phase transitions have been studied using the surface tension measurements as a function of concentration.

Polar solvents such as alcohol tend to be combined with head groups, which causes the region of the effective head group to decrease and less curved structures to emerge [50]. Therefore, lyotropic polymorphism is expected to be going to increase in number. The experimental consequences are consistent with theoretically expected ones. Addition of octanol to the system has created the nematic-calamitic N_c , nematic-discotic N_d and lamellar D mesophases as well as the hexagonal mesophase.

ACKNOWLEDGEMENTS

The study was partially supported by Research Foundation of Ege University, Grant No. 2009/FEN/024.

- [1]. S. Shrivastava. J. Dey, J. Colloid Interface Sci. 350 (2010) 220.
- [2]. X. Chen, B.D. Hamlington, A.Q. Shen.
- [3]. Langmuir 24 (2008) 541-546.
- [4]. Q. Liu, C. Beier, J. Evans, T. Lee, S. He, Smalyukh. Langmuir 27 (2011) 7446.
- [6]. P. J. Collings. Liquid Crystals-Nature's Delicate Phase of Matter, second ed., Princeton University Press, New Jersey, 1990.
- [7]. S. Chandrasekhar. Liquid Crystals, second ed., Cambridge University Press, Cambridge, 1992.
- [8]. O. Masalci, M. Okcan, N. Kazanci. J. Mol. Struct. 843 (2006) 32.
- [9]. M. Acimis, E. Akpınar. Pyhs. Chem. Chem. Phys. 5 (2003) 4197.
- [10]. M. Simoes, F.S. Alves, K.E. Yamaguti,
- [11]. P.A. Santoro, N.M. Kimura, A.J. Palangana. Liq. Cryst. 33 (2006) 99.
- [12]. J. Mondal, A. Yethiraj. J. Chem. Phys. 136 (2012) 84902.
- [13]. J. Cui, W. He, Y. Yue, H. Zhao, X. Xi. Inorg. Mater. 46 (2010) 1369.
- [14]. C. Albayrak, N. Ozkan, O. Dag. Langmuir 27 (2011) 870.
- [15]. L. Benedini, E.P. Schulz, P.V. Messina,
- [16]. S. D. Palma, D. A. Allemandi, P. C. Schulz. Colloids Surf., A 375 (2011) 178.
- [17]. K. Holmberg, B. Jönsson, B. Kronberg,
- [18]. B. Lindman. Surfactants and Polymers in Aqueous Solution, second ed., John Wiley, Chichester, 1998.
- [19]. Saucier, J. Muller. Physica A 267 (1999) 221.
- [20]. S.V. Muniandy, C.S. Kan, S.C. Lim, S. Radiman,. Physica A 323 (2003) 107.
- [21]. O. Masalci, N.Kazanci. J.Mol.Struct. 919 (2009) 1.
- [22]. J.K. Kim, K.V. Le, S. Dhara, F. Araoka, K. Ishikawa, H. Takezoe. J. Appl. Phys. 107 (2010) 123108-1.
- [23]. K. Lunkenheimer. J. Colloid Interface Sci. 131 (1989) 580.
- [24]. M. Lundin, L. Macakova, A. Dedinaite, P. Claesson, Langmuir 24 (2008) 3814.
- [25]. Y. Iwashita, H. Tanaka. Nat. Mater. 5 (2006) 147.
- [26]. T. Beica, R. Moldovan, M. Tintaru, M. R. Puica, I. Enache, S. Frunza. Liq. Cryst. 31 (2004) 325.
- [27]. N.H. Hartshorne, A. Stuart. Crystals and Polarising Microscope, American Elsevier Pub. Comp, New York, 1970.
- [28]. E. Staples, L. Thompson, I. Turcker, J. Penfold, R. K. Thomas, J. R. Lu, Langmuir 9 (1993) 1651.
- [29]. R. Guo, Z. Li, T. Liu. Colloid. Polym. Sci. 283 (2004) 243.
- [30]. P. Kekicheff, C. Crabielle - Madelmont,
- [31]. M. Ollivon. J. Colloid Interface Sci. 131 (1989) 112.
- [32]. P. Kekicheff. J.Colloid Interface Sci.131(1989) 133
- [33]. L.Q. Amaral, A. Gulik, R. Itri, P. Mariani.
- [34]. Phys. Rev. A 46 (1992) 3548.
- [35]. R. Itri, L.Q. Amaral, P. Mariani. Phys. Rev. E 54 (1996) 5211.
- [36]. M.W. Sulek, T. Wasilewski, K. J. Kurzydowski. Tribol. Lett. 40 (2010) 337.
- [37]. G. Burducea. Rom. Rep. Phys. 56 (2004) 66.
- [38]. F.P. Nicoletta, A. Golemm, G. Ghidichimo. Gazz. Chim. Ital. 126 (1996) 279.
- [39]. D.J. Mitchell, G.J.T. Tiddy, L. Waring,
- [40]. T. Bostock, M. P. McDonald. J. Chem. Soc. Faraday Trans. 79 (1983) 975.
- [41]. P. Warszynski, W. Barzyk, K. Lunkenheimer,
- [42]. H. Fruhner. J. Phys. Chem. B 102 (1998) 10948.
- [43]. K. Szymczyk, B. Janczuk. J. Surfactants Detergents 13 (2010) 207.
- [44]. Y. Imai, K. Shimamoto, T. Takiue, H. Matsubara, M. Aratono, Colloid. Polym. Sci. 288 (2010) 1005.
- [45]. Goodchild, L. Collier, S. L. Mittar, I. Prokeš, J. C. D. Lord, C. P. Butts, J. Bowers, J. R. P. Webster, R. K. Heenan, J. Colloid Interface Sci. 307 (2007) 455.
- [46]. E. Rilo, J. Pico, S. García-Garabal, L. M. Varela, O. Cabeza, Fluid Phase Equilib. 285 (2009) 83.
- [47]. Rico, A. Lattes, J. Phys. Chem. 90 (1986) 5870.
- [48]. S. Pandey, R. P. Bagwe, D. O. Shah. J. Colloid Interface Sci. 267 (2003) 160.
- [49]. Patist, T. Axelberd, D. O. Shah. J. Colloid Interface Sci. 208 (1998) 259.
- [50]. V. Teixeira, R. Itri, L. Q. Amaral. Langmuir 16 (2000) 6102.
- [51]. L.Q. Amaral, M.E.M. Helene, D. R. Bittencourt, R. Itri. J. Phys. Chem. 91 (1987) 5949.
- [52]. S.E. Moya, S.C. Schulz. Colloid Polym. Sci. 277 (1999) 735.
- [53]. R. Bartolino, T. Chiaranza, M. Meuti. Phys. Rev. A 26 (1982) 1116.
- [54]. R. Sampaio, N.M. Kimura, R.C. Viscovini, P. G. R. Fernandes, A.J. Palangana. Mol. Cryst. Liq. Cryst. 422 (2004) 57.
- [55]. G.W. Gray, P.A. Winsor. Adv.Chem. 1 (1976) 213.
- [56]. L. Porcar, J. Marignan, C. Liogure, T. G. Krzywicki, Langmuir 16 (2000) 2581.
- [57]. Nesrullajev, M. Okcan, N. Kazanci. J. Mol. Liq. 108 (2003) 313.
- [58]. R. G. Laughlin, R. L. Munyon, Y. C. Fu,
- [59]. J. Fehl. J. Phys. Chem. 94 (1990) 2546.
- [60]. J. Zhang, Z. Wang, J. Liu, S. Chen, G. Liu.
- [61]. Self-Assembled Nanostructures, Kluwer Academic Publishers, U.S.A, 2002.

Received: 17.01.2013

THE ANALYSIS OF SERIES RESISTANCE AND INTERFACE STATE DENSITY DISTRIBUTIONS OF Au/TiO₂/n-Si METAL-INSULATOR-SEMICONDUCTOR STRUCTURES AT ROOM TEMPERATURE

MURAT SEL , AHMET ASİMOV* , ELCHİN HUSEYNOV**

Physics Department, Faculty of Arts and Sciences, Gazi University, Ankara, Turkey

**Department of Physics, Uludağ University, Görükle, Bursa, Turkey*

***The Institute of Radiation Problems of ANAS, Baku, Azerbaijan*

Corresponding author. Tel.: 00905350628201

E-mail address: fizikasimov@hotmail.com ; elchin55@yahoo.com

The electronic and interface state density distribution properties obtained from current–voltage (I–V) and capacitance–voltage (C–V) characteristics of Au/TiO₂/n-Si Metal–Insulator–Semiconductor Schottky diode were measured at room temperature. The (I–V)–T characteristics are analysed on the basis of thermionic emission (TE). The forward bias I–V of SBDs have been studied at room temperature. SBD parameters such as ideality factor n , the series resistance (R_s) determined Cheung's functions and Schottky barrier height, Φ_{bo} , are investigated as functions of temperature. The diode parameters such as ideality factor, series resistance and barrier heights were found as 3.20 and 2910–2348 Ω and 0,77–0,86 eV, respectively. The diode shows non-ideal I–V behaviour with an ideality factor greater than unity. Furthermore, the energy distribution of interface state density was determined from the forward bias I–V characteristics by taking into account the bias dependence of the effective barrier height. The I–V characteristics confirmed that the distribution of N_{ss} , R_s and interfacial insulator layer are important parameters that influence the electrical characteristics of MIS Schottky diodes.

Keywords: Schottky barrier diode; Ideality factor; Interface states; insulator layer; Series resistance.

PACS: 81.05.Cv; 52.77.Dq

1. INTRODUCTION

Metal-semiconductor (MS) Schottky structures are an essential part of virtually all semiconductor electronic and optoelectronic devices [1–2]. Insulators layers play a significant role in modern device technology. Electrical characteristics of Metal–Insulator–Semiconductor (MIS) structures are influenced by various non-idealities such as formation of an insulator layer and the energy distribution profile of interface states at the metal/semiconductor interface, series resistance and inhomogeneous Schottky barrier heights. The presence of an insulator layer between metal and semiconductor in the MIS structure gives these devices the

properties of a capacitor, which stores the electric charge by virtue of the dielectric property of oxide layers. Due to the existence of oxide layer and two surface charge regions, MIS physics is more complicated than semiconductor surface physics. Recently, insulator layers that form on Si, such as SnO₂ [4] and TiO₂ [5] films have been investigated as a potential material to replace silicon dioxide (SiO₂). The main advantages of these films are low densities of the surface states and high dielectric permittivity when compared to SiO₂. The titanium dioxide (TiO₂) thin films are extensively studied due to their interesting chemical, optical and electrical properties. Various methods have been employed to prepare TiO₂ thin films, among which are e-beam evaporation [6], sol-gel process [7] and chemical vapor deposition [8]

In the study, the I–V characteristics of Au/TiO₂/n-Si Metal–Insulator–Semiconductor Schottky diode were measured at room temperature. Electrical parameters such as ideality factor, barrier height series resistance and Richardson constant were extracted from forward bias I–V measurements. Thus, we examined the electronic properties of main parameters obtained from current–

voltage (I–V) and capacitance–voltage (C–V) measurements and interface state density distribution properties of interface states of Au/TiO₂/n-Si (MIS) SBD. Experimental results show that both N_{ss} and R_s are important parameters that influence the electrical characteristics of MIS structures.

2. EXPERIMENTAL PROCEDURE

The Au/TiO₂/n-Si MIS structure was fabricated on a quarter of 2 in diameter float zone (100) n-type (S doped) single crystal silicon (Si) wafer having thickness of 380 μm . The sample was ultrasonically cleaned in trichlorethylene and ethanol, etched by H₂SO₄/H₂O₂/H₂O=5:1:1 (weight ratio) solution for 30 s., rinsed by propylene glycol and blown with dry nitrogen gas. The high purity gold with a thickness of 1750 Å was thermally evaporated from tungsten filament onto the whole back side on the n-Si wafer at a pressure of 1×10^{-6} Torr in liquid nitrogen trapped oil-free ultra high vacuum pump system. Preceding each cleaning step, the wafer was rinsed thoroughly in de-ionized water of resistivity of 18 M Ω cm. The ohmic contact was formed by sintering the evaporated Au back contact at 350 C⁰ for 5 min in a flowing dry oxygen ambient at rate of 1 lt/min. After oxidation, circular dots of 1mm diameter and 1800 Å thick gold contacts were deposited onto the oxidized surface of the wafer through a metal shadow mask in a liquid nitrogen trapped vacuum system in a vacuum of 1×10^{-6} Torr.

The I–V measurements were performed by the use of a Keithley 220 programmable constant current source, a Keithley 614 electrometer. The C–V measurements were performed at 1 MHz by using HP 4192A LF impedance analyzer. The I–V and C–V characteristics of

the Au/TiO₂/n-Si Schottky diode were studied at 300 K by using temperature controlled Janes vpf-475 cryostat.

3. RESULTS AND DISCUSSION

The forward and reverse current-voltage (I-V) characteristics of Au/TiO₂/n-Si (100) Schottky contacts at room temperature are shown in Fig. 1. We have analyzed the experimental I-V curves according to TE theory in which the current-voltage characteristics are given by the relation [1-2]

$$I = I_0 \exp\left(\frac{qV}{nkT}\right) \left[1 - \exp\left(-\frac{qV}{kT}\right)\right] \quad (1)$$

Where

$$I_0 = AA^*T^2 \exp\left(-\frac{q\phi_{B0}}{kT}\right) \quad (2)$$

is the saturation density, V is the definite forward-bias voltage, A is the effective diode area, k is the Boltzmann constant, T is the absolute temperature, A* is the effective Richardson constant and equals 120 A cm⁻²K⁻² for n-type Si, where ϕ_{B0} (I-V) is the barrier height at zero bias (which is defined by Eq. (2)), and n is called the ideality factor, which is defined as

$$n = \frac{q}{kT} \left(\frac{dV}{d(\ln J)} \right) \quad (3)$$

Fig. 1. shows the experimental semilog-forward and reverse-bias characteristics of the Au/TiO₂/n-Si SBD. The values of the barrier height ϕ_{B0} and the ideality factor n of the Au/TiO₂/n-Si SBD were calculated as 0.77 eV from the extrapolated experimental saturation current, $I_0=7.77 \times 10^{-8}$, and $n=3.20$ from the slope of the linear region of the semilog-forward bias I-V characteristics indicating that the effect of series resistance in this region was not important, respectively [6-7]. The zero-bias barrier height and the ideality factor (n) were determined by Eqs.(1) and (2). The high values of ideality factor can be attributed to effects of the bias voltage drop across the interfacial insulatorlayer.

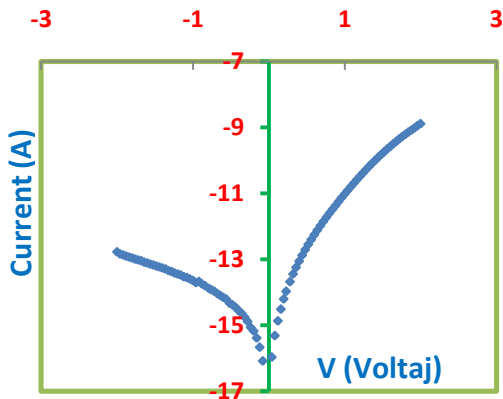


Fig. 1. The experimental forward and reverse current-voltage characteristics of the Au/TiO₂/n-Si Schottky barrier diode at room temperatures.

In this study, the values of the series resistance (R_s) was evaluated from the forward bias I-V data at the high bias voltage region (non-linear region) using the method developed by Cheung [9]. Cheung functions are given as:

$$\frac{dV}{d(\ln I)} = IR_s + n \left(\frac{kT}{q} \right) \quad (4)$$

$$H(I) = V - \left(\frac{kT}{q} \right) \ln \left(\frac{I_0}{AA^*T^2} \right) n \quad (5)$$

$$H(I) = IR_s + n\phi_b \quad (6)$$

where IR_s is the voltage drop across the series resistance of the MIS structure. Fig. 3 shows the experimental $dV/d(\ln I)$ vs. I, and $H(I)$ vs. I plots for the Au/TiO₂/n-Si (MIS) structure, respectively. Thus, a plot of $dV/d(\ln I)$ vs. I will give R_s as the slope and $n(kT/q)$ as the current axis intercept. The values of R_s from their slopes were found as 2910-2348, respectively.

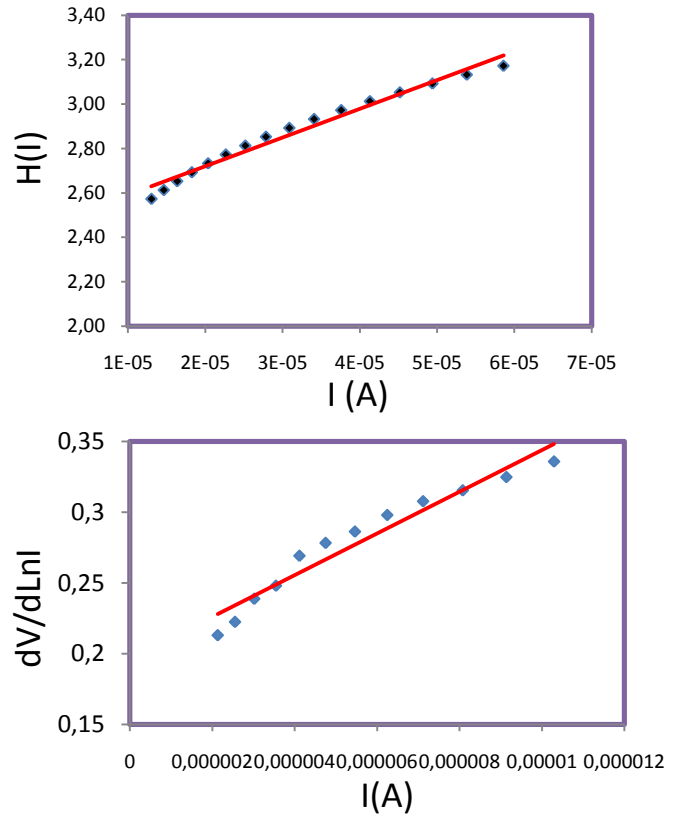


Fig. 2. The experimental $H(I)$ vs. I and $dV/d(\ln I)$ vs. I plots for the Au/TiO₂/n-Si Schottky barrier diode at room temperatures.

Fig. 3(a) shows the C-V characteristic at room temperature ($T=300$ K) measured at frequency of 1000 kHz. In Schottky diodes, the depletion layer capacitance can be expressed as [1,2]

$$\frac{\partial C^{-2}}{\partial V} = \frac{2}{q\epsilon_s A^2 N_D} \quad (7)$$

or

$$C_2 = \frac{1}{n_{CV}} = \frac{2}{q\epsilon_s N_D \left(\frac{\partial C^2}{\partial V} \right)} \quad (8)$$

$$\Phi_{b0}(C-V) = V_d + E_F \quad (9)$$

in Fig. 3(b) to Eq. (8), A is the area of the diode, the dielectric constant of the Si ($=12 \epsilon_0$), q is the electronic charge and N_D is the donor concentration. The diffusion potential or built-in potential is usually measured by extrapolating $1/C^2-V$ plot to the V-axis. The barrier height, Φ_{b0} CV, from C-V measurement is defined by

where E_F is the Fermi energy. According to Eq. (9), the measured barrier height $\Phi_{b0}(C-V)$ is 0,86 eV and the donor concentration is determined to be $1,5 \times 10^{16} \text{ cm}^{-3}$. The difference between barrier heights obtained from I-V and C-V measurements is mainly due to inhomogeneities. Density of states in the conduction band, which is $N_c = 2.8 \times 10^{19} \text{ cm}^{-3}$ for Si at room temperature [11]

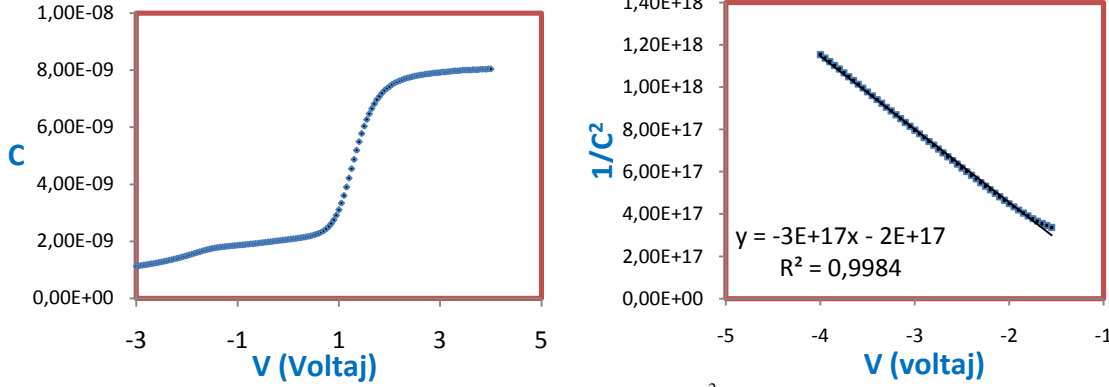


Fig. 3. (a) The experimental capacitance-voltage, and (b) reverse bias C^2-V characteristics of the Au/TiO₂/n-Si Schottky barrier diode in the frequency 1000 kHz at room temperatures.

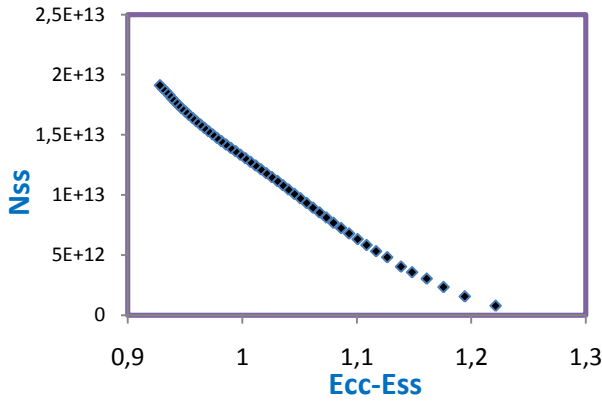


Fig. 4. Density of interface states N_{SS} as a functions of $E_{SS}-E_v$ obtained from the I-V measurements at room temperature.

The interface state energy distribution curve of the Au/TiO₂/n-Si SBD is given in Fig. 4. For an MIS diode having interface states in equilibrium with the semiconductor, the ideality factor, n becomes greater than unity as proposed by Card and Rhoderick [3] and is given by

$$N_{ss}(V) = \frac{1}{q} \left[\frac{\epsilon_i}{\delta} (n(V) - 1) - \frac{\epsilon_s}{W_d} \right] \quad (10)$$

where W_d is the interfacial insulator layer thickness, N_{SS} is the density of interface states, ($\epsilon_i = 48 \epsilon_0$ and $\epsilon_0 = 8.85 \times 10^{-14} \text{ Fcm}^{-1}$) are the permittivities of the semiconductor and interfacial layer, and W_d is the thickness of insulator layer. The interfacial insulator layer thickness ($W_d = 2,23 \times 10^{-5} \text{ sm}$) was obtained from high-frequency (1000 kHz) C-V characteristic using the equation for insulator layer capacitance ($C = C_{ox} = \epsilon A / \delta$), and ϵ_0 is the permittivity of free space. Furthermore, in n-

type semiconductors, the energy of the interface states E_{ss} with respect to the bottom of the conduction band at the surface of semiconductor is given as

$$E_{ss} - E_v = q(\Phi_e - V) \quad (11)$$

where V is the applied voltage drop across the depletion layer and Φ_e is the effective barrier height. The relationship between effective barrier height, applied voltage V and the ideality factor n in given by:

$$\Phi_e = \Phi_{b0} + (1 - 1/n)(V) \quad (12)$$

The interface state density (N_{SS}) values obtained decrease with applied voltages. This confirms that the density of interface states changes with bias and each of applied biases corresponds to a position inside the Si gap. The value of N_{SS} obtained $3,5 \times 10^{12} (\text{eV})^{-1} \text{ cm}^{-2}$.

4. CONCLUSION

The current-voltage characteristics of Au/TiO₂/n-Si MIS Schottky contacts were measured at room temperature. SBD parameters such as ideality factor n, the series resistance (R_s) determined Cheung's functions and Schottky barrier height, Φ_{b0} , are investigated as functions of temperature. The diode parameters such as ideality factor, series resistance were found as 3,20 and 2910-2348Ω respectively. In particular, the values obtained from the C-V measurements are higher than derived from the I-V measurements as expected. The difference between ideality factor obtained from I-V and C-V measurements is mainly due to inhomogeneities. The interface states and interfacial insulator layer at the MIS interface play an important role in the determination of the characteristic parameters of the devices. The energy distribution of the interface state densities of the Au/TiO₂/n-Si diode has been determined taking into account the forward bias I-V measurements. The high

value of ideality factor n has been attributed to the effects of the bias voltage drop across the interfacial insulator layer, the particular distribution of interface states localized at semiconductor-insulator interface, and the special barrier in homogeneities at the MS interface [1,2,3,12,13].

- [1]. Rhoderick EH, Williams RH. "Metal-semiconductor contacts" 2nd ed. Oxford [England] : Clarendon Press ; New York : Oxford University Press, 1988
- [2]. Sze SM. "Physics of semiconductor structures". 2nd ed. New York; 1981.
- [3]. H.C. Card, E.H. Rhoderick, "Barrier Heights of Schottky Junctions on n-InP Treated with Phosphine Plasma" J. Phys. D4 (1971) 1589.
- [4]. A.Tataroglu,Ş.Altındal"Characterization of current-voltage (IV) and capacitance-voltage-frequency (C-V-f) features of Al/SiO₂/p-Si (MIS) Schottky diodes" Microelectron. Eng. 83(2006)582.
- [5]. S.Chakraborty, M.K.Bera, P.K.Bose, C.K.Maiti, "Modeling and Simulation of Memory Devices with High-k Dielectrics" Semicond.Sci.Technol.21 (2006) 335.
- [6]. G. Sanon, R. Rup, A. Mansingh, "Growth and characterization of tin oxide films prepared by chemical vapour deposition" Thin Solid Films 190 (1990) 287.
- [7]. J.P. Chatelon, C. Terrier, E. Bernstein, R. Berjoan, J.A. Roger, "Thin Solid Films" 247 (1994) 162.
- [8]. H.Y. Ha, S.W. Nam, T.H. Lim, I.H. Oh, S.A. Hong, J. Membr. "The double Gaussian distribution of barrier heights in Al/TiO₂/p-Si (metal-insulator-semiconductor) structures at low temperatures" Sci. 111 (1996) 81.
- [9]. S.K. Cheung, N.W. Cheung, "Extraction of Schottky diode parameters from forward current-voltage characteristics" Appl. Phys. Lett. 49 (1986) 85.
- [10]. A. Türüt, M. Sağlam, H. Efeoğlu, N. Yalçın, M. Yıldırım, B. Abay, "Electrical analysis of organic interlayer based metal/interlayer/semiconductor diode structures" Physica B 205 (1995) 41.
- [11]. D.A. Neamen, in: "Semiconductors Physics and Devices", R. R. Donnelley & Sons Company, Sydney, 1992
- [12]. Karataş Ş, Altındal Ş, Çakar "Current transport in Zn/p-Si(100) Schottky barrier diodes at high temperature" M. Physica B 2005;357:386.
- [13]. Werner JH,Guttler HH. "Barrier inhomogeneities at Schottky contacts" J. Appl. Phys.1991; 69:1522.

Otaq temperaturunda Au/TiO₂/n-Si metal – dielektrik – yarımkəçirici quruluşların səth sıxlığının paylanmaları və ardıcıl müqavimətlərin analizi

Murad Sel , Əhməd Asimov, Elçin Hüseynov

Otaq temperaturunda Au/TiO₂/n-Si metal dielektrik yarımkəçirici Şotki diyodların volt – amper (I-V) və tutum-gərginlik (C-V) ölçümlərindən elektronik və səthi elektron sıxlığı kimi özəllikləri tapıldı. Termoionik emmissiya nəzəriyyəsi əsasında (I-V-T) xassələri araşdırıldı. Otaq temperaturunda düz istiqamətdə gərginlik təbii etməklə volt – amper ölçümləri əldə edildi. Çəng funksiyalarının köməyi ilə Şotki bariyer diyotların ideallıq faktoru, ardıcıl müqavimət və bariyer qalınlığı kimi özəllikləri temperaturun bir funksiyası olaraq araşdırıldı. İdeallıq faktoru, ardıcıl müqavimət və bariyer qalınlığı kimi diyod özəllikləri 3.20; 2910-2348 Ω ve 0,77-0,86 eV, olaraq tapıldı. Volt – amper (I-V) ölçmələrində Şotki diyodun idellıq faktoru böyük qiymət almışdır. Buna görə də, effektiv bariyer qalınlığı hesaba qatılaraq volt – amper xarakteristikalarından enerji dağılması və səthi elektron sıxlığı tapıldı. I-V xarakteristikasından gördük ki, MIS diyotların elektrik xarakteristikaları olan Nss, Rs, Wd, önəmli parametrlərdir.

Açar sözlər: Şotki bariyer diodu; ideallıq amili; interfeys hallar; izolyator qatı; seriya müqaviməti.

Анализ рядов сопротивления и состояние интерфейса распределений плотности Au/TiO₂/n-Si металл-дielektrik-полупроводник при комнатной температуре

Мурат Сэл, Ахмед Асимов, Эльчин Гусейнов

Электронные и состояние интерфейса плотность распределения свойств, полученных от текущего напряжения (I-V) и емкость-напряжение (C-V) характеристик Au/TiO₂/n-Si металл-дielektrik-полупроводник диода Шоттки были измерены при комнатной температуре.(I-V)-T характеристики анализируются на основе термоэлектронной эмиссии (TE).Прямого смещения I-V из SBDS были изучены при комнатной температуре. SBD такие параметры, как фактор идеальности n , последовательное сопротивление (RS) определяются функции Cheung и высота барьера Шоттки, F_{bo}, исследованы как функции температуры.Диод параметры, такие как фактор идеальности, последовательное сопротивление и высоты барьеров были найдены в 3.20 и 2910-2348 Ω и 0,77-0,86 эВ, соответственно.Диод показывает неидеальных I-V поведения с коэффициентом идеальности больше единицы. Кроме того, распределение энергии Интерфейс плотности состояний определялась из прямого смещения ВАХ с учетом смещения зависимость эффективной высоты барьера.ВАХ подтвердил, что распределение Nss, Rs и межфазного слоя изолятора являются важными параметрами, которые влияют на электрические характеристики МДП-диодов Шоттки.

Ключевые слова: барьер Шоттки диод; Идеальность фактор; интерфейс государств; слой диэлектрика; серия сопротивление.

CONTENTS

1.	Atomic-force Microscopy of Van-Der Waals surface of layered crystals by GaSe and GaSe<impurity> types A.M. Pashayev, B.G. Tagiyev, R.A. Ibragimov, A.A. Safarzade	3
2.	Analysis of main artifacts in scanning probe microscopy (II) S.D. Alekperov	9
3.	Solution of generalization of principal chiral field problem for the high rank semisimple algebras M.A. Mukhtarov	12
4.	Influence of temperature and doping with rare-earth elements on electrophysical parameters of A ^{III} B ^{VI} crystals with layered structure A.Sh. Abdinov, R.F. Babayeva, N.A. Ragimova, R.M. Rzayev, S.I. Amirova	17
5.	Characterization of electrical, optical and morphological properties of CuInSe ₂ thin films exposed to plasma treatment K. Koseoglu, S. Acar, B.G. Salamov, T.G. Mammadov and F. Dagdelen	23
6.	Dielectric relaxation and conduction of TlInTe ₂ crystal subjected to radiation exposure R.M. Sardarli, O.A. Samedov, P.Sh. Agayeva, A.P. Abdullayev, F.T. Salmanov, S.Ph. Samedov	28
7.	Theoretical conformational analysis of piperazine-2,3,5,6-tetraone Metin Bilge, Yenel Gökpek, Mahir Tursun, Nesrin Emir and Cemal Parlak	32
8.	Phase transitions and their co-existence in the TlGaSe ₂ - TiCoS ₂ system N.Z. Gasanov, Mir-Hasan Yu. Seyidov, R.Z. Sadykhov, F.M. Seyidov, R.G. Veliyev, Yu.G. Asadov, E.M. Kerimova, A.A. Isayeva, K.M. Huseynova	37
9.	Influence of small particles on electrohydrodynamic instability in the nematic liquid crystal T.D. Ibragimov, Ch.O. Qajar, Sh.Yu. Samedov, G.M. Bayramov	42
10.	Creating of ordered porous anodic alumina templates on glass substrates Sh.O. Eminov, Kh.D. Jalilova, A.A. Rajabli, G.Kh. Mamedova, J.A. Guliyev, Z.I. Badalova	46
11.	Decrease in risk erroneous classification the multivariate statistical data describing the technical condition of the equipment of power supply systems E.M. Farhadzadeh, Y.Z. Farzaliyev, A.Z. Muradaliyev	50
12.	The nonequilibrium radiative states in external constant and alternating magnetic fields E.R. Hasanov, B.Z. Aliyev	58
13.	Piezoelectric properties of polymer composite dielectrics M.A. Kurbanov, A.A. Bayramov, T.G. Mammadov, M.M. Kuliev	63
14.	Electrophysical properties of photodiode on the base of iridium-silicon silicide E.A. Kerimov	67
15.	Characterization of lyotropic liquid crystalline phases formed in sodium dodecyl sulphate/octanol/water ternary lyotropic system Emir Haliki, Ozgur Masalci and Nadide Kazanci	70
16.	The analysis of series resistance and interface state density distributions of Au/TiO ₂ /n-Si metal-insulator-semiconductor structures at room temperature Murat Sel, Ahmet Asimov, Elchin Huseynov	75



www.physics.gov.az